Three-Dimensional Fracture Mechanics Computations Using Tetrahedral Finite Elements

by

Harish Rajaram

Bachelor of Technology in Mechanical Engineering,
Indian Institute of Technology, Madras, India (1997)

Submitted to the Department of Mechanical Engineering
in partial fulfillment of the requirements for the degree of

Master of Science in Mechanical Engineering

at the

MASSACHUSETTS INSTITUTE OF TECHNOLOGY

June 1999

Author .....
Department of Mechanical Engineering
May 7, 1999

Certified by .....
David M. Parks
Professor of Mechanical Engineering
Thesis Supervisor

Accepted by .....
Ain A. Sonin
Chairman, Department Committee on Graduate Students

Three-Dimensional Fracture Mechanics Computations Using Tetrahedral Finite Elements

by

Harish Rajaram

Submitted to the Department of Mechanical Engineering
on May 7, 1999, in partial fulfillment of the
requirements for the degree of
Master of Science in Mechanical Engineering

Abstract

With the development of CAD packages which can create complicated 3-D models and mesh them with tetrahedral elements with relative ease, the application of finite element techniques in mechanical design has reached unprecedented proportions. However, the extension of these techniques to fracture mechanics studies is hindered by the unavailability of a general method to obtain fracture mechanics singularity strength (J, K_I, etc.) for tetrahedral meshes. An approach to obtain these parameters along a 3-D crack front using tetrahedral elements is presented here. The method is then validated on well-known crack geometries using tetrahedral meshes generated from commercially-available CAD-FEA packages for both elastic and elastic-plastic problems.

Thesis Supervisor: David M. Parks
Title: Professor of Mechanical Engineering

Acknowledgments

I wish to express my sincere gratitude to Prof. Parks for his constant support, encouragement and insightful guidance during my stay here at MIT. I have gained a lot from interacting with him and thoroughly enjoyed working with him. I also wish to thank Prof. McClintock for his advice on various aspects of fracture mechanics and above all for his patience and suggestions. A large share of my thanks goes to Dr. Simona Socrate, my co-advisor in this work. I admire her perseverance and penchant for perfection and working with her has been a memorable experience. Special thanks to Ray Hardin for taking care of many administrative details. Thanks to Tom, Kevin, Gu, Jorgen, Clarence, Steve, Yioula, Ethan, Brian, Prakash and other Mechanics and Materials lab mates Rami, Heather, Jeremy, Greg, Jennifer, Hyung-Soo and Yu for making my stay at MIT a wonderful experience.

My friends Mahadevan, Venkatesan, Sreeram and other IITians have helped me a lot in feeling at home in the other side of the globe. I am indebted to my parents for their constant support and motivation all through my life.

This work was supported by the D.O.E under grant number DE-FG02-85ER13331 to MIT.

Contents

List of Figures

List of Tables

Chapter 1

Introduction

1.1 Fracture mechanics singularity strengths

1.1.1 Linear elastic fracture mechanics

The stress fields at the tip of a crack are given by the Williams [2] expansion

$$\sigma_{ij} = (\frac{k}{\sqrt{r}})f_{ij}(\theta) + \text{ higher-order terms,} \tag{1.1}$$

where σ_{ij} is the stress tensor, r and θ are as defined in figure 1-1, k is a constant, and f_{ij} are dimensionless functions of θ. The higher-order terms depend on the geometry, but the solution for any given configuration contains a leading term that is proportional to $1/\sqrt{r}$. As $r \to 0$, the leading term approaches infinity, but the other terms remain finite or approach zero. The above equation describes a stress singularity, since stress is asymptotic to $r = 0$.

There are three types of loading a crack can experience: Mode I, where the principal load is applied normal to the crack plane; Mode II, which is in-plane shear; and Mode III, which is out-of-plane shear. For Mode I loading, the stress state ahead of the crack tip reduces to

$$\lim_{r\to 0} \sigma_{ij}^{(I)} = (\frac{K_I}{\sqrt{2\pi r}})f_{ij}^{(I)}(\theta). \tag{1.2}$$

The factor K_I is called the stress intensity factor for Mode I type loading. The stress

intensity factor defines the amplitude of the crack tip singularity and completely defines the crack tip conditions, in the sense that if K_I is known, then all components of stress and strains in front of the crack can be computed. Closed-form solutions for K_I for a variety of simple crack geometries and loading conditions have been tabulated in the literature [3]. For complex geometries, the stress intensity factors are computed using experimental and/or numerical methods. Historically, finite elements have been used to compute K_I using energy-based methods. The stiffness derivative formulation by Parks [9] first used finite elements for the virtual crack extension method to accurately compute compute K_I, and the domain integral method (see chapter 2), which is based on the virtual crack extension method, has been widely used to compute K_I-values for various crack configurations. Computational fracture mechanics has developed since, and a discussion on computational issues can be found in [4].

Elastic analysis of the stresses at the crack tip is valid as long as the plasticity at the crack-tip is negligible. A first-order estimate of the crack-tip plastic zone is given by

$$r_y = \frac{1}{2\pi}(\frac{K_I}{\sigma_{YS}})^2, \tag{1.3}$$

where σ_{YS} is the yield strength of the material. More accurate estimates of the size of the plastic zone using various correction factors can be found in [5]. Thus for K_I to be a valid singularity, or for linear elastic fracture mechanics (LEFM) to be valid, we must have small-scale yielding (SSY), which requires the plastic zone to be much smaller than the in-plane dimensions of the structure.

Most of the classical solutions in fracture mechanics have been performed by reducing the problem to two dimensions (*i.e.*, either plane stress or plane strain). In general, the crack-tip conditions are neither plane stress nor plane strain, but are three-dimensional. There are certain cases when either of these assumptions provide good approximations. For a specimen with a thickness (out-of-plane dimension) much greater than the plastic zone, plane strain conditions prevail in the interior near the crack tip. Similarly, plane stress conditions prevail for a thin specimen. It has been

observed [5] that the size of the plastic zone for a specimen in plane strain is smaller than the one for a plane stress specimen, loaded to the same K_I-level.

The utility of K lies in its ability to predict fracture. Theoretically fracture occurs (*i.e.*, a pre-existing crack in a material would begin to grow) when K equals a critical value, K_c, which is termed the fracture toughness of the material. It must be noted that while K is a loading parameter, K_c is purely a material parameter (under the conditions described below). In some sense, K_c is the resistance of the material to crack propagation. If the plastic zone is too large, or if the specimen thickness is too small, the constraint at the crack tip relaxes, and this lower degree of triaxiality results in higher toughness. One manifestation of this process is the fact that the plane strain fracture toughness is generally smaller than the fracture toughness in plane stress. The plane strain fracture toughness is denoted as K_{Ic}, and the design-against-fracture criterion can now be expressed as $K \leq K_{Ic}$. The American Society for Testing and Materials (ASTM) has laid down specifications for K_{Ic} testing, requiring

$$\text{in-plane, out-of-plane dimensions} \geq 2.5(\frac{K_I}{\sigma_{YS}})^2$$

for a valid K_{Ic} result.

1.2 Elastic-plastic fracture mechanics

Linear elastic fracture mechanics (LEFM) is valid only as long as non-linear material deformation is confined to a small region surrounding the crack-tip. For materials and structures exhibiting substantial plastic deformation, elastic-plastic fracture mechanics must be used. Analogous to the Williams expansion (1.1) for the elastic fields near the crack-tip, the Hutchinson-Rice-Rosengren (HRR) singularity fields describe the asymptotic elastic-plastic crack-tip fields for power-law hardening nonlinear stress-strain behavior. Two elastic-plastic crack-tip parameters which characterize the crack-tip fields are the J-integral and the crack-tip opening displacement (CTOD). The J-integral can be computed numerically using a finite element implementation of the domain integral method (detailed in chapter 2). A detailed discussion on the J-integral and elastic-plastic fracture mechanics is presented in chapter 6.

1.3 Status of fracture mechanics computation using FEM and the need for a general procedure for tetrahedral elements

The overall quality of mesh generators for tetrahedral elements has been consistently improving over the past decade, and a number of CAD-FEA interfaces are now available, thus allowing construction of complicated 3-D models at the click of a button. However, currently-available finite element implementations of domain integral or virtual crack extension methods for evaluating the variation of fracture mechanics singularity strength (J, K_I, etc.) along a 3-D crack front require the use of brick elements in the neighborhood of the crack. Unfortunately, the capabilities of mesh generators for brick elements remain in a comparatively early stage of development [1]. In order to address this issue, we extended domain integral techniques to tetrahedral meshes.

A "straightforward" implementation of the method (see chapter 3) proved quite unsatisfactory; the estimated nodal J-values along the crack front depended strongly on the particular choice of the perturbation field and were in poor agreement with analytical predictions. Refining the tetrahedral meshes and optimizing element aspect ratios did not result in substantial improvements. These difficulties are tied to the inability of the quadratic tetrahedral shape functions to describe accurately the gradients introduced by a node-based representation of the perturbation fields.

An alternative domain integral procedure to calculate 3-D stress intensity factors has been proposed by Červenka and Saouma [6]. In their approach, all the finite element support is abandoned, and the domain integral is evaluated through quadrature over an analytically-defined tubular domain surrounding the crack front. Integrands at the quadrature points of the domain integral, which do not necessarily correspond to either nodes or integration points of the finite element mesh, must be interpolated from the finite element data. The method, while general in its applicability to all finite element formulations, does not address the problems specific to tetrahedral meshes.

The solution also presents inherent limitations: the crack front must intersect the free surfaces at right angles, and the entire boundary of the domain of integration must lie within the body, thus limiting the radius of the domain to the minimum distance between the crack front and the nearest free surface. These requirements restrict the applicability of the technique to a limited set of crack configurations.

In the approach proposed here (chapter 4), we outline a procedure to obtain the singularity strengths (J, K) to overcome the poor performance of the tetrahedral shape functions while remaining within the framework of the finite element method. We use a piece-wise linear crack-front perturbation pattern and selectively evaluate the perturbation gradient at the integration points of the elements in the interior of the domain through direct analytical differentiation of the globally-defined perturbation field. We retain the shape function representation of the perturbation gradient for elements on the boundary of the domain. The versatility of finite elements in modeling crack combinations and free surface configurations is thus preserved. This expedient has allowed us to improve dramatically the accuracy of the procedure, as demonstrated by validation on a number of standard crack configurations. We also evaluate alternative crack-front perturbation patterns and domain integral evaluations, and the accuracy of each method is tabulated in chapter 5. The proposed method is validated for the linear elastic case first (see chapter 6) and the stress intensity factors are calculated for a number of crack geometries. The formulation for the elastic-plastic case (see chapter 7) is then developed, and the method is validated for various crack geometries. The elastic-plastic analysis is also conducted on different material models and hardening behavior and compared with reported results. The effect of mesh topology on the accuracy of the computed J-values is studied, and guidelines to obtain accurate J-values are proposed in chapter 8.

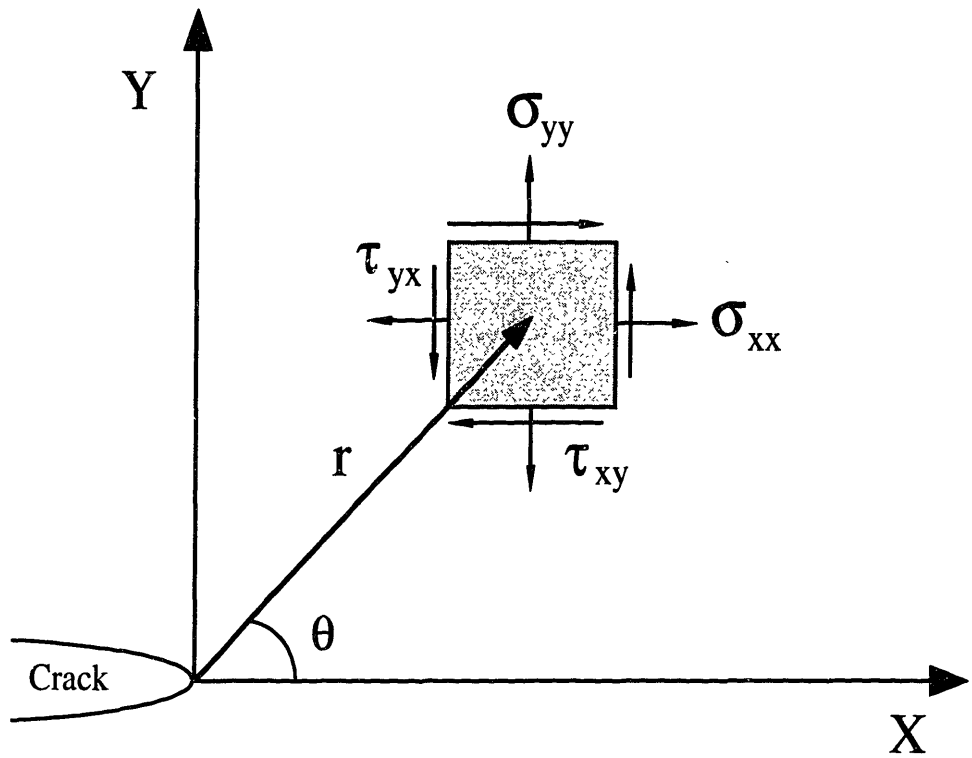

Figure 1-1: Stress field at the tip of a crack

Chapter 2

Domain integral method

2.1 Definition of crack tip parameters

The path-independent J-integral is a measure of the intensity of the singular crack-tip fields which can be used to correlate the initiation of crack propagation. For a two-dimensional, planar solid, assuming small displacement gradients and neglecting body forces and crack-face tractions, the path-independent J-integral is defined by [7]

$$J = \int_{\Gamma} [W\alpha_1 - \sigma_{ij}\alpha_j \frac{\partial u_i}{\partial x_1}] d\gamma, \tag{2.1}$$

where Γ is any counter-clockwise path within the body starting on the lower crack-face and terminating on the upper crack-face, as shown in figure 2-1 (a). Here α_i is the outward normal to Γ, σ_{ij} the Cauchy stress, u_i the displacement, $d\gamma$ the increment of arc length along Γ, and W the strain energy density defined by

$$W(\epsilon_{kl}) = \int_0^{\epsilon_{kl}} \sigma_{ij} d\epsilon_{ij}. \tag{2.2}$$

In plane strain, the potential energy per unit thickness, $\tilde{\pi}$, of a loaded body is

$$\tilde{\pi} = \int_A W(\epsilon_{ij}) dA - \int_{\partial A_T} \bar{T}_i u_i d\gamma, \tag{2.3}$$

where A is the area of the body and ∂A_T is the portion of the boundary where the tractions, $\bar{T}_i$, are prescribed. The energy release rate, $\mathcal{G}$, is a characterizing parameter of elastic crack tip fields. $\mathcal{G}$ denotes the decrease in $\tilde{\pi}$ due to a unit crack advance in its plane with the tractions held fixed :

$$\mathcal{G} = -\frac{\partial \tilde{\pi}}{\partial l} \mid_{\bar{T}} . \tag{2.4}$$

Then, to the first order,

$$\mathcal{G}\delta l = -\delta\tilde{\pi}, \tag{2.5}$$

where δl denotes the virtual crack advance, uniform through-the-thickness in a 2-D formulation.

Expression (2.5) can be generalized to three-dimensional problems by introducing a point-wise definition of the energy release rate, $\mathcal{G}(s)$, as a function of the arc-length measuring curvilinear coordinate, s, along the crack-front, C. Let $\delta l(s)$ denote the magnitude of the virtual crack advance at s, in the plane of the crack and in the direction normal to the crack-front, as shown in figure 2-1 (b). Equation (2.5) can be recast, to within first-order terms in $\delta l(s)$, as

$$\int_C \mathcal{G}(s)\delta l(s) ds = -\delta\pi, \tag{2.6}$$

where ds is the elemental arc length along C, and $-\delta\pi$ is the decrease in total potential energy of the body.

The energy release rate, $\mathcal{G}$, can be evaluated by means of the contour integral J. J and $\mathcal{G}$ are equivalent for a crack advancing uniformly through the thickness under plane stress or plane strain conditions [8]. Along a 3-D crack-front, as $r \rightarrow 0^+$, asymptotic plane strain conditions prevail so that the three-dimensional stress fields approach the plane strain two-dimensional fields along C. Hence, as Γ shrinks onto the crack front, $\Gamma \rightarrow \Gamma_0$ [1], the local value of the energy release rate, $\mathcal{G}(s)$, and point-

[1] As $\Gamma \rightarrow \Gamma_0$, $r(\mathbf{x}) \rightarrow 0^+$ for any $\mathbf{x} \in \Gamma$

wise value of the J-integral, $J(s)$, become equivalent:

$$\mathcal{G}(s) = \lim_{\Gamma \to \Gamma_0} \int_{\Gamma(s)} \left[W\alpha_k n_k - \sigma_{ij}\alpha_j \frac{\partial u_i}{\partial x_k} n_k \right] d\gamma = J_{\Gamma_0}(s) = J(s), \tag{2.7}$$

where $\mathbf{n}$ is the in-plane normal to the crack-front at location s. Equation (2.6) can then be written as

$$\int_C J(s)\delta l(s) ds = -\delta\pi, \tag{2.8}$$

with the understanding that $J(s)$ is defined through (2.7).

2.2 Volume integral expressions for evaluating the energy release rate

The domain integral method provides a convenient way to calculate the energy release rate for 2-D and 3-D problems [8]. The finite element formulation of the domain integral method corresponds to the virtual crack extension method [9], which is versatile in its applicability to 3-D crack configurations.

2.2.1 Two-dimensional formulation

Introducing Eshelby's energy momentum tensor [10], $P_{ij} = W\delta_{ij} - \sigma_{mj}\partial u_m/\partial x_i$, we can recast (2.1) in the more compact form

$$J = \int_\Gamma [W\delta_{1j} - \sigma_{ij}\frac{\partial u_i}{\partial x_1}]\alpha_j d\gamma = \int_\Gamma P_{1j}\alpha_j d\gamma. \tag{2.9}$$

We now consider a second curve around the crack tip, Γ_1, surrounding Γ, and define a simply-connected region Ω between Γ_1 and Γ, as shown in figure 2-2. Ω is bounded by the closed curve $\Psi = \Gamma_1 + \Gamma^+ - \Gamma + \Gamma^-$. The path-independence of J [7] gives

$$J = \int_\Gamma P_{1j}\alpha_j d\gamma = \int_{\Gamma_1} P_{1j}\alpha_j d\gamma. \tag{2.10}$$

We define a vector $\boldsymbol{\beta}$ as the outward normal to Ψ, such that $\boldsymbol{\beta} = -\boldsymbol{\alpha}$ on Γ, and $\boldsymbol{\beta}$

$= \boldsymbol{\alpha}$ on Γ_1. If the crack faces are traction-free, then $\sigma_{ij} \cdot \beta_j = 0_i$ on Γ^+ and Γ^-. Also, on Γ^+ and Γ^- the vector $\boldsymbol{\beta}$ is normal to the direction of crack propagation, $\beta_1 = 0$, so that (2.5) can be written as

$$-\delta\tilde{\pi} = \mathcal{G}\delta l = J\delta l = \int_\Psi [W\delta_{1j} - \sigma_{ij}\frac{\partial u_i}{\partial x_1}]q_1\beta_j d\gamma = \int_\Psi P_{1j}q_1\beta_j d\gamma, \tag{2.11}$$

where we have introduced a sufficiently-smooth (C^0) vector-valued perturbation field $\mathbf{q} = q_1\ \mathbf{e}_1$ in Ω which has magnitude δl on Γ, and vanishes on Γ_1:

$$q_1 \equiv \begin{cases} \delta l & \text{on and within } \Gamma\ , \\ 0 & \text{on } \Gamma_1. \end{cases}$$

Application of the divergence theorem reduces (2.11) to

$$-\delta\tilde{\pi} = J\delta l = \int_\Omega [\frac{\partial}{\partial x_j}(P_{1j}q_1)]dA = \int_\Omega [\frac{\partial P_{1j}}{\partial x_j}q_1 + P_{1j}\frac{\partial q_1}{\partial x_j}]dA. \tag{2.12}$$

Since $\partial P_{1j}/\partial x_j = 0$ in Ω [10], (2.12) becomes

$$-\delta\tilde{\pi} = J\delta l = \int_\Omega [W\delta_{1j} - \sigma_{ij}\frac{\partial u_i}{\partial x_1}]\frac{\partial q_1}{\partial x_j}dA. \tag{2.13}$$

2.2.2 Three-dimensional formulation

For three-dimensional crack configurations, (2.7) and (2.8) can be combined to express the decrease in total potential energy as

$$-\delta\pi = \int_C \delta l(s)[\lim_{\Gamma\to\Gamma_0}\int_\Gamma P_{kj}n_k\alpha_j d\gamma]ds. \tag{2.14}$$

Introducing surface S_0 as the envelope of the curves $\Gamma_0(s)$ as shown in figure 2-3 (a), we can write (2.14) as

$$-\delta\pi = \lim_{S\to S_0}\int_S P_{kj}n_k\alpha_j\delta l(s)dS. \tag{2.15}$$

Now consider a second surface around the crack tip, S_1, surrounding S_0, and define a three-dimensional simply-connected domain Ω between S_0 and S_1, as shown in figure 2-3 (b). Ω is bounded by the closed surface $\mathcal{S}$ formed by the surfaces S_0, S_1, S^+, S^-, S_R and S_L, where S^+ and S^- are surfaces on the respective crack faces, and S_R and S_L are the respective ends of the cylindrical domain as shown in figure 2-3 (b). We define a vector $\boldsymbol{\beta}$ as the outward normal to $\mathcal{S}$, such that $\boldsymbol{\beta} = -\boldsymbol{\alpha}$ on S_0; also, the traction-free crack surfaces S^- and S^+ have their respective outward normals $\boldsymbol{\beta} = \pm\mathbf{m}$, where $\mathbf{m}$ is the normal to the crack plane.

We now consider a sufficiently-smooth (C^0) virtual crack advance pattern, $\delta l(s)$ which vanishes at all crack locations outside the Ω-domain[2], and the corresponding perturbation field, $\mathbf{q}$, in Ω as

$$\mathbf{q} \equiv \begin{cases} \delta l(s)\,\mathbf{n}(s) & \text{on the crack front,} \\ \mathbf{0} & \text{on } S_1, \\ \mathbf{0} & \text{on } S_R \cup S_L, \\ \mathbf{q}\cdot\mathbf{m} = 0 & \text{on } S^+ \cup S^-. \end{cases}$$

The third condition applies only if S_L and S_R are not bounding surfaces of the body. If an end surface is a bounding surface of the body, only the components of $\mathbf{q}$ normal to that bounding surface must vanish. If the crack faces are traction-free, $\sigma_{ij}\beta_j = 0_i$ on S^+ and S^-, so that $q_k P_{kj}\beta_j = 0$ on S^+ and S^-. Combining these results with (2.15), we obtain

$$-\delta\pi = \int_S [P_{kj}q_k\beta_j]\ dS. \tag{2.16}$$

Application of the divergence theorem to (2.16) leads to

$$-\delta\pi = \int_\Omega [W\delta_{kj} - \sigma_{mj}\frac{\partial u_m}{\partial x_k}]\frac{\partial q_k}{\partial x_j}dV, \tag{2.17}$$

where use has again been made of the result $\partial P_{kj}/\partial x_j = 0_k$ [10].

[2]If the end surfaces, S_L and S_R are not bounding surfaces of the body, this condition requires $\delta l(s)$ to vanish at the domain end-points where C intersects S_L and S_R. If an end surface is such a bounding surface, all components of crack advance normal to the bounding surface must vanish at the corresponding end point along C.

2.3 Finite element implementation

Finite element (FE) implementation of the domain integral method for Lagrangian elements is extensively discussed in [8]. Here we specialize the formulation to 10-noded 3-D isoparametric tetrahedral elements. At each point K along the crack, we define a toroidal coordinate system as shown in figure 2-4 (a), consisting of a crack-front tangent vector $\mathbf{t}$ and normal vector $\mathbf{n}$ in the crack-plane. We also define a constant normal vector $\mathbf{m} = \mathbf{n} \times \mathbf{t}$ perpendicular to the crack-plane. The vectors $\mathbf{n}$ and $\mathbf{t}$ vary with the coordinate s. The position of each point P in Ω is identified by its distance from the crack-front, r, the curvilinear coordinate s^* of its projection, P^*, on the crack-front, and the angle θ. In general we can write the position of P^*, $\mathbf{X}\ (P^*) = \mathbf{X}\ (P)$ - $\mathbf{r}$, as shown in figure 2-4 (b). In a FE model of the cracked body, the crack-front is discretized by M element-edges of tetrahedral elements and their corresponding N nodes.

Recalling the expressions (2.8) and (2.17) for the energy release rate, the method to obtain values of the J-integral at each of the N nodes along the crack-front $\{J_1, J_2, .., J_K, .., J_N\}$ involves definition of N perturbation patterns, $\{\delta l^1(s),\ \delta l^2(s),..,\ \delta l^K(s),..,\ \delta l^N(s)\}$, centered on each of the N nodes. For the $K-th$ perturbation pattern $\{\ \mathbf{q}^K;\ \delta l^K(s);\ \Omega^K\ \}$, we have a crack-front integral expression for the energy release:

$$\delta\pi^K = -\int_C J(s)\delta l^K(s)ds, \tag{2.18}$$

as well as the corresponding domain-integral expression:

$$\delta\pi^K = -\int_{\Omega^K}[W\delta_{kj} - \sigma_{mj}\frac{\partial u_m}{\partial x_k}]\frac{\partial q_k^K}{\partial x_j}dV. \tag{2.19}$$

Equating the right-hand sides of (2.18) and (2.19), we obtain an implicit expression for the J-profile. Nodal values of the J-integral can then be obtained through appropriate selections of the perturbation fields $\{\ \mathbf{q}^K,\ \delta l^K\}$ and of the domains of integration, Ω^K, as detailed in the following sections.

2.3.1 Crack-front integral expression for the energy release

The profiles of quantities along the crack-front are defined in term of their nodal values and interpolating shape functions. For each element-edge along the crack-front, we identify an isoparametric coordinate η, and define shape functions $N_I(\eta)$, where $I = 1, 2, 3$ denote the three nodes of the element-edge. In general, we express the value of any quantity g at location η along the element-edge j, in terms of the nodal values of g and shape functions as

$$g(\eta) = N_I(\eta) < g_I >_j, \tag{2.20}$$

where the summation convention (from $I = 1$ to 3) is implied also for the capital subscripts, and $< g_I >_j$ is the value of g at the local node I of the element-edge j.

In particular, the explicit form of shape function interpolations for the curvilinear coordinate s, the point-wise value of the J-integral, and the perturbation field δl^K are

$$s(\eta) = N_Q(\eta) < s_Q >_j , \tag{2.21}$$

$$ds = \frac{ds}{d\eta} d\eta = \frac{dN_Q}{d\eta} < s_Q >_j d\eta , \tag{2.22}$$

and

$$J(\eta) = N_P(\eta) < J_P >_j , \tag{2.23}$$

$$\delta l^K(\eta) = N_L(\eta) < \delta l^K_L >_j , \tag{2.24}$$

where $< J_P >_j$ and $< \delta l^K_L >_j$ are the point-wise values of J and the K-th perturbation field, respectively, at local nodes P and L of element-edge j. Combining (2.21 – 2.24) with (2.18), we obtain an expression for the energy release associated with the K-th perturbation field, $\delta\pi^K$, in terms of the nodal values of J and δl:

$$\delta\pi^K = \sum_{j=1}^{M} \{ - \int_{-1}^{1} N_L(\eta) < \delta l^K_L >_j N_P(\eta) < J_P >_j \frac{dN_Q}{d\eta} < s_Q >_j d\eta \}, \tag{2.25}$$

where we have transformed the integral along the crack to the sum of the integrals

over each element-edge along the crack.

2.3.2 Domain integral expression for the energy release

Evaluation of (2.19) requires the definition of the domain of integration, Ω^K, and of the perturbation field $\mathbf{q}^K$. For the K-th perturbation pattern, we define the domain of integration, Ω^K, to be centered on the K-th crack-front node, as the union of all elements with at least one node B, located within a distance ρ from node K, as shown in figure 2-4 (c).

The perturbation field $\mathbf{q}^K$ at point P in figure 2-5 (a), where $P = \{s, r, \theta\}$, is taken to be:

$$\mathbf{q}^K = q_t^K \cdot \mathbf{t}(s) + q_n^K \cdot \mathbf{n}(s) + q_m^K \cdot \mathbf{m}(s), \tag{2.26}$$

with $q_t^K = q_m^K \equiv 0$. The magnitude of q_n^K depends on the distance of point P from the crack, r, and on the position, s, of P^* with respect to node K, the center of the crack perturbation (see figure 2-5 (b). We express q_n^K as

$$q_n^K = f_r(r) \cdot f_s^K(s), \tag{2.27}$$

where f_r and f_s^K must be continuous functions within the domain of integration and must vanish at the boundary of the domain. Consistent with the definition of the $\mathbf{q}^K$-functions, $f_s^K(s) \equiv \delta l^K(s)$ and $f_r(r = 0) = 1$ for each perturbation. For clarity, we have used the notation $\delta l^K(s)$ in the evaluation of $\delta\pi^K$ by the crack-front integrals, and $f_s^K(s)$ in the evaluation of $\delta\pi^K$ by the 3-D volume integral.

To evaluate $\delta\pi^K$, numerical integration of (2.19) is performed using 4-point quadrature [13] within each element of Ω^K. Any nodal variable "$\mathbf{g}$" can be interpolated at the integration points of the tetrahedral element j by means of the quadratic tetrahedral shape functions $\mathcal{N}^I$ and nodal values $< \mathbf{g}^I >_j$ as

$$\mathbf{g}(c_m) = \mathcal{N}^I(c_m) < \mathbf{g}^I >_j, \tag{2.28}$$

where c_m are the natural coordinates, and the implied sum on I extends from 1 to 10. The field variables W and σ_{ij} are available at the integration points of the tetrahedral element from the finite element solution of the boundary value problem. The displacement gradient $u_{i,k}$ is evaluated at the integration points of element j, in terms of nodal values of the cartesian components of the displacement field, $< u_i^I >_j$, as

$$u_{i,k} = C_k^I < u_i^I >_j, \tag{2.29}$$

where the coefficients C_k^I are obtained through a shape function based procedure detailed in the appendix.

The specific technique used to evaluate the gradient of the $\mathbf{q}^K$-functions affects the effectiveness of the procedure in certain topologies of FE meshes of a cracked structure, as discussed in chapter 5. We have found that a direct evaluation of the derivatives $q_{j,i}^K$ based on nodal interpolation of q_j^K followed by shape function differentiation, is not adequate for certain tetrahedral FE meshes, as further detailed in chapters 3 and 5. A superior technique to evaluate $q_{j,i}^K$, independent of the mesh topology, is described in chapter 4.

2.3.3 Evaluation of the point-wise J-values

Equations (2.19) and (2.25) are equivalent representations of the energy release associated with the K-th perturbation pattern. Equating the RHS of (2.19) and (2.25) for each pattern of perturbation, we obtain a system of N equations in N in unknowns J_I,

$$[A_I^K]\{J_I\} = \{\delta\pi^K\}. \tag{2.30}$$

Solving the system of equations (2.30) gives the nodal values of the J-integral, which provide point-wise definition of J on C through (2.23) .

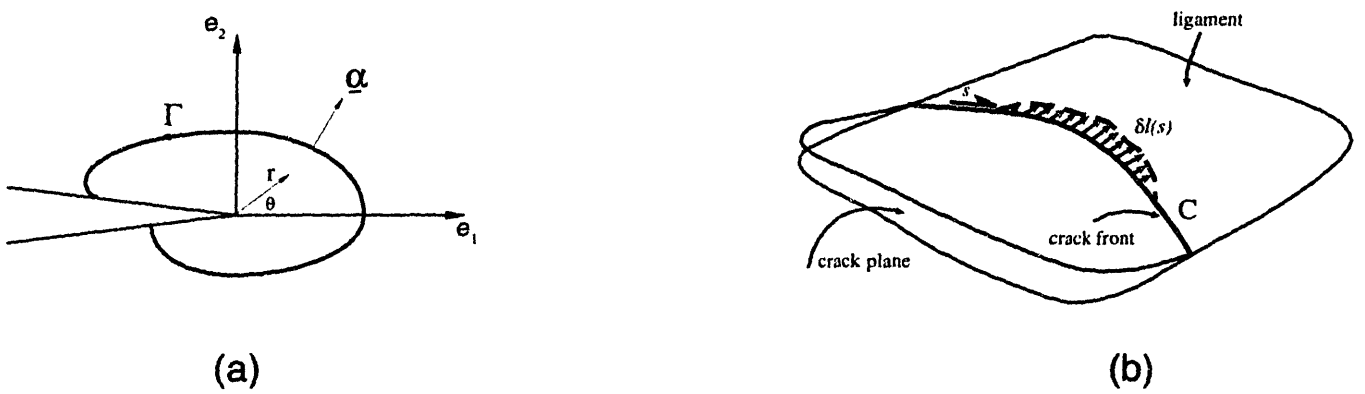

Figure 2-1: Definition of the J-integral. (a) Contour for the evaluation of the J-integral. (b) Crack-front perturbation field $\delta l(s)$.

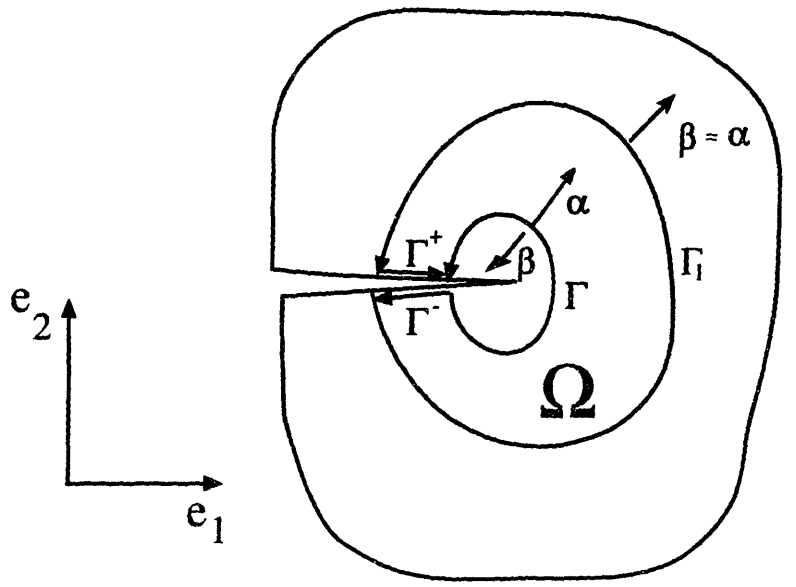

Figure 2-2: Two-dimensional formulation. Domain of integration Ω .

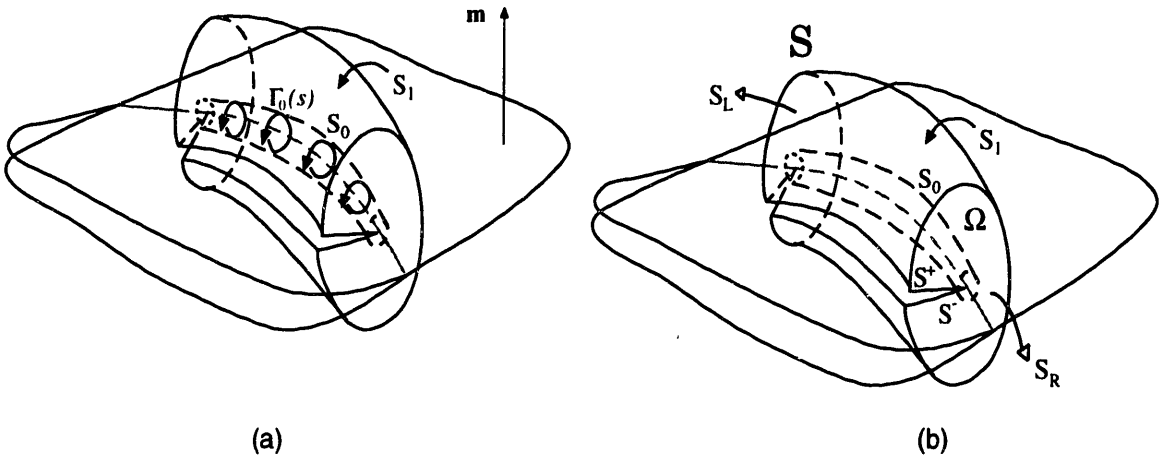

Figure 2-3: Three-dimensional formulation. (a) Surfaces S_0 and S_1 enclosing the crack-front. (b) 3-D domain of integration, Ω in the limit $\Gamma_0 \to 0$.

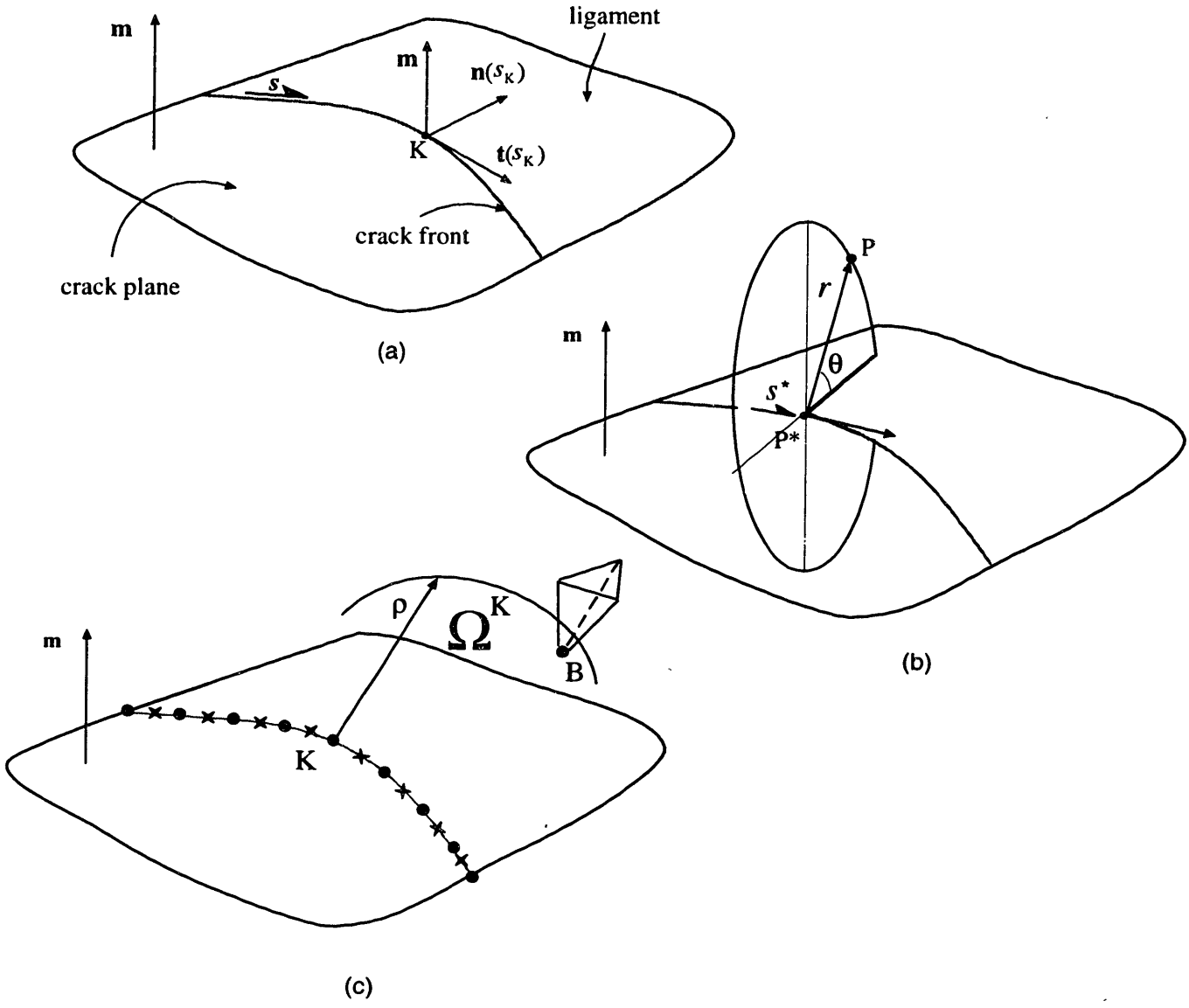

Figure 2-4: Definition of the crack-front. (a) Toroidal coordinate system localized at position K along the crack-front. (b) Projection of location P onto the crack-front. (c) Definition of the domain of integration for evaluating the energy release rate.

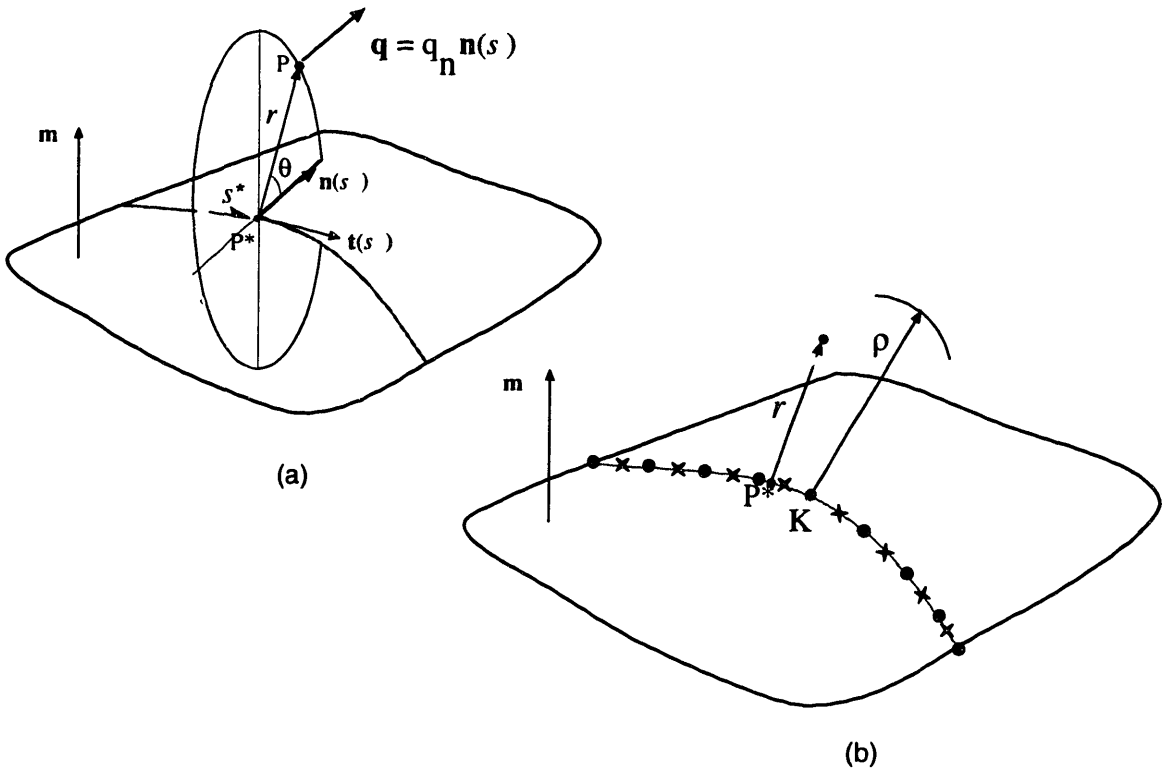

Figure 2-5: Definition of the perturbation field $\mathbf{q}(\mathbf{X})$.

Chapter 3

A "straightforward" method for computing point-wise J-values, or how not to proceed

3.1 Finite element formulation

The details specific to the FE formulation of a "straightforward" implementation of the domain integral method are discussed in this section. A toroidal coordinate system is defined at each of the N nodes along the crack-front as described in chapter 2.

3.1.1 Crack-front integral representation of the energy release

To evaluate (2.25) for each of the N perturbation patterns, we use quadratic shape functions $N_I(\eta)$ along the crack-front element-edges defined by

$$N_I(\eta) \equiv \begin{cases} 0.5 \cdot \eta(1-\eta) & \text{if } I = 1, \\ (1-\eta^2) & \text{if } I = 2, \\ 0.5 \cdot \eta(1+\eta) & \text{if } I = 3. \end{cases}$$

We define the K-th perturbation pattern $\delta l^K(s)$ in terms of nodal perturbation based on the location of the R^{th} node as

$$< \delta l_R^K > \equiv \begin{cases} 1 & \text{if } K = R, \\ 0 & \text{if } K \neq R. \end{cases}$$

When interpolated using quadratic shape functions, the perturbation pattern centered on a corner node is spread over two adjacent element-edge crack-front segments, while the perturbation pattern centered on a mid-side node is spread over one element-edge crack-front segment. Perturbation patterns $\delta l^K(s)$ and $\delta l^L(s)$ centered on corner node K and mid-side node L, respectively, are shown in figure 3-1 (b). Equation (2.25) can be written more compactly as

$$\delta\pi^K = \sum_{j=1}^{M} < \delta l_L^K >_j < J_P >_j < s_Q >_j B_{LPQ}, \tag{3.1}$$

where

$$B_{LPQ} \equiv -\int_{-1}^{1} N_L(\eta) \cdot N_P(\eta) \cdot \frac{dN_Q(\eta)}{d\eta}\, d\eta \tag{3.2}$$

can be explicitly evaluated for all combination of indices. Writing (3.1) for all the N perturbation patterns, we obtain a system of N equations in N unknown nodal values of J_I, as expressed in (2.30). The term A_I^K can be evaluated as

$$A_I^K = \sum_{m_I} < \delta l_L^K >_j < s_Q >_j B_{LPQ}, \tag{3.3}$$

where $P(I) = 2$ if I is a mid-side node, and either 1 or 3, depending the position of corner node I in element j, and m_I denote the crack-front element segment[s] to which node I belongs.

3.1.2 Domain integral evaluation of the energy release

The radial and tangential variation of $q_n^K = f_r(r) f_s^K(s)$ associated with the K-th perturbation are defined as (see figures 3-1(a) and 3-1(b)):

$$f_r(r) = e^{-[r/(r-\rho)]^2}, \tag{3.4}$$

and

$$f_s^K(s) \equiv \delta l^K(s), \tag{3.5}$$

where ρ is the nominal radius of Ω^K. A radial variation of the form $e^{-[r/(r-\rho)]^2}$ has been selected because this function has unit value and zero derivatives at $r = 0$, and vanishes along with its derivatives at the boundary of the domain, $r = \rho$.

In the "straightforward" procedure, the gradients of the $\mathbf{q}^K$-functions, $\partial q_i^K / \partial x_k$ are evaluated at the integration points by the same procedure used to evaluate the displacement gradients (2.29), based on the nodal values within element j of the $\mathbf{q}^K$-field and the derivatives of the quadratic shape functions:

$$q_{i,k} = C_k^I < q_i^I >_j, \tag{3.6}$$

where the coefficients C_k^I are obtained through the shape-function-based procedure detailed in the appendix.

3.2 Results and discussion

The performance of the "straightforward" procedure was evaluated on an edge-cracked model in plane strain subjected to uniform remote tension. The crack geometry is a straight through-thickness crack with $a/b = 0.5$, $h/b = 3.0$ and $a/W = 0.5$, as shown in figure 3-2. Commercially-available packages ABAQUS/Pre [14] and Pro/MESH [15] were used to create the meshes, and ABAQUS/Standard [17] was used as the FE solver. Two tetrahedral meshes, a regular mesh from ABAQUS/Pre and an irregular mesh from Pro/MESH, as shown in figures 3-3 (a) and 3-3 (b), respectively,

were created for this crack geometry. Second-order isoparametric (10-noded) tetrahedral elements were used. A mesh using 20-noded brick elements of comparable mesh density was also created for the cracked geometry, as shown in figure 3-4 (c). To incorporate the square-root singularity at the crack tip, quarter-point elements [16] were used along the crack-front in all the meshes. Nodal J-values were obtained for both tetrahedral meshes using the "straightforward" procedure. As a comparison, nodal J-values were also obtained from the brick mesh using the domain integral option available for brick elements in ABAQUS/Standard. The J-values were normalized with respect to the plane-strain values reported by Tada, *et al.* [19], which we denote as "J_{th}" (see also subsection 5.1.1). In figure 3-2, the normalized pointwise J-values, J/J_{th}, are shown as a function of the normalized curvilinear coordinate (x/W) for all three cases. While the brick mesh provides predictions in good agreement with the theoretical estimate, the regular and irregular tetrahedral meshes give very unsatisfactory results.

3.3 Reasons for the poor performance

The poor performance of the "straightforward" implementation on the irregular tetrahedral mesh can be attributed to the reasons elaborated below.

Firstly, different mesh connectivity at crack nodes introduces artificial oscillations in energy release rate. Figures 3-4 (d) and 3-4 (e) show crack-plane mesh connectivity at the crack-tip, and schematically indicate the location of integration points for tetrahedral and brick meshes. For the irregular tetrahedral mesh, there are elements which have an edge along the crack-front, while others have only a vertex on the crack-front. The locations of the integration points, relative to the node about which the perturbation is centered, are inherently different for these two cases. The relative positions of the integration points in the tetrahedral mesh do not provide a "firewall" for spatially localizing the perturbation field and its discontinuous tangential gradients, as in the brick mesh. This causes artificial oscillations in the calculated energy release rate, and the base of the perturbation field is not wide enough to average out

these oscillations.

Secondly, in the irregular tetrahedral mesh we have a fine mesh along the crack-front, but substantially larger elements in the far-field. For this mesh topology, the quadratic shape functions produce large discontinuous gradients of the crack-front perturbations. These are distorted within the crack-front elements by the intrinsically unstructured topology of the irregular tetrahedral meshes with a steep mesh gradient perpendicular to the crack-front. Figure 3-4 (a) shows the perturbation field which results from interpolating the nodal $\mathbf{q}^K$ values using 3-D quadratic shape functions. The quadratic tetrahedral shape functions form artificial "pockets" in the $\mathbf{q}$-field, thereby leading to undesirable representation of the gradients of the perturbation field. This problem is largely confined to the irregular mesh with a topology similar to the one used in the study and is a relatively smaller effect compared to the effect of using node-based perturbation pattern with quadratic shape-functions. A study of the relative effects of the problems described above is presented in chapter 5.

It can be summarized that using a node-based crack-front perturbation pattern with quadratic shape-function interpolation is the main problem with the "straight-forward" method. In irregular tetrahedral meshes with the mesh topology used in the study, we also have the relatively minor issue of obtaining accurate gradients of the perturbation field using the node-based approach. In the next chapter we propose an alternative method to obtain the point-wise J-values. We use piece-wise linear perturbation patterns centered at every alternate node on the crack-front and obtain J-values at these nodes along the crack-front. This is the major expedient which significantly increases the accuracy of the computed J-values. To obtain accurate gradients of the perturbation field in the extreme but representative cases of tetrahedral meshing, we also propose to compute the gradients of the perturbation field analytically and to evaluate the domain integral, we identify a core domain $\tilde{\Omega}^K$ and a periphery domain $\bar{\Omega}^K$, within Ω^K. We use "analytical-gradients" within $\tilde{\Omega}^K$, and within $\bar{\Omega}^K$, we use a node-based method for computing the gradient as detailed in this chapter, with a minor modification by using linear shape-functions instead of quadratic shape-functions. The details of the proposed method are presented in the

next chapter. We then proceed to examine other alternative perturbation patterns and also compare the methods of evaluating the domain integral in chapter 5.

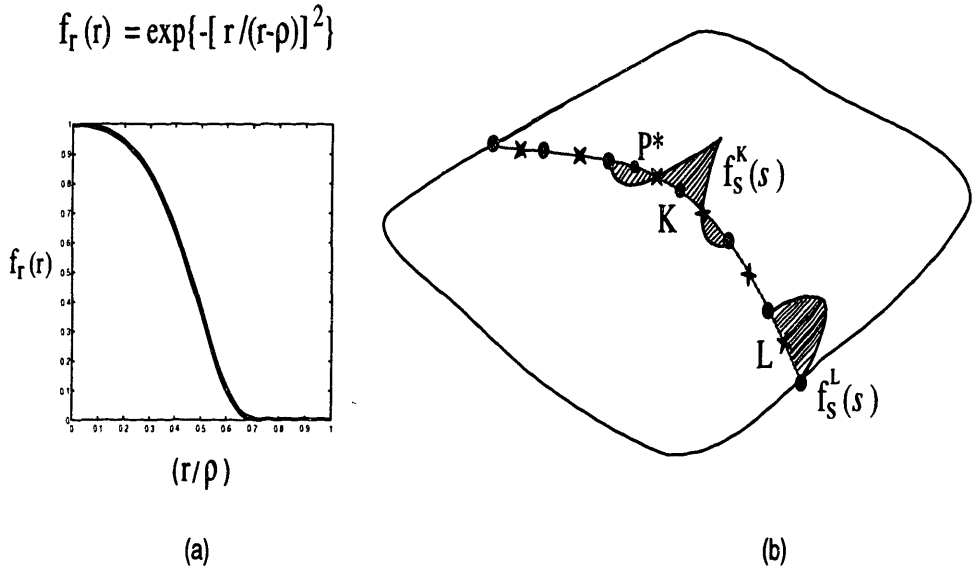

Figure 3-1: Components of the perturbation field for the "straightforward" method. (a) Radial variation of $q_n^K(s,r)$, $f_r(s)$. (b) Schematic of tangential variation of $q_n^K(s,r)$, $f_s^K(s)$.

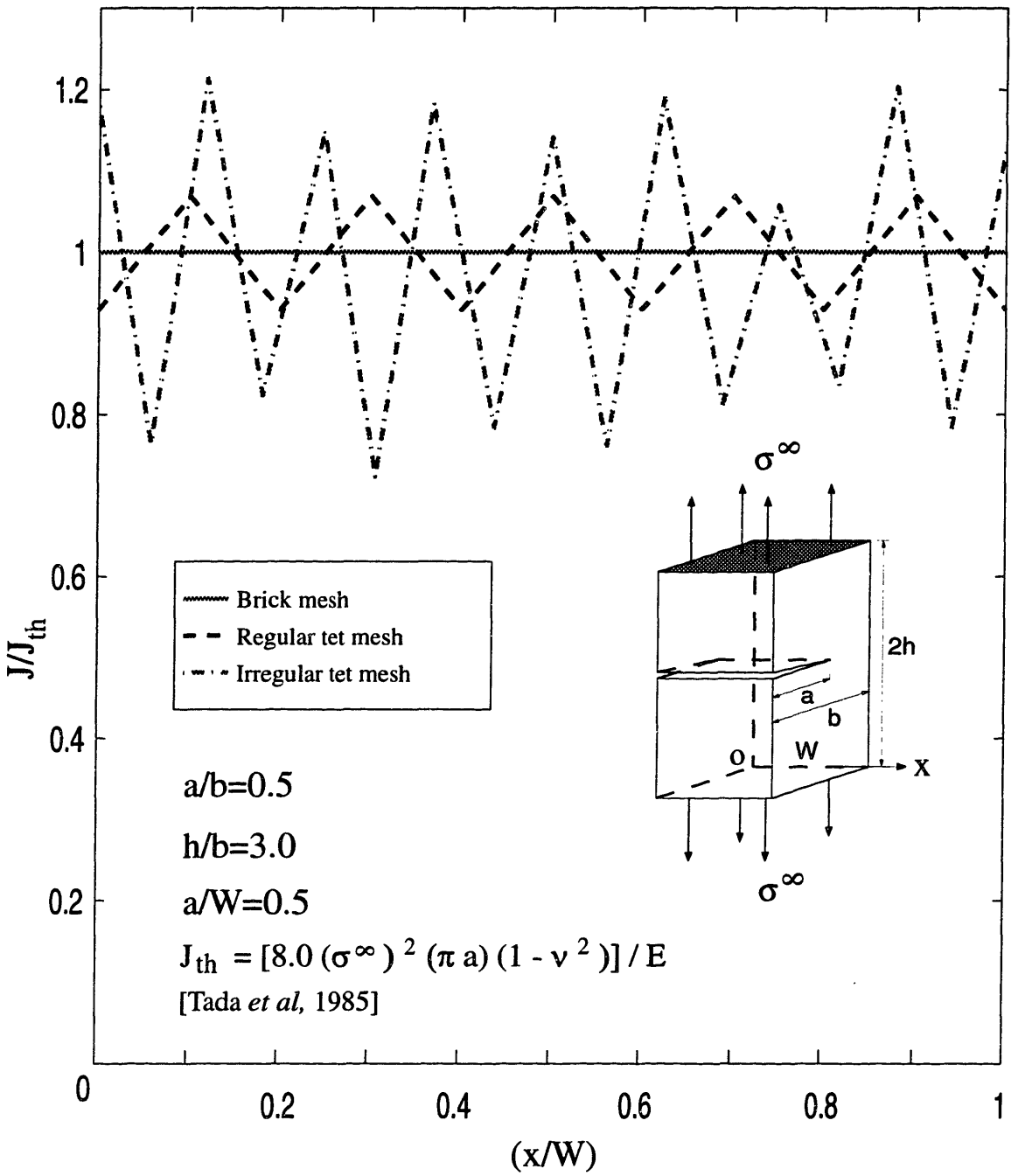

Figure 3-2: Point-wise J-integral values obtained by the "straightforward" method. The edge-crack in plane strain is subjected to uniform remote tension of magnitude σ^{∞}.

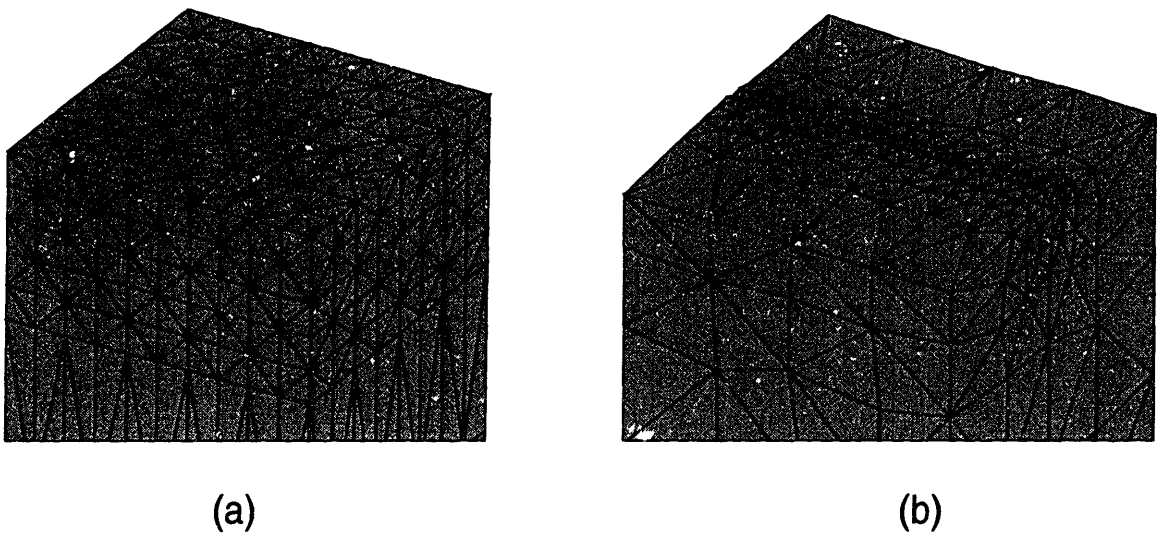

Figure 3-3: Crack-plane view of the finite element meshes for the edge-crack in plane strain. (a) Regular tetrahedral mesh obtained from ABAQUS/Pre. (b) Irregular tetrahedral mesh obtained from Pro/Mesh.

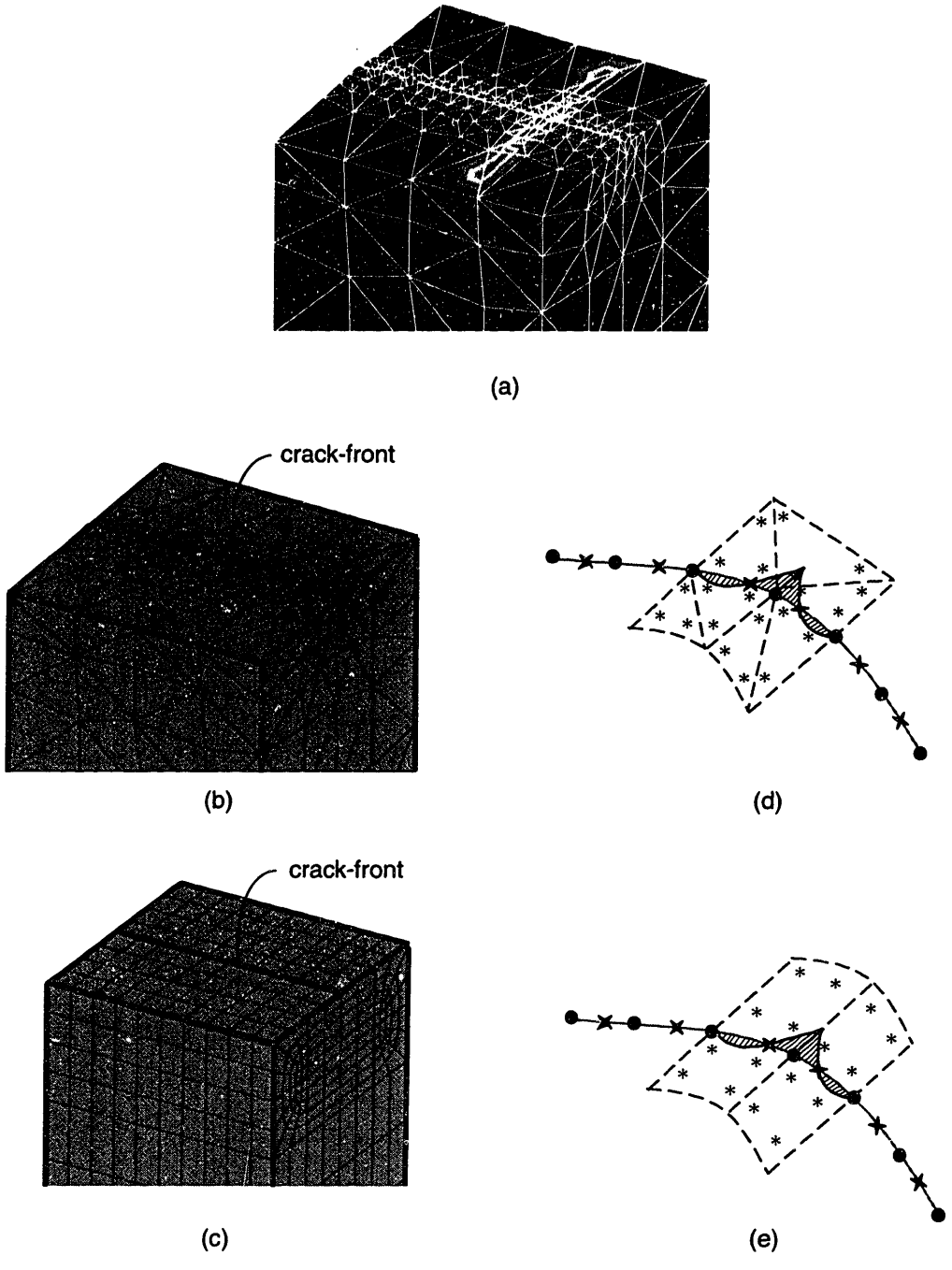

Figure 3-4: J-integral evaluation by the "straightforward" method for the edge-crack in plane strain. (a) Undesirable interpolations of the q_n^K function by the quadratic tetrahedral shape functions. (b) Crack plane view of the irregular tetrahedral mesh generated by Pro/MESH. (c) Crack plane view of the brick mesh. (d) Integration points for the tetrahedral elements at the crack tip. (e) Integration points for the brick elements at the crack tip.

Chapter 4

Proposed method for computing point-wise J-values

4.1 Finite element formulation

An alternative method is proposed in this section to overcome the difficulties encountered with the "straightforward" method. A comparison of other possible alternative methods is presented in chapter 5. The inherent oscillations present due to the meshing property detailed in section 3.3 can be suppressed by considering nodal J-values at every alternate corner node. This also provides a well-conditioned $[A]$-matrix, as defined in (2.30), which can be easily inverted to obtain the nodal J-values.

While no perturbation fields are centered at the mid-side nodes, the mid-side nodes are still used in order to obtain accurate deformation fields and to accurately define curved crack-fronts. We extend the base of each perturbation pattern to span four adjacent crack-front element-edges, as shown in figure 4-1. Hence we now have $N_J = (N+3)/4$ perturbation patterns centered on every alternate corner node along the crack-front. This introduces the modest restriction that an even number of element-edges should be used to define the crack-front, in order to obtain a complete set of perturbation patterns.

4.1.1 Crack-front integral representation of the energy release

To evaluate (2.25) for each of the N_J perturbation patterns, we use piecewise linear interpolations for the crack perturbation patterns instead of quadratic shape functions. The use of linear interpolation functions for $\delta l^K(s)$ and $J(s)$ reduces the number of locations having discontinuous gradients in the perturbation field and minimizes the distortion of the perturbation field by the intrinsically unstructured tetrahedral meshes, as shown in figure 4-1. The nodes forming the crack-front are sequentially numbered from 1 to N. The K-th perturbation pattern, $\delta l^K(s)$, is defined in terms of its value at nodes along the crack front:

$$< \delta l_I^K > \equiv \begin{cases} 1 & \text{if } I = K, \\ 0 & \forall \text{ nodes } I \text{ on the crack-front such that } I \leq K-4 \text{ and } I \geq K+4, \end{cases}$$

and a linear variation (with respect to s) from unity at node K to zero at nodes $(K+4)$ and $(K-4)$. The perturbation pattern $\delta l^K(s) = f_s^K(s)$ centered on node K is shown in figure 4-1. Expression (3.3) still holds, but it is now evaluated only at alternate corner nodes, with B_{LPQ} re-computed using the linear interpolation functions, and the index P being either 1 or 3, depending on the position of corner node I in element j.

4.1.2 Domain integral representation of the energy release

We define the core domain $\tilde{\Omega}^K$ as the union of all elements which have all their nodes within radius ρ from node K. We also define a periphery domain $\bar{\Omega}^K$ as the union of elements which have at least one node within distance ρ from node K and at least one node further than ρ from node K, as shown schematically in figure 4-2. The domain of integration is defined as $\Omega^K = \tilde{\Omega}^K \cup \bar{\Omega}^K$. The radial and tangential variation of q_n^K associated with the K-th perturbation are still defined as detailed in subsection 3.1.2, except that $\delta l^K(s) = f_s^K(s)$ is now a piecewise linear function spread over four crack-front element-edges, as shown in figure 4-1.

Expression (2.19) is then evaluated via element-by-element numerical quadrature

over Ω^K. The field variables W and σ_{ij} are available at the integration points of the tetrahedral element from the finite element solution of the boundary value problem. The displacement gradient, $u_{i,k}$ is evaluated at the integration points, through the shape function procedure described in subsection 3.1.2 and detailed in the appendix.

Different procedures are used to evaluate the gradients of the $\mathbf{q}^K$-function for elements in the core domain, $\tilde{\Omega}^K$, and for elements in the periphery domain, $\bar{\Omega}^K$. For elements within the core domain $\tilde{\Omega}^K$, we evaluate the gradients of the $\mathbf{q}^K$-functions, at each integration point, analytically, by differentiating expressions (3.4) and (3.5). Details of the derivation of analytical expressions for $\partial q_i^K/\partial x_j$ are given in appendix. For each element within the periphery domain $\bar{\Omega}^K$, we evaluate $\partial q_i^K/\partial x_j$ based on the value of the $\mathbf{q}^K$-field at the four corner nodes, and using linear shape functions to interpolate $\mathbf{q}^K$, so that the resulting perturbation gradient is constant over the element. This method overcomes undesirable effects linked to the interpolation of the perturbation gradient by the quadratic tetrahedral shape functions in tetrahedral meshes with a topology similar to the irregular tetrahedral mesh used in the study in chapter 3 (Fig. 3-4 b). This approach leads to a significant improvement in the accuracy of the results, especially in the irregular tetrahedral mesh, as shown in chapter 5. Note that we continue to use nodal interpolation for $\mathbf{q}^K$ within $\bar{\Omega}^K$. The nodal basis is particularly useful when the boundary of Ω^K meets a free surface or a bounding surface of the model, where it is necessary to impose the constraint $\xi \cdot \mathbf{q}^K = 0$, where ξ is the outward normal to the surface.

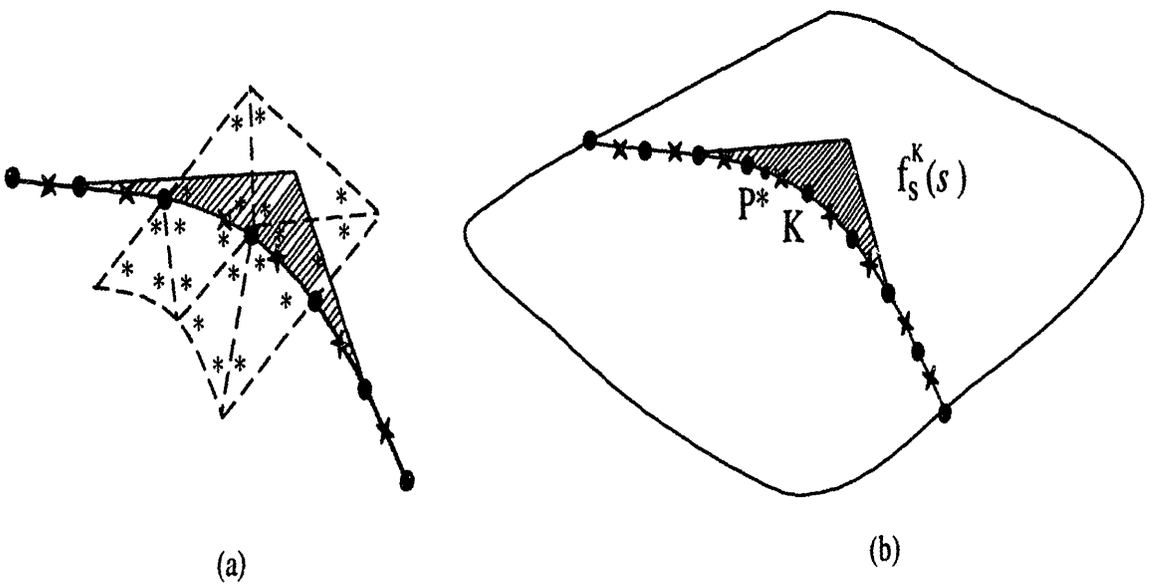

Figure 4-1: Crack-front perturbation for the proposed method, with $\delta l(s)$ spread over 4 adjacent crack-front element-edges. (a) Schematic of integration points for irregular tetrahedral elements at the crack tip. (b) Tangential variation of $q_n^K(s,r)$, $f_s(s)$.

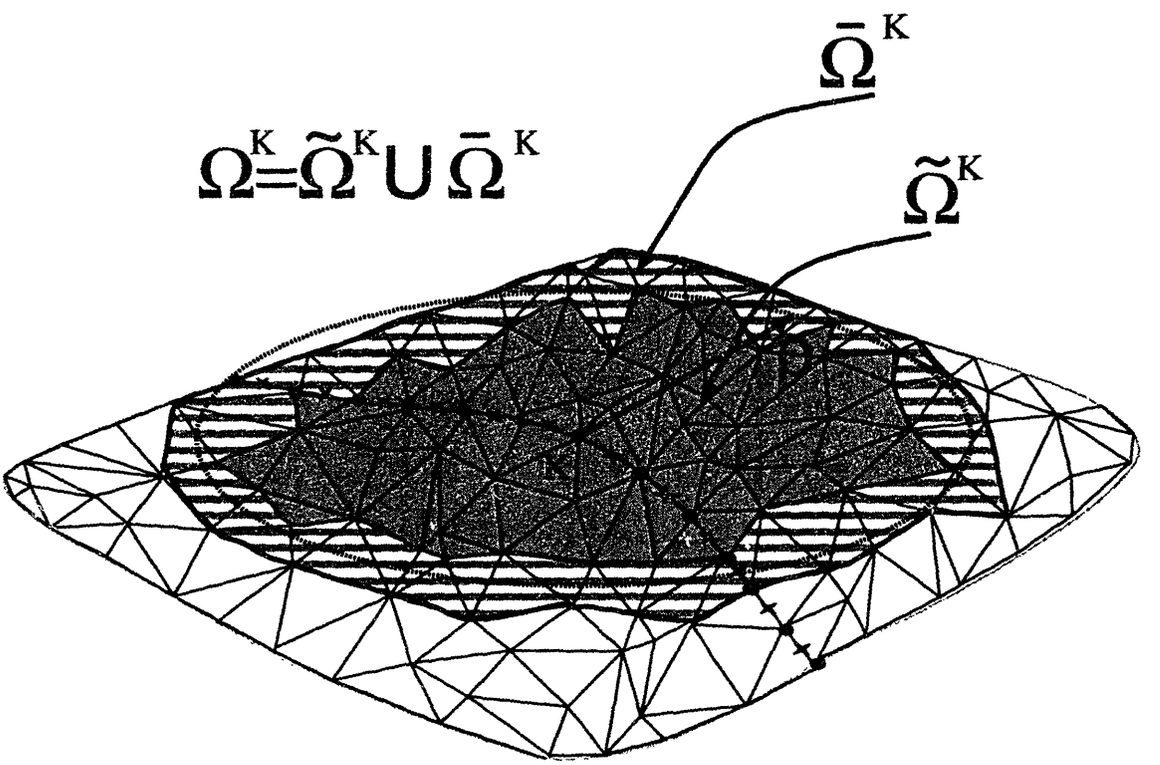

Figure 4-2: Schematic illustration of domain of integration Ω^K for the proposed method. Core domain $\tilde{\Omega}^K$ and periphery domain $\bar{\Omega}^K$ are schematically identified.

Chapter 5

Comparison of alternative methods for computing nodal J-values

A "straightforward" method to obtain nodal J along the crack-front was discussed in chapter 3, and possible reasons for the poor performance were also detailed. A method to compute the nodal J-values accurately was proposed in chapter 4. In this chapter we examine the relative merits and demerits of alternative schemes for computing J and also attempt to provide a relative basis for the choice of a computation scheme.

5.1 Crack-front perturbations

For a crack-front comprised of N nodes, the method to obtain N_J values of the J-integral along the crack-front $\{J_1, J_2, .., J_K, .., J_{N_J}\}$ requires the definition of N_J perturbation patterns, $\{\delta l^1(s), \delta l^2(s), .., \delta l^K(s), .., \delta l^{N_J}(s)\}$, centered on each of the N_J nodes as discussed in section 2.3. In the "straightforward" implementation in chapter 3, $N_J = N$ perturbation patterns were defined at all the N nodes forming the crack-front. These perturbation patterns were formed by quadratic shape functions (see section 3.1.1). Subsequently, from the analysis of the straight through-thickness crack in plane strain (see section 3.2), it was observed that different mesh connectivity

at crack nodes introduced artificial oscillations in energy release rate, and the base of the perturbation field was not wide enough to average out these oscillations. Also, the quadratic shape functions produce large discontinuous gradients of the crack-front perturbations. A factor accounting for the poor performance of the "straightforward" implementation is the perturbations based on quadratic shape functions. Hence, we consider piece-wise linear crack-front perturbations as an alternative. The primary form of these piece-wise linear perturbation patterns is one whose base is spread over two element-edges, as shown in figure 5-1 (a). We center these perturbations on every corner node, thus defining $N_J = (N+1)/2$ perturbation patterns and hence obtain $N_J = (N+1)/2$ values of J along the crack-front. The perturbation patterns are centered on corner nodes only, as this provides a well-conditioned $[A]$-matrix, as defined in (2.30), which can be easily inverted to obtain the nodal J-values. While no perturbation fields are centered at the mid-side nodes, the mid-side nodes are still used in order to obtain accurate deformation fields and to accurately define curved crack-fronts. This perturbation pattern is referred as "two-element-linear" in our further discussion. The finite element implementation of this perturbation pattern is similar in all respects to the implementation detailed in section 4.1.1. The performance of this perturbation pattern is discussed at the end of this chapter. The next alternative crack-front perturbation is to spread the base of the piece-wise linear perturbation pattern to four element-edges as in the proposed method (see section 4.1) and to obtain a well-conditioned $[A]$-matrix, as defined in (2.30), we define $N_J = (N+3)/4$ perturbation patterns centered on every alternate node on the crack-front, and hence obtain $N_J = (N+3)/4$ values of J along the crack-front. This pattern is referred to as the "four-element-linear" in our further discussion. The finite element implementation of the "four-element-linear" pattern is detailed in section 4.1.

5.2 Evaluation of the domain integral

To evaluate the energy release, $\delta\pi^K$, for each perturbation pattern, numerical integration of (2.19) is performed using 4-point quadrature [13] within each element of

Ω^K (see section 2.3.2). In a "straightforward" implementation, the displacement gradients and the gradients of $\mathbf{q}^K$ are evaluated at the integration points, in terms of nodal values of the cartesian components of the displacement field and perturbation field $\mathbf{q}^K$, respectively. The procedure uses the tetrahedral quadratic shape functions and is detailed in the appendix. The summation is then carried out in the domain Ω^K, with the field variables W and σ_{ij} obtained at the integration points of the tetrahedral element from the finite element solution of the boundary value problem. This "node-based" computation of the gradient of $\mathbf{q}^K$ based on the quadratic tetrahedral shape functions led to the formation of pockets for certain mesh topology, as discussed in section 3.3. We refer to this method of evaluating the domain integral as "node-based-quadratic" in our further discussion. An alternative method to compute to the domain integral is to obtain the gradients of $\mathbf{q}^K$ using the same "node-based" approach, but using linear tetrahedral shape functions in the procedure detailed in the appendix. Hence we now have constant gradients of $\mathbf{q}^K$ within an element. We refer this method using linear shape functions for $\mathbf{q}^K$ as "node-based-linear" in future. Another alternative method, which eliminates all the undesirable interpolations, is to compute the gradients analytically and then use them in the quadrature, as discussed in the proposed method in section 4.1.2. This requires the definition of the two subdomains $\tilde{\Omega}^K$ and $\bar{\Omega}^K$, use of the analytical gradients within $\tilde{\Omega}^K$, and computation of the gradient of $\mathbf{q}^K$ based on nodal interpolation, using the procedure detailed in the appendix; in particular, linear shape functions were used, as discussed in section 4.1.2. We denote this method of evaluating the domain integral as "analytical-gradients" in our further discussion.

5.3 Results and discussions

The performance of the two crack-front perturbation patterns-"two-element-linear" and "four-element-linear", along with the three possible methods of evaluating the domain integral-"node-based-quadratic", "node-based-linear" and "analytical-gradients" was evaluated on an edge-cracked model in plane strain subjected to uniform remote

tension. The crack geometry is a straight through-thickness crack with $a/b = 0.5$, $h/b = 3.0$ and $a/W = 0.5$, as shown in figure 5-2. One-half of the specimen geometry was modeled, and commercially-available packages ABAQUS/Pre [14] and Pro/MESH [15] were used to create the meshes. ABAQUS/Standard [17] was used as the FE solver. Three tetrahedral meshes, a regular mesh from ABAQUS/Pre and two irregular meshes from Pro/MESH, as shown in figures 5-3 (a), (b) and (c), respectively, were created for this crack geometry. The first irregular tetrahedral mesh is one in which the far-field element size is of the order of 2 times the crack-tip element size. The second irregular tetrahedral mesh is one in which the far-field element size is of the order of 8 times the crack-tip element size. These two meshes were used to study the effect mesh gradient perpendicular to the crack-front in obtaining accurate J-values along the crack-front. Second-order isoparametric (10-noded) tetrahedral elements were used. To incorporate the square-root singularity at the crack tip, quarter-point elements [16] were used along the crack-front in all the meshes. The J-values were normalized with respect to the plane-strain values reported by Tada, *et al.* [19], which we denote as "J_{th}" (see also subsection 5.1.1).

5.3.1 Two element-edge crack-front perturbation patterns

The J-profile obtained using the "two-element-linear" crack-front perturbations are shown in figures 5-4, 5-5 and 5-6 for the regular, irregular and irregular mesh with a steep mesh gradient perpendicular to the crack-front, respectively. In all the cases, the domain of integration was taken as $\rho/a = 0.4$, so that it extends to the far-field in all the meshes. In each of the figures, the profiles obtained by the three domain integral options are also shown. We can observe from figure 5-4 that when the meshing is structured and regular, as in the case of the regular tetrahedral mesh from ABAQUS/Pre [14], there are strong corner-node to corner-node oscillations in the computed J-values. Typical J-oscillations are +/- 5% of the mean value. Topologically, this can be attributed to the fact that the two adjacent corner nodes on the crack front are not really identical [they alternately attach to 4 or 8 tetrahedral elements with faces on the crack plane], and the oscillations support that notion. The

J-profile for the irregular tetrahedral mesh does not show as pronounced an oscillation as does the regular mesh (compare figure 5-5 or 5-6 with 5-4). This can be attributed to the fact that, while two adjacent crack-front corner nodes are topologically different, the difference tends to "even out" in the far field, where each node in a tetrahedral element is topologically similar. We do not observe this "evening out" in the regular mesh because of the structured nature of the mesh. When we consider an extreme case of tetrahedral meshing, we do observe substantial oscillations as shown in figure 5-6. Hence we conclude from the above results that the "two-element-linear" perturbation patterns have pronounced shortcomings in computing J-values for regular meshes and produce inherent oscillations in other cases. Focusing on figure 5-5 and figure 5-6, we see that computing the domain integral by "analytical-gradients" yields slightly better results than from either node-based interpolation of $\mathbf{q}^K$, at least for the two element-edge crack-front perturbations.

5.3.2 Four element-edge crack-front perturbation patterns

Figure 5-7 shows the J-profile for the regular tetrahedral mesh using the three methods of evaluating the domain integral, but this time for four-element-edge crack-front perturbations; again we consider the domains of $\rho/a = 0.4$ for computing J. We observe that the mean values of J are accurate to 99% of the theoretical value of J, with essentially zero gradient. All three domain integration methods produce very similar results. From result of the irregular tetrahedral mesh shown in figure 5-8, we can observe slight variation in the J-profile, but the variation is less than 1 % using all the three options of evaluating the domain integral. Results from the irregular tetrahedral mesh with steep mesh gradients are shown in figure 5-9; we can observe that evaluating the domain integral by "analytical-gradients" produces a more accurate values of J than the other methods. For this method, the computed J is approximately 97% of J_{th}.

Hence we conclude from these numerical experiments that the "four-element-linear" crack-front perturbation pattern is necessary for obtaining accurate J-values. While the "best" choice of the method for evaluating the domain integral may not

be obvious from this study, nevertheless the "analytical-gradients" produces results which are quite accurate in most cases. Especially in the extreme but presumably representative of a tetrahedral mesh of a cracked body with very fine mesh along the crack-front, but substantially larger elements in the far-field (*e.g.*, with linear dimensions of 8 or more times larger than those of the crack-front elements), the "analytical-gradients" method has been shown to be effective and superior in obtaining accurate J-profiles. We now proceed to use the "analytical-gradients" method, in conjunction with the "four-element-linear" crack-front perturbation pattern in our further analyses in the next few chapters.

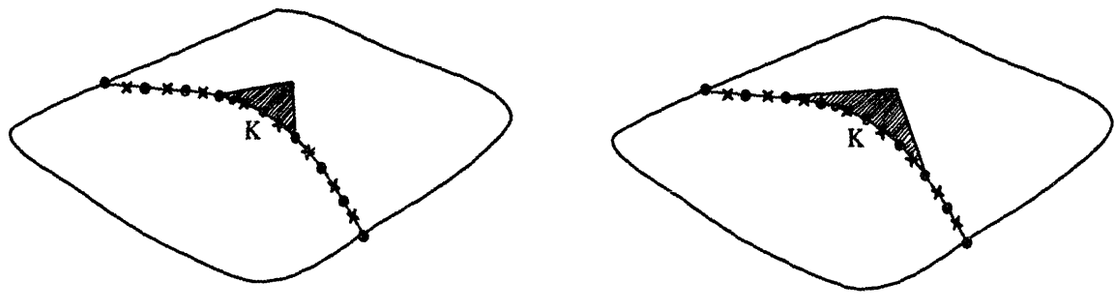

(a) (b)

Figure 5-1: Piece-wise linear crack-front perturbation patterns. (a) Perturbations with base spread over two element-edges. (b) Perturbations with base spread over four element-edges.

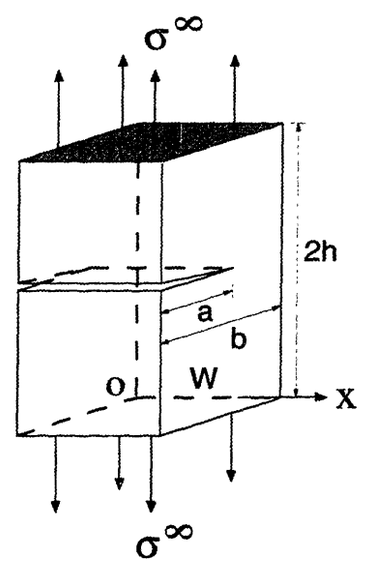

a/b=0.5

h/b=3.0

a/W=0.5

Figure 5-2: Model of the edge-crack in plane strain. The straight through-thickness crack is subjected to a uniform far-field normal traction σ^{∞}. The dimensional ratios are $a/b = 0.5$, $h/b = 3.0$ and $a/W = 0.5$.

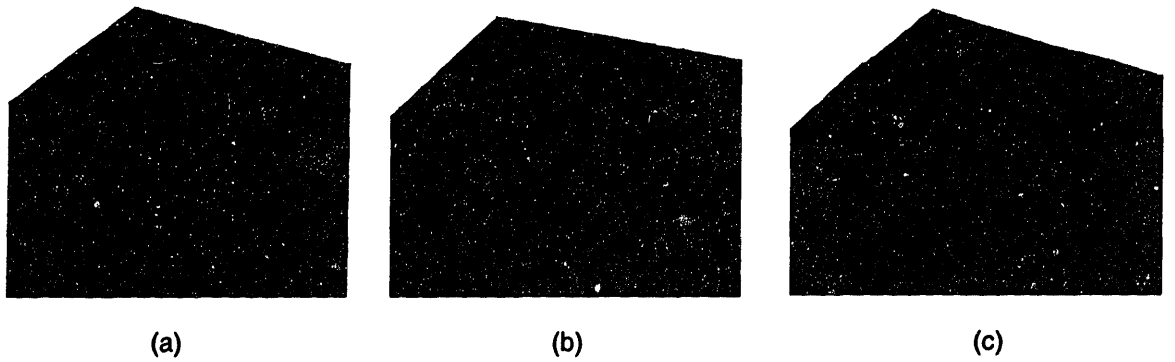

Figure 5-3: Tetrahedral finite element meshes of the straight though-thickness crack in plane strain. (a) Regular mesh from ABAQUS/Pre. (b) Irregular mesh from Pro/MESH. (c) Irregular mesh from Pro/MESH with steep mesh gradient perpendicular to the crack-front.

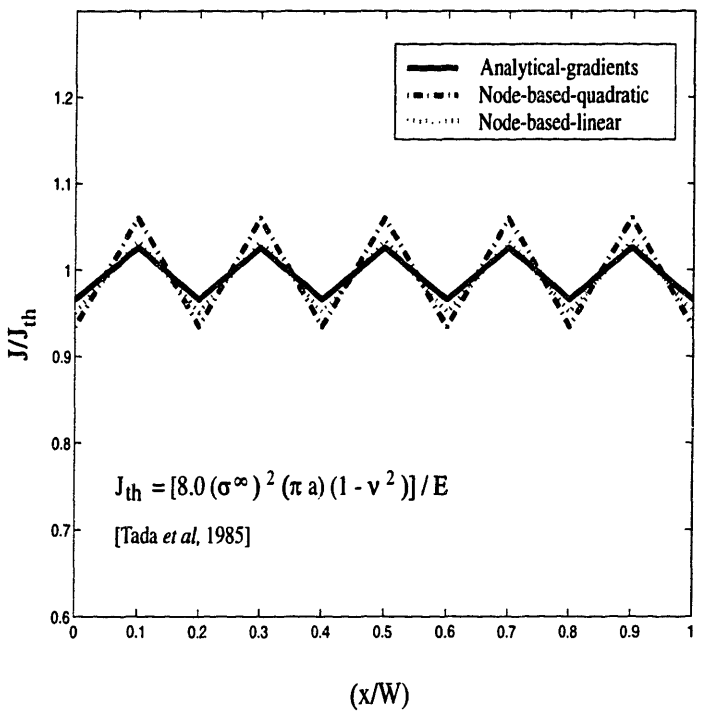

Figure 5-4: Straight through-thickness crack in plane strain. J-profile for the two element-edge based crack-front perturbation for the regular tetrahedral mesh (Fig. 5-3 a) from ABAQUS/Pre. The domain radius $\rho/a = 0.4$.

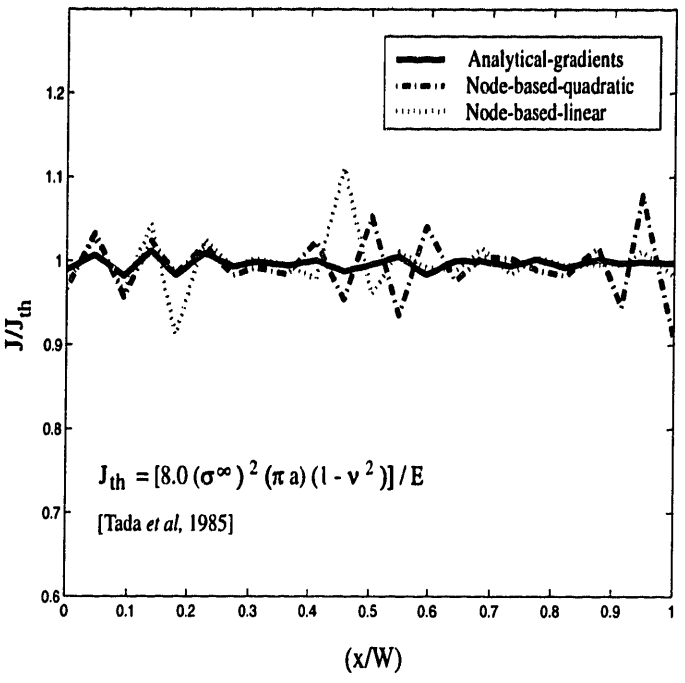

Figure 5-5: Straight through-thickness crack in plane strain. J-profile for the two element-edge based crack-front perturbation for the irregular tetrahedral mesh (Fig. 5-3 b) from Pro/MESH. The domain radius $\rho/a = 0.4$.

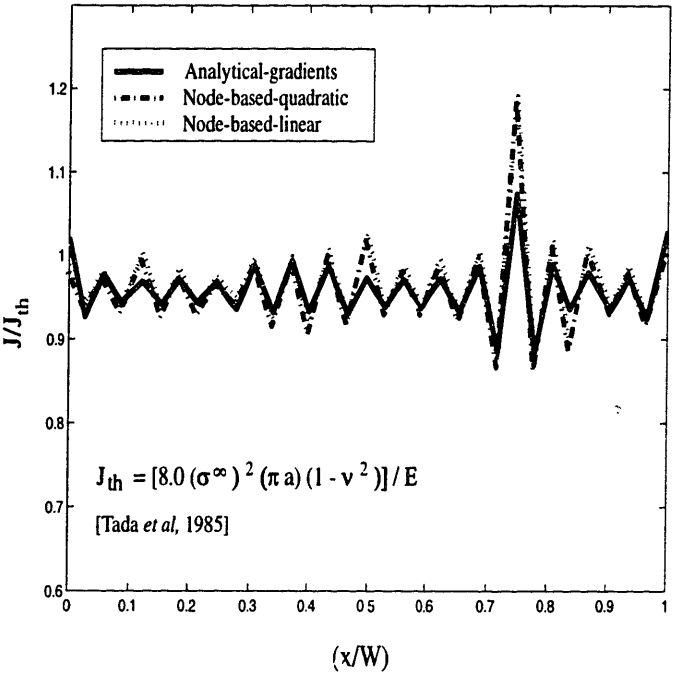

Figure 5-6: Straight through-thickness crack in plane strain. J-profile for the two element-edge based crack-front perturbation for the irregular tetrahedral mesh (Fig. 5-3 c) from Pro/MESH. The domain radius $\rho/a = 0.4$.

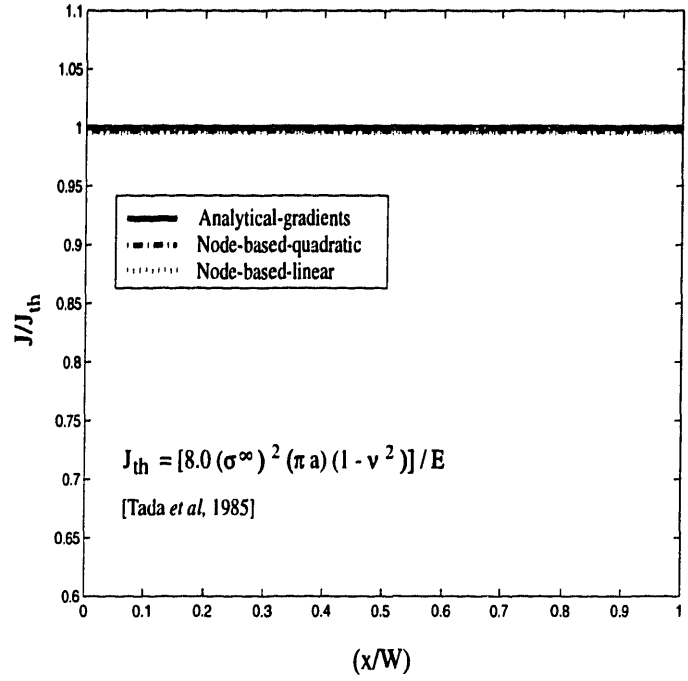

Figure 5-7: Straight through-thickness crack in plane strain. J-profile for the four element-edge based crack-front perturbation for the regular tetrahedral mesh (Fig. 5-3 a) from ABAQUS/Pre. The domain radius $\rho/a = 0.4$.

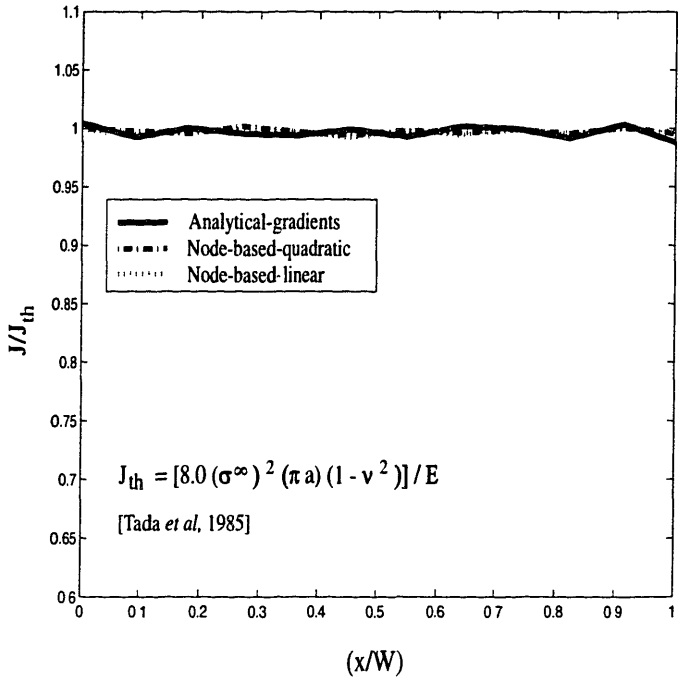

Figure 5-8: Straight through-thickness crack in plane strain. J-profile for the four element-edge based crack-front perturbation for the irregular tetrahedral mesh (Fig. 5-3 b) from Pro/MESH. The domain radius $\rho/a = 0.4$.

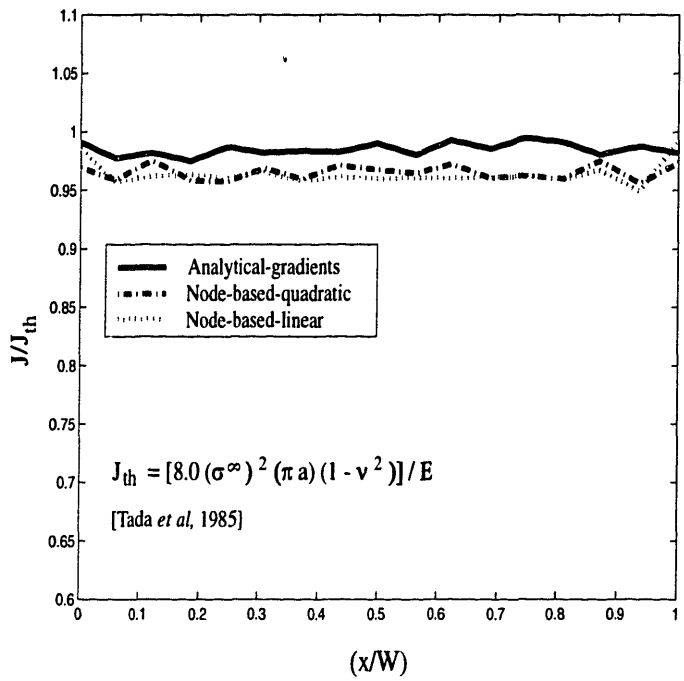

Figure 5-9: Straight through-thickness crack in plane strain. J-profile for the four element-edge based crack-front perturbation for the irregular tetrahedral mesh (Fig. 5-3 c) from Pro/MESH. The domain radius $\rho/a = 0.4$.

Chapter 6

Elastic analysis

The proposed method detailed chapter 4 is validated on well-known crack geometries. Commercially-available packages ABAQUS/Pre [14] and Pro/MESH [15] were used to create the meshes, and ABAQUS/Standard [17] was used as the FE solver. Two tetrahedral meshes–a regular mesh from ABAQUS/Pre and an irregular mesh from Pro/MESH, were created for each of the crack geometries, and the method was validated on both meshes. The tetrahedral mesh results were also compared to the predictions obtained with brick meshes of comparable mesh density, using the domain integral option in ABAQUS/Standard.

6.1 Edge-cracked model under uniform remote tension

An edge-cracked model with characteristic dimensional ratios $(a/b) = 0.5$, $(h/b) = 3.0$, and $(a/W) = 0.5$, as shown in figure 6-1, was considered. The model was subjected to uniform far-field tension (mode I). Second-order isoparametric (10-noded) tetrahedral elements were used to mesh this geometry. To obtain the square root singularity at the crack tip, quarter-point elements [16] were used at the crack tip in both the tetrahedral meshes. A finer mesh was used near the crack, with crack-tip elements ten times smaller than far-field elements. The fine mesh at the crack tip

was used to better capture the steep crack-tip gradients. The point-wise J-integral values were calculated for two lateral boundary conditions: (1) plane-strain, and (2) traction-free lateral surfaces, resulting in a fully 3-D solution.

6.1.1 Plane strain

The model was subjected to plane strain boundary conditions, and uniform remote tension was applied (mode I). The results were compared with the plane strain solution of Tada, *et al.* [19]. For the single edge-notch specimen, the stress intensity factor is given by

$$K_I = \sigma^\infty \sqrt{\pi a} \cdot F(a/b), \tag{6.1}$$

where σ^∞ is the applied remote tensile stress, and the geometry correction factor $F(a/b) = 2.83$ for $(a/b) = 1/2$. For plane strain, the point-wise J-integral is constant along the crack-front. Hence the expression for the J-integral becomes

$$J_{th} = (1 - \nu^2)K_I^2/E = 8.0 \cdot [(\sigma^\infty)^2(\pi a)(1 - \nu^2)]/E, \tag{6.2}$$

where E is the modulus of elasticity and ν is the Poisson's ratio. Figure 6-1 shows the plot of nodal J-values obtained for the tetrahedral elements using the proposed method for domain size $\rho/a = 0.7$, normalized by the values quoted by Tada, *et al.* We define $J_{ave} = \int J dx/W$ to represent the average value of J along the crack-front. The J_{ave}/J_{th} obtained from the regular mesh was accurate to 0.5% of the theoretical value, and the oscillations were within 0.5%, while values of J_{ave}/J_{th} obtained from the irregular mesh were accurate to 0.5% of the theoretical value, with oscillations within 1%. The values obtained via the proposed technique were in close agreement with those obtained using second-order brick elements of equivalent mesh density, also with quarter-point elements at the crack tip. To verify domain independence of the J-integral [7], three contours of radii ρ varying from 50% to 80% of the crack length, were considered in the irregular mesh. The corresponding results in figure 6-2 clearly demonstrate the domain-independence of the J-integral.

6.1.2 3-D analysis with one free surface

The model was subjected to a 3-D stress state, with one of the lateral surfaces being traction-free and the other a symmetry plane, as shown in figure 6-3. Nakamura and Parks [22] have described the three-dimensional stress state near the free surface from very detailed full-field finite element analysis of the near-tip region of a thin isotropic plate. The obtained J-values were normalized with respect to the theoretical plane strain J-value. The J profiles from all three meshes are shown in figure 6-3. The local value of J theoretically vanishes at the free-surface, as the corner singularity is weaker than $1/\sqrt{r}$ [22], but to capture this behavior very fine meshes are needed. The irregular tetrahedral mesh closely follows the J values from the brick mesh, and the variations are within 2-3 %.

6.2 Penny-shaped crack in a round bar

The method was further validated on a circular crack front. A penny-shaped crack of radius a, in a round bar of radius b, as shown figure 6-5, was subjected to far-field tension. One-eighth of the specimen geometry was modeled. Crack-plane details of the displaced meshes for the circular crack, meshed with bricks, as well as regular and irregular tetrahedral elements, are shown in figure 6-4. Quarter-point crack tip elements were again used. The point-wise J-values are compared to the axisymmetric solution quoted by Tada, *et al.* [19], for which

$$K_I = (2/\pi)\ \sigma^{\infty}\ \sqrt{\pi a} \cdot \mathcal{F}(a/b), \tag{6.3}$$

where σ^{∞} is the applied uniform remote tensile stress, and the factor $\mathcal{F}(a/b) = 1.09$ for $(a/b) = 1/2$. Due to symmetry, J remains constant along the crack-front, with magnitude

$$J_{th} = (1-\nu^2)K_I^2/E = 4.75 \cdot [(\sigma^{\infty})^2(a/\pi)(1-\nu^2)]/E. \tag{6.4}$$

The results obtained using the brick meshes and the regular and irregular tetrahedral meshes were normalized with respect to the theoretical value (6.4), and are shown

in figure 6-5. The mean values of the solutions obtained with the two tetrahedral meshes agree with (6.4) to 0.5% for the regular tetrahedral mesh, and to 1% for the irregular tetrahedral mesh. The oscillations for the regular mesh were within 1% of the mean value, while for the irregular mesh we observe oscillations within 3% of the mean value.

6.3 Semi-elliptical surface crack in a finite-thickness plate

Surface cracks are an important class of crack geometries which are crucial to life prediction in aircraft, pressure vessels and other structures. Typically, surface cracks propagate sub-critically by fatigue, with semi-elliptical or near-semi-elliptical crack fronts. A crack with a semi-elliptical front has varying local radius of curvature along the crack front, thus representing a good test to assess the performance of the proposed method on a general 3-D curvilinear crack-front in space. Hence, a planar semi-elliptical surface crack is considered here to further validate the accuracy of the method. A comparison of the relative user-time needed to generate brick, regular and irregular tetrahedral meshes for this geometry is shown in table 6.1. For this relatively simple 3-D crack configuration, a reduction factor in user time between 15 and 20 is evident for automatic tetrahedral meshing; the speed-up factor for more complex geometries can be much larger.

Newman and Raju [20] have obtained stress-intensity factors from detailed finite element models of semi-elliptical surface cracks using a nodal force method. Here, a semi-elliptical surface crack with aspect ratio $a/c = 1/3$ and maximum relative depth $a/t = 0.5$ was considered for analysis. The crack was subjected to uniform remote tension in Mode-I loading. Displaced meshes of the FEM models for the semi-elliptical surface crack are shown in figure 6-6. The stress intensity factor K_I, at any point ϕ

along the semi-elliptical crack, can be expressed as

$$K_I = \sigma^{\infty} \sqrt{[(\pi \frac{a}{Q})]}\ F(\frac{a}{t}, \frac{a}{c}, \phi), \tag{6.5}$$

where σ^{∞} is the applied stress, a is the crack depth, ϕ is the parametric angle of the ellipse, Q is the shape factor of an ellipse and is given by the square of the complete elliptical integral of the second kind [21]; for $(a/c) = 1/3$, $Q = 1.123$. The value of the boundary correction factor F for the specific crack geometry ($a/c = 1/3$ and $a/t = 0.5$) was obtained as a function of ϕ from Raju and Newman [20]. Results from the FEM models using brick elements, regular and irregular tetrahedral elements, along with the reported values of Newman and Raju, are shown in figure 6-7, using $(1 - \nu^2)K_I^2 = EJ$.

An accurate solution to this crack configuration presents a rapid variation in K_I near the boundary layer of the corner singularity created by the orthogonal intersection of the crack-front with a traction-free surface [22]. The effect of this boundary layer on the K_I-field was not considered in this study, as it has been shown that the mesh refinement at the surface required to capture the boundary layer does not the affect features of the general K_I solution in the interior [20]. The maximum value of K_I occurs at $\phi = \pi/2$, in agreement with Newman and Raju's observations. The average value of the K_I-solution was in agreement to within 2% of Newman and Raju's findings (which have been reported to be accurate to $1-3\%$ [20]), and the oscillations were within 2% and 4% of the mean value for the regular and irregular tetrahedral meshes, respectively.

MESH	NUMBER OF NODES	TOTAL TIME		
		Meshing	Setting up	Running
Irregular tets (Pro/MESH)	10,000	20 sec	30 min	10 min
Regular tets (ABAQUS/Pre)	28,000	10 min	1 day	30 min
Bricks	15,000	20 min	> 2 days	2 hours

Table 6.1: Approximate total user mesh generation time and size of the problem for the semi-elliptical surface crack in a finite thickness plate.

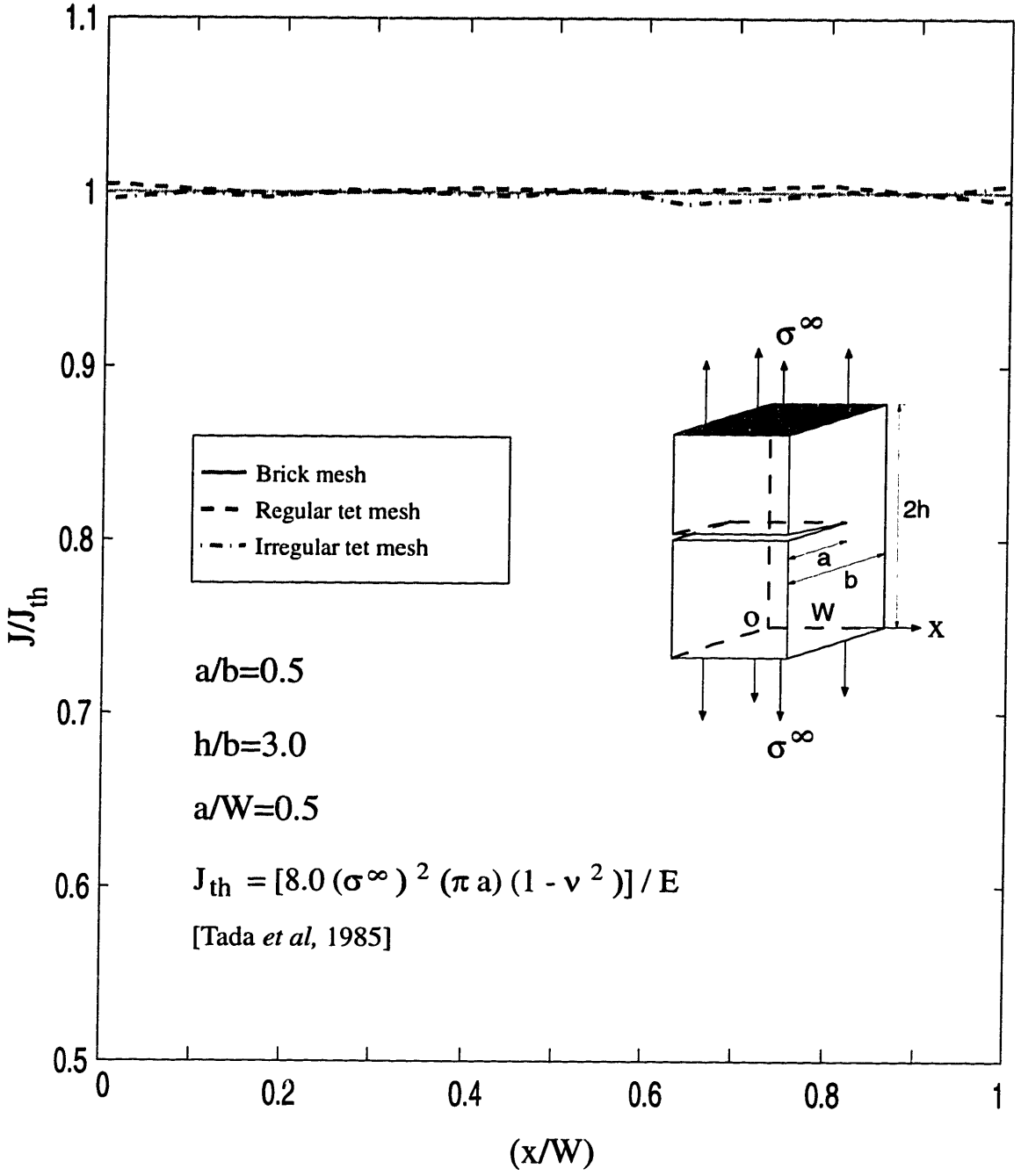

Figure 6-1: Point-wise J-integral values obtained by the proposed method. The edge-crack in plane strain is subjected to uniform remote tension of magnitude σ^{∞}. Radius of the domain integral used in the tetrahedral meshes is $\rho/a = 0.7$.

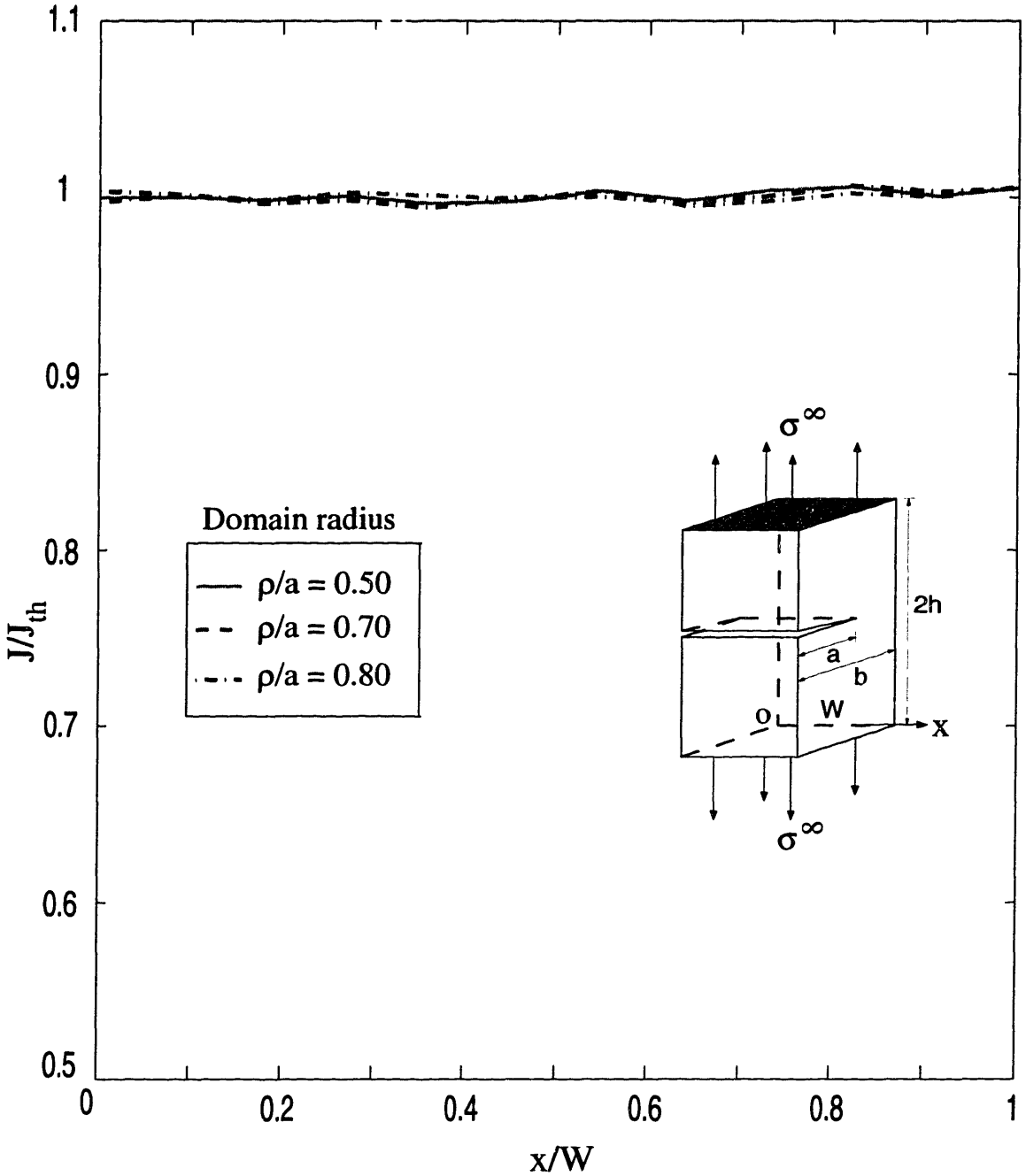

Figure 6-2: Domain independence of the computed J-values. The irregular tetrahedral mesh of an edge-crack in plane strain is subjected to uniform remote tension of magnitude σ^{∞}. Geometric ratios are as in Fig. 6-1.

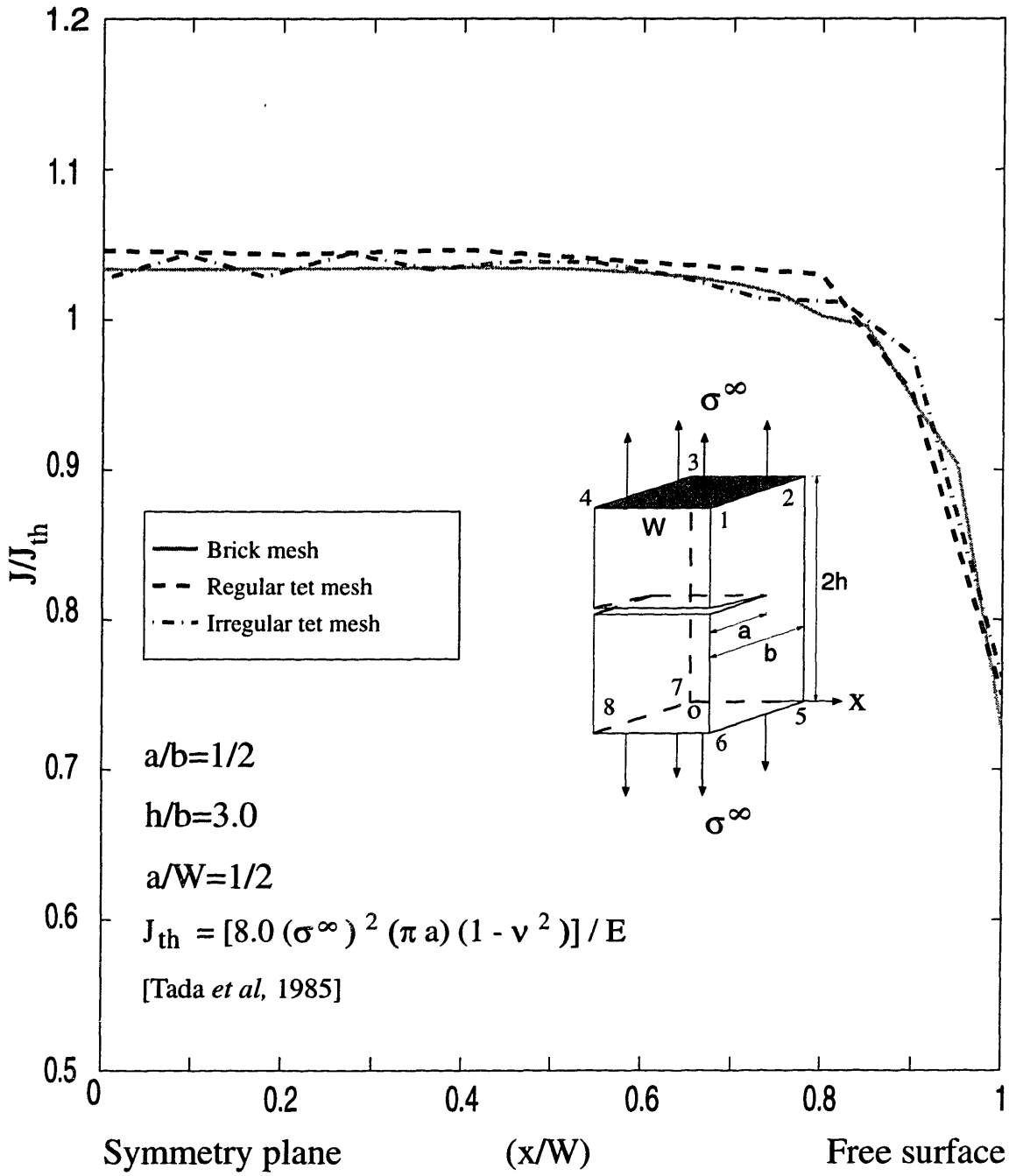

Figure 6-3: Point-wise J-integral values obtained by the proposed method. The edge-crack is subjected to uniform remote tension of magnitude σ^{∞}. Face (1-2-5-6) is a free surface, and face (4-3-7-8) is a symmetry plane.

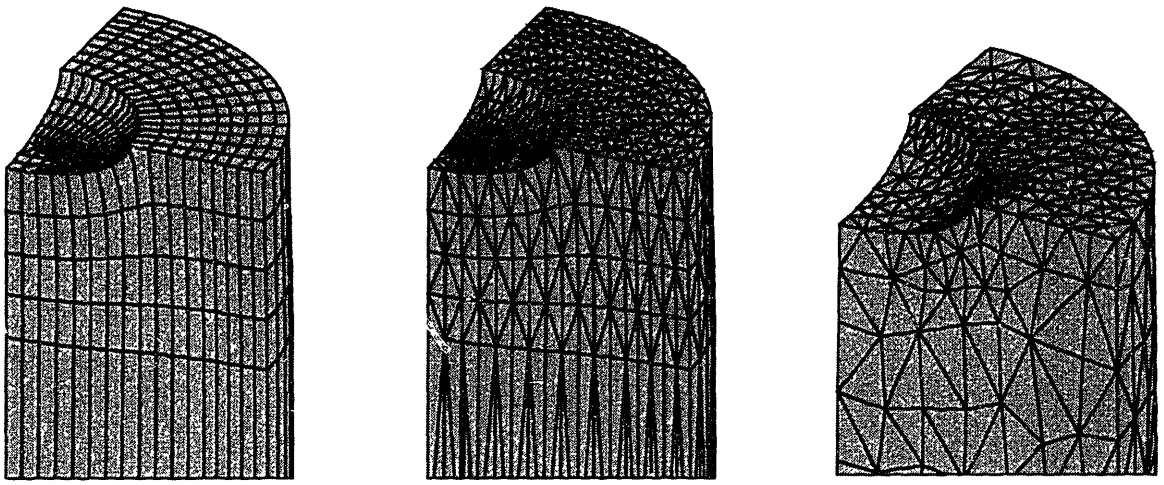

Figure 6-4: Displaced meshes of the penny-shaped crack in a round bar. The model with symmetry planes at 90^o is subjected to uniform remote tension. (a) Brick mesh. (b) Regular tetrahedral mesh obtained from ABAQUS/Pre. (c) Irregular tetrahedral mesh obtained from Pro/Mesh.

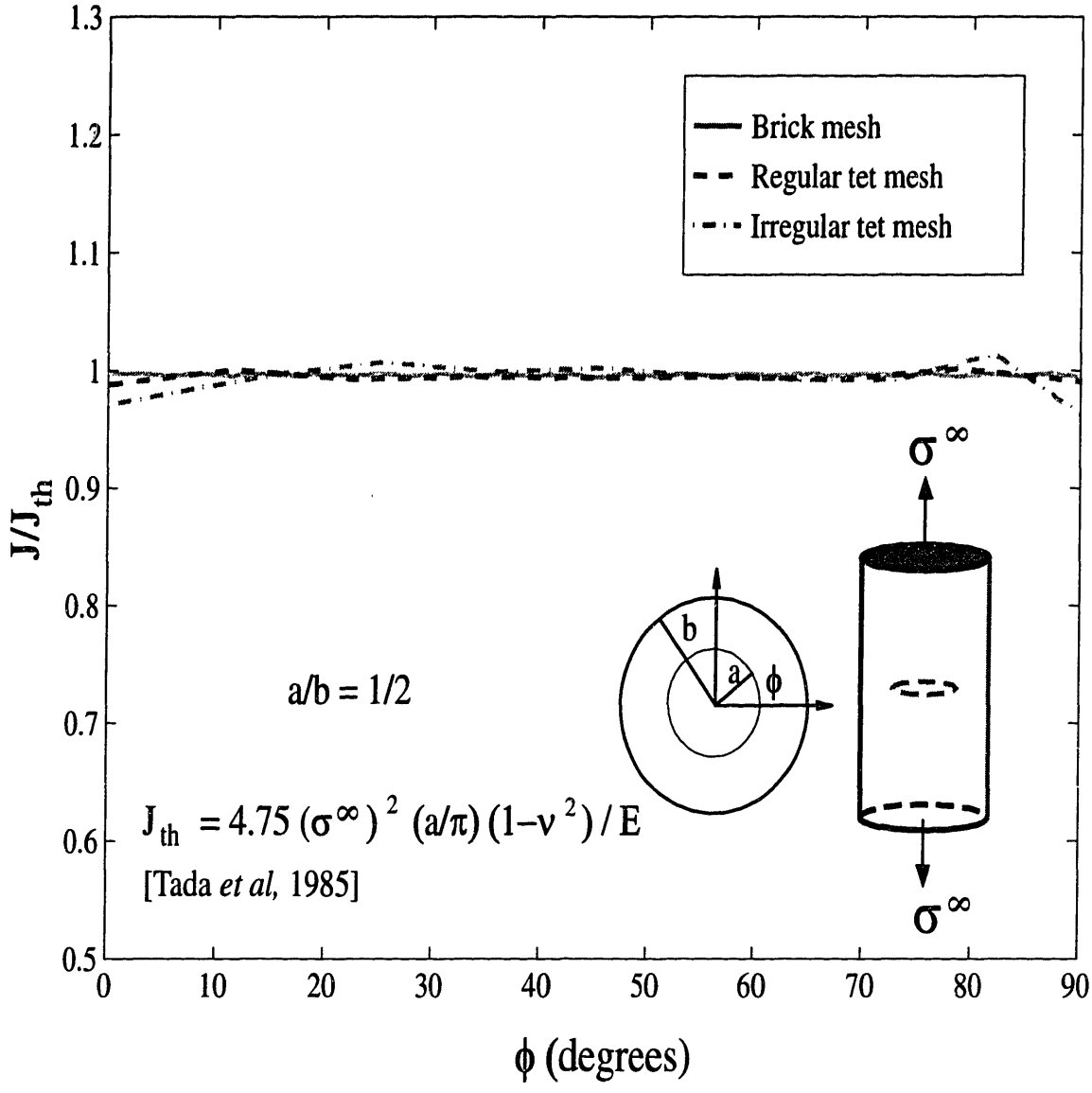

Figure 6-5: Point-wise J-integral values for a penny-shaped crack in a round bar. The penny-shaped crack is subjected to uniform remote tension (Mode I) of magnitude σ^{∞}.

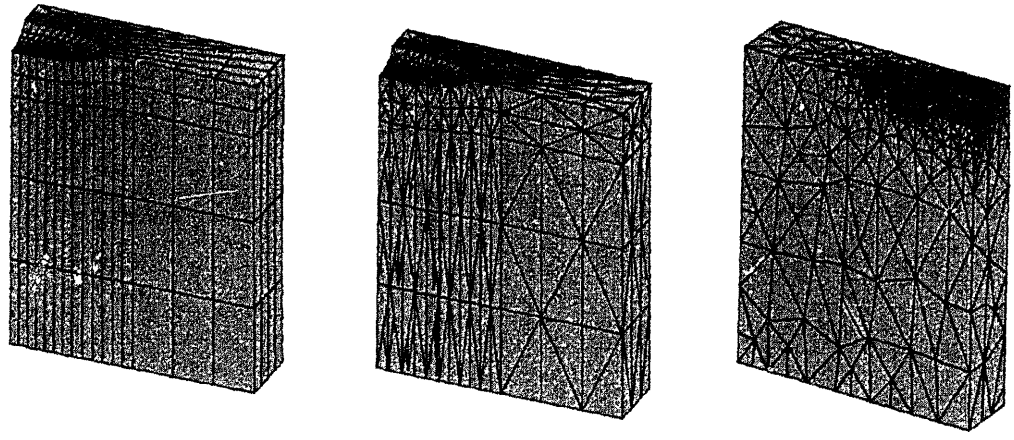

(a) (b) (c)

Figure 6-6: Displaced meshes of the semi-elliptical surface crack in a finite thickness plate. The models are subjected to uniform remote tension. One-quarter of the plate is modeled. (a) Brick mesh. (b) Regular tetrahedral mesh obtained from ABAQUS/Pre. (c) Irregular tetrahedral mesh obtained from Pro/Mesh.

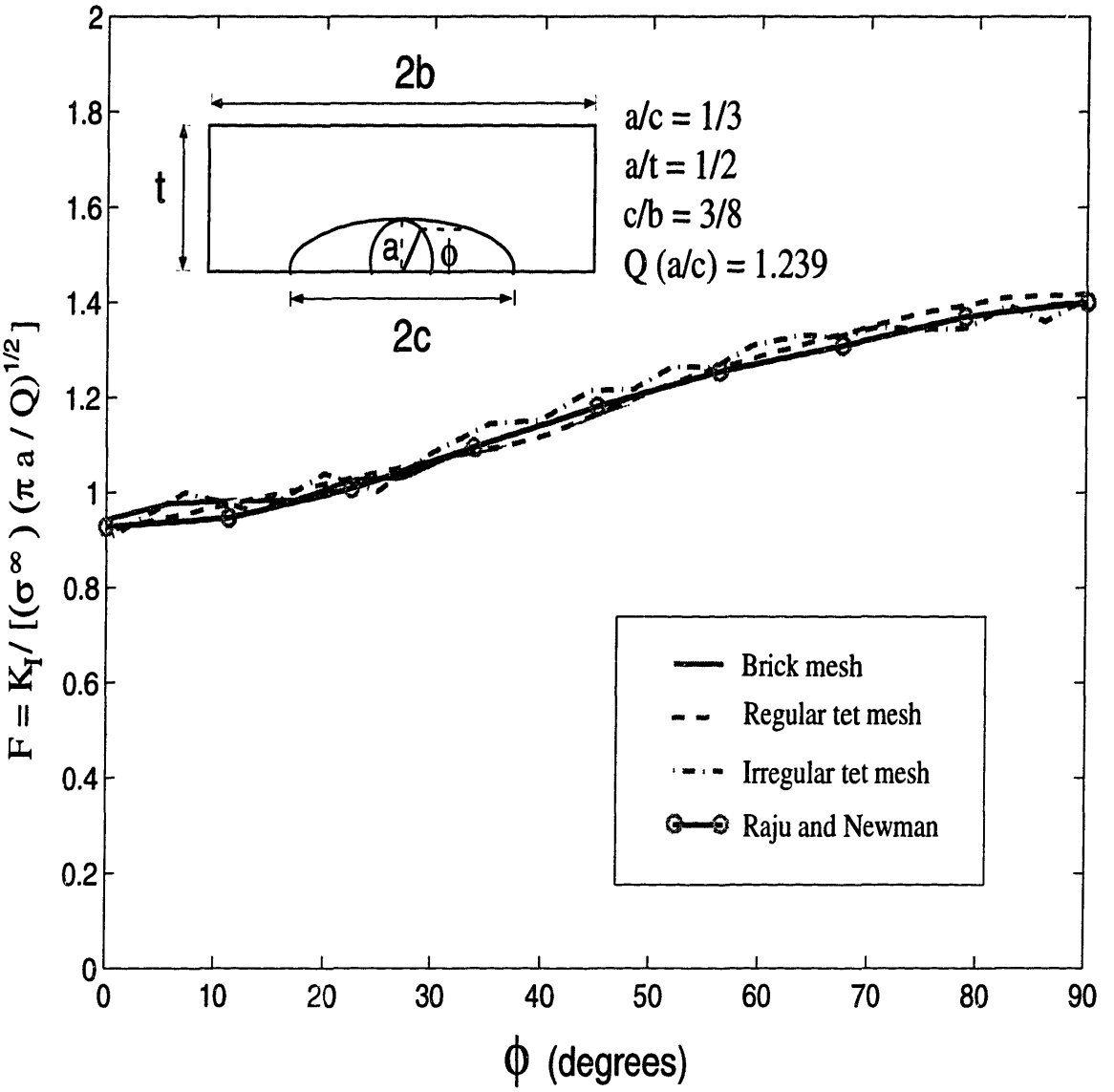

Figure 6-7: Point-wise J-integral values for semi-elliptical surface crack in a finite thickness plate. The semi-elliptical crack is subjected to uniform remote tension of magnitude σ^{∞}.

Chapter 7

Elastic-plastic analysis

7.1 Elastic-plastic fracture mechanics

In the previous section we were in the regime of linear elastic fracture mechanics (LEFM). Linear elastic fracture mechanics is valid as long as the non-linear material deformation is confined to a small region (relative to the in-plane dimensions) surrounding the crack-tip. Elastic-plastic fracture mechanics (EPFM) is to be used under circumstances depending on geometry, loads and material which exhibit substantial plastic deformation. Two parameters: J and crack tip opening displacement (CTOD) are commonly used as a fracture criterion. The J-integral has been widely accepted as a fracture characterizing parameter for non-linear materials, and its applicability to elastic-plastic crack configurations is detailed below.

7.1.1 Nonlinear fracture mechanics

Consider the uniaxial stress-strain behavior of elastic-plastic and nonlinear elastic materials. The loading behavior of the two materials is identical, but the materials' responses differ when each is unloaded. While the elastic-plastic material follows a linear unloading path with slope equal to the Young's modulus, the nonlinear elastic material unloads along the same path as it was loaded. There is a unique stress-strain relation for an elastic material, whereas in an elastic-plastic material, a given

strain can correspond to more than one stress level when the material is unloaded or cyclically loaded. Hence it is much easier to analyze an elastic material. As long as there is monotonic loading, the mechanical responses of both the materials are the same. In three-dimensions, even though it does not necessarily follow that the loading behaviors of nonlinear elastic and elastic-plastic material are identical, it is a very good approximation, as detailed later in the next subsection. Many monotonic loading problems in plasticity can be dealt with by treating the material as non-linear elastic through the deformation theory of plasticity (*i.e.*, nonlinear elasticity) [7].

Hutchinson [23] and Rice and Rosengren [24] independently showed that J characterizes crack-tip conditions in a nonlinear material. Hutchinson had used a Ramberg-Osgood power law hardening material of the form

$$\frac{\epsilon}{\epsilon_0} = \frac{\sigma}{\sigma_0} + \alpha(\frac{\sigma}{\sigma_0})^n, \tag{7.1}$$

where ϵ_0 is a reference strain, σ_0 is a reference stress $\sigma_0 = (E\epsilon_0)$, α is a material constant and n the strain hardening exponent. Rice and Rosengren had used a power law hardening of the form

$$\frac{\epsilon}{\epsilon_0} = \begin{cases} \frac{\sigma}{\sigma_0} & \text{if} < 1\ , \\ (\frac{\sigma}{\sigma_0})^n & \text{if} > 1\ . \end{cases} \tag{7.2}$$

Both of them independently showed that in order for J to remain path-independent, $\sigma \cdot \epsilon$ must vary as $1/r$ near the crack-tip. Also, at distances very near to the crack-tip the elastic strains are small in comparison to the total strain, and the stress-strain behavior reduces to a simple power law. The asymptotic stresses and strains ahead of the crack-tip, as $r \to 0$, were obtained by Hutchinson [23] from the solution of the nonlinear eigen value problem as

$$\sigma_{ij} = \sigma_0(\frac{EJ}{\alpha\sigma_0^2 I_n r})^{\frac{1}{n+1}}\ \tilde{\sigma}_{ij}(n,\theta) \tag{7.3}$$

and

$$\epsilon_{ij} = \frac{\alpha\sigma_0}{E}\left(\frac{EJ}{\alpha\sigma_0^2 I_n r}\right)^{\frac{n}{n+1}} \tilde{\epsilon}_{ij}(n,\theta) \ , \tag{7.4}$$

where I_n is an integration constant that depends on n, and $\tilde{\sigma}_{ij}$ and $\tilde{\epsilon}_{ij}$ are dimensionless functions of n and θ. These parameters also depend on the stress state (*i.e.*, plane stress or plane strain). The above equations are called the HRR singularity fields. A detailed discussion on the HRR fields is in [5].

7.1.2 Plasticity theories in elastic-plastic fracture mechanics

The deformation theory of plasticity was proposed by Hencky in 1924. In this theory the plastic strain tensor itself is assumed to be determined by the stress tensor, provided the yield condition is met. The deformation theory is a total strain theory, and since the strains depend only on the final stress, the strain state is independent of any particular loading path. In general, however, the deformation theory cannot be used for problems in which unloading occurs, for the obvious reason that unloading in a real material follows a different stress-strain curve. A more detailed discussion on the deformation theory is in [25]. For the uniaxial deformation of a Ramberg-Osgood material with a stress strain relation as given by (7.1), we have the plastic strain ϵ^p as

$$\epsilon^p = \alpha\left(\frac{\sigma}{\sigma_0}\right)^{n-1} \frac{\sigma}{E}. \tag{7.5}$$

Differentiating (7.5), we get the increment of plastic strain as

$$d\epsilon^p = \alpha n\left(\frac{\sigma}{\sigma_0}\right)^{n-2} \frac{\sigma}{E} \frac{d\sigma}{\sigma_0}. \tag{7.6}$$

The incremental theory of plasticity is widely used in mechanics, and in this theory the increment of the total strain, $d\epsilon$, is written in terms of its elastic and plastic parts as $d\epsilon = d\epsilon^e + d\epsilon^p$, where $d\epsilon^e \equiv d\sigma/E$. Now for the uniaxial case, (7.6) is also the expression for $d\epsilon^p$ from the incremental theory. Hence there is no difference between the theories for monotonic loading in the uniaxial case. Equation (7.5) can be generalized to three dimensions by assuming deformation plasticity and isotropic

hardening:

$$\epsilon_{ij}^{p} = \frac{3}{2}\alpha(\frac{\sigma_e}{\sigma_0})^{n-1}\ \frac{S_{ij}}{E}, \tag{7.7}$$

where $\sigma_e = (3S_{ij}S_{ij}/2)^{1/2}$ is the effective (von Mises) stress, and S_{ij} is the deviatoric component of the stress tensor, defined as

$$S_{ij} = \sigma_{ij} - \frac{1}{3}\sigma_{kk}\delta_{ij}, \tag{7.8}$$

where δ_{ij} is the Kronecker delta. Equation (7.7) is the deformation theory flow rule for a Ramberg-Osgood material. The flow rule for incremental theory is given by

$$d\epsilon_{ij}^{p} = \frac{3}{2}\alpha n(\frac{\sigma_e}{\sigma_0})^{n-2}\ \frac{S_{ij}}{E}\frac{d\sigma_e}{\sigma_0}. \tag{7.9}$$

The two theories of plasticity coincide only if (7.9) can be integrated to obtain (7.7). This happens when there is proportional loading in the deviatoric stresses [1]. Budiansky has shown that the deformation theory is still acceptable when there are modest deviations from proportionality [26]. Further discussion on these theories of plasticity can be found in [5]. In conclusion we can say that the deformation theory and the incremental theory are equivalent in most cases for purpose of elastic-plastic fracture mechanics computation (with stationary crack fronts).

7.2 Elastic-plastic formulation of the domain integral method

The J-integral is an energy-related quantity as described in section 2.1. It has also been shown earlier (see section 2.1) that for a virtual crack extension δl as shown in figure 2-1, the J-integral around the crack tip is the change in potential energy (per unit thickness) $\tilde{\pi}$:

$$J = -\frac{\partial\tilde{\pi}}{\partial l}, \tag{7.10}$$

[1] The total stress components need not be proportional for the two theories to coincide, as the flow rule does not depend on the hydrostatic part of the stress tensor.

under conditions of the equivalence between $\mathcal{G}$ and J described in section 2.1. Equation (7.10) is also valid for a non-linear elastic material. Recall the definition of J from (2.1)

$$J = \int_{\Gamma} [W\alpha_1 - \sigma_{ij}\alpha_j \frac{\partial u_i}{\partial x_1}] d\gamma, \tag{7.11}$$

where W, the strain energy density, is defined as

$$W(\epsilon_{kl}) = \int_0^{\epsilon_{kl}} \sigma_{ij} d\epsilon_{ij}. \tag{7.12}$$

We also have the Cauchy stress σ_{ij} as

$$\sigma_{ij} = \frac{\partial W}{\partial \epsilon_{ij}} . \tag{7.13}$$

In the context of incremental theory, in (7.12), the integral is taken along the actual path of loading and (7.13) becomes a formal definition of "$\partial W/\partial \epsilon_{ij}$" as "$\sigma_{ij}$". We can now rewrite (7.12) as

$$W(\epsilon_{kl}) = \int_0^{\epsilon_{kl}} \sigma_{ij} (d\epsilon_{ij}^e + d\epsilon_{ij}^p), \tag{7.14}$$

where $d\epsilon_{ij}^e$ and $d\epsilon_{ij}^p$ are the elastic and plastic parts of the total incremental strain, $d\epsilon_{ij}$ respectively. Equation (7.14) now becomes

$$W(\epsilon_{kl}) = W^e + W^p, \tag{7.15}$$

where W^e is the elastic strain energy and W^p is the plastic dissipation. Hence we obtain the volume integral expression for the energy release for the elastic-plastic case from (2.17) as

$$-\delta\pi = \int_{\Omega} [(W^e + W^p)\delta_{kj} - \sigma_{mj} \frac{\partial u_m}{\partial x_k}] \frac{\partial q_k}{\partial x_j} dV. \tag{7.16}$$

7.3 Finite element implementation of the domain integral method

To compute the J-values along the crack front, we use the finite element implementation of the domain integral method exactly as described in section 2.3. The crack-front integral expression remains the same as (2.25) in subsection 2.3.1 and is evaluated using the proposed crack-front perturbation pattern described in subsection 4.1.1. The volume integral expression for the energy release is now evaluated using (7.16). The evaluation of (7.16) is similar in all respects to FE evaluation of (2.19) using the proposed method as described in subsections 2.3.2 and 4.1.2, except that now both W^e and W^p have to be read at the integration points of the 3-D elements in the domain Ω. The point-wise J values are obtained using the procedure detailed in subsection 2.3.3.

7.4 Edge-cracked model in plane strain

7.4.1 Description of the model

A straight through-thickness crack is considered in a body with characteristic dimensional ratios $(a/B) = 0.5$, $(h/B) = 3.0$, and $(a/w) = 0.5$, as shown in figure 7-1. The model is constrained to plane strain boundary conditions. Begley and Landes [27] have shown that J can be evaluated experimentally using tensile loading of a cracked specimen. The aims of this exercise are to study the accuracy of the method proposed in chapter 4 in obtaining J-values under fully-plastic conditions and the effect of material model and plasticity theories in obtaining accurate fully-plastic J values. The analysis is performed on two material models – an elastic/perfectly-plastic material model using the incremental theory of plasticity and a Ramberg-Osgood hardening behavior using deformation theory. The elastic/perfectly-plastic model is loaded with a far-field uniform relative displacement Δ, and the Ramberg-Osgood model is loaded with a uniform far-field tensile stress σ^∞. The elastic/perfectly-plastic material model

is considered, so that the results can be conveniently compared to the rigid-plastic theoretical predictions [28], as detailed below.

7.4.2 Finite element modeling

As in the elastic case, ABAQUS/Pre [14] and Pro/MESH [15] were used to create the regular and irregular tetrahedral meshes respectively, and ABAQUS/Standard [17] was used as the FE solver. One-half of the specimen geometry was modeled, and second-order isoparametric (10-noded) tetrahedral elements were used to mesh this geometry with quarter-point elements [16] at the crack tip. The tetrahedral mesh results were also compared to predictions obtained using brick meshes of comparable mesh density with the quarter-point elements at the crack tip, using the domain integral option in ABAQUS/Standard. A finer mesh is used near the crack to capture the steep crack-tip gradients. The crack plane view of the tetrahedral meshes is shown in figure 7-2. The results are also compared with a 2-D plane strain analysis using 2-D 8-noded quadrilateral plane strain elements with reduced integration (CPE8R) from ABAQUS/Standard [17]. A focussed mesh is also used at the crack tip. The 2-D FE mesh is shown in figure 7-3.

7.4.3 Results and discussion

Elastic/perfectly-plastic material model

The one-half specimen is loaded with a far-field displacement of $\Delta/2$. Elastic/perfectly-plastic material model is used with $Y/E = 0.0011$, where Y is the tensile yield strength of the material and E is the Young's modulus. For a rigid-plastic model in plane strain, we have from limit analysis [29], the limit load P_{LIM} as

$$P_{LIM} = \frac{2Yw}{\sqrt{3}}(B - a), \tag{7.17}$$

where a the crack length and B, w are dimensions as shown schematically in figure 7-1. Schematic load-displacement curves for crack lengths of a and $(a + \delta a)$ are shown

in figure 7-4. From the definition of J as the energy difference, we have

$$J \cdot (\delta a) = \int_0^{\Delta} -(\frac{\partial P}{\partial a})\ (\delta a)\ d\delta, \tag{7.18}$$

where $P(\delta; a)$ is the load at displacement δ and crack length a. For a rigid-plastic formulation, we can write (7.18) as

$$J = J_{Plastic} = \Delta \cdot (-\frac{\partial P_{LIM}}{w\ \partial a}), \tag{7.19}$$

and hence from (7.17)

$$\frac{dJ_{Plastic}}{d\Delta} = -\frac{\partial P_{LIM}}{w\ \partial a} = \frac{2Y}{\sqrt{3}}. \tag{7.20}$$

Hence the slope of the J-Δ curve is constant in the fully-plastic, non-hardening regime, which can be used to verify the FE results.

Figure 7-5 shows the plot of normalized load P/P_{LIM} versus the normalized far-field displacement $(10^3 \cdot \Delta/2h)$. We can observe from figure 7-5 that the finite element solutions overshoot the limit load of (7.17). This can be attributed to the fact that the classical solution to the plane strain problem is the sliding off along two 45^o slip planes. The FE solutions for elastic-plastic materials exhibit too stiff a response in the fully plastic range. Nagtegaal, *et al.* have studied the accuracy of finite element solutions in the fully plastic range. They observed that a cause of this problem is that the deformation state of an elastic perfectly-plastic material is highly constrained at limit load, and, for the usual material idealization, deformation increments at limit load will be strictly incompressible [30].

The values of J obtained are normalized using EJ/Y^2a, and the far-field displacement Δ is normalized to $E\Delta/Yl$, where E is the Young's modulus, Y the yield strength and $l = (B - a)$ is the ligament length as shown in figure 7-1. The J-profile along the crack-front is shown in figure 7-6 for three domains of integration at the last increment of loading (*i.e.*, at $E\Delta/Yl = 32$), corresponding to the fully-plastic case. The values of J are normalized by the J-value obtained from the 2-D plane strain solution at the same load-level (*i.e.*, at $E\Delta/Yl = 32$). We observe some path

dependence of the computed J-values along the crack-front for the domain close to the crack tip (*i.e.*, $\rho/a = 0.4$, $\rho/a = 0.5$ and $\rho/a = 0.6$). This is because of the basic nature of the incremental theory of plasticity as detailed in earlier sections. Also, the general trend of the modest path-dependence is consistent with reported results: J monotonically increases with distance from the crack-tip to a far-field saturation value. In our further analysis, for the 3-D meshes, we consider the average value of J along the crack-front, $\bar{J} = \int J dx/w$, to represent the J for a load-level. To validate the elastic-plastic analysis, we consider the slope of the normalized J-Δ curve from (7.20) under fully plastic conditions. We now have the slope of the normalized J-Δ curve (under fully plastic conditions), denoted $(Slope)_{th}$ as

$$\frac{d(EJ/Y^2a)}{d(E\Delta/Yl)} = (Slope)_{th} = \frac{2\,l}{\sqrt{3}\,a}. \tag{7.21}$$

Figure 7-7 shows the plot of normalized J ($\bar{J}$ for the 3-D meshes) versus normalized Δ. Calculating the slope of the curves from the FE computations from figure 7-7, we have $(Slope)_{Reg.tet.} = 1.131$, $(Slope)_{Irr.tet.} = 1.120$ and $(Slope)_{Bricks} = 1.134$. We also have, for the geometry modeled, $(Slope)_{th} = 1.155$. Thus the slope of $J - \Delta$ curve has a variation of 3 % from the theoretical value for the irregular tetrahedral mesh and 2 % for the regular tetrahedral mesh.

Ramberg-Osgood material model

The straight through-thickness crack in plane strain is also analyzed using the Ramberg-Osgood law with $n = 5$ and $\alpha = 0.5$. The one-half model is loaded with a uniform far-field tensile stress σ^{∞}. The Electric Power Research Institute (EPRI) J-estimation scheme [31] provides a means for computing the J integral for a hardening behavior represented by the Ramberg-Osgood material model. The total J is given by sum of the plastic and the effective elastic J; *i.e.*, $J_{tot} = J_{el} + J_{pl}$.

The fully-plastic J-integral in the EPRI J-estimation scheme, for the geometry

and loading considered, is expressed as

$$J_{pl} = \alpha\epsilon_0\sigma_0 \left(\frac{la}{B}\right) h_1 \left(\frac{P}{P_0}\right)^{n+1}, \tag{7.22}$$

where $l = (B-a)$ is the ligament length and a is the crack length, as shown in figure 7-1. The dimensionless factor $h_1(a/B, n)$ is tabulated in [31] for various configurations. In our case, $h_1 = 0.928$, for $n = 5$ and $a/B = 0.5$. In (7.22), P is the tensile load and is computed as $\sigma^{\infty} \cdot Bw$. The reference load P_0 is given by

$$P_0 = 1.455\eta w l \sigma_0, \tag{7.23}$$

where

$$\eta = \sqrt{1 + (a/l)^2} - (a/l). \tag{7.24}$$

For the geometry under consideration, with $a/l = 1$, $\eta = 0.414$.

The effective elastic J is computed from

$$J_{el} = \frac{K_I^2}{E'}, \tag{7.25}$$

where $E' = E/(1-\nu^2)$ for plane strain, and K_I is a function of the effective crack length (a_{eff}) which is given by

$$a_{eff} = a + \frac{1}{1 + (P/P_0)^2} \frac{1}{\beta\pi} \left(\frac{n-1}{n+1}\right) \left(\frac{K_I(a)}{\sigma_0}\right)^2, \tag{7.26}$$

where $K_I(a)$ implies that K_I is a function of the crack length a, and $\beta = 6$ for plane strain conditions. The values of K_I can be obtained from

$$K_I = \frac{P}{w\sqrt{B}} f(a/B), \tag{7.27}$$

where $f(a/B)$ is a function of the geometry of the crack that is tabulated in [5].

The same FE meshes as in the elastic/perfectly-plastic case are used, and the J-profile along the crack-front is shown in figure 7-8 for three domains of integration

at the last increment of loading (*i.e.*, at $\sigma^{\infty}/\sigma_0 = 1.36$), corresponding to the fully-plastic case. The values of J are normalized by the J obtained from the EPRI reference solution at the same load-level (*i.e.*, at $\sigma^{\infty}/\sigma_0 = 1.36$). Three domains (*i.e.*, $\rho/a = 0.4$, $\rho/a = 0.5$ and $\rho/a = 0.6$) are considered, and they exhibit path independence. In our further analysis, we consider the average value of J along the crack-front, $\bar{J} = \int J dx/w$, to represent J for the 3-D meshes at a given load-level. Figure 7-9 shows the variation of normalized J ($\bar{J}$ for the 3-D meshes) versus normalized load level, σ^{∞}/σ_0, for both the tetrahedral meshes along with bricks and the 2-D plane strain result. The EPRI solution is also shown in the figure. We can observe from figure 7-9 that the variation in the computed J-values for the tetrahedral elements is less than 2-3% of the EPRI reference solution.

7.5 Surface cracks in a semi-infinite body

The predictions of fracture strengths and fatigue lifetimes of components require accurate solutions of singularity strengths (J, K, etc.) for small surface cracks. For these cracks, crack geometry and material non-linearity must be considered along with the three-dimensional nature of the surface crack. These studies often involve material behavior in the elastic-plastic regime. Trantina, *et al.* [32] have done 3-D elastic-plastic FE studies on surface cracks for two geometries; namely, semi-circular and semi-elliptical surface cracks. These studies were done using brick elements and the deformation theory of plasticity, and J-profiles along the crack-front were computed using the virtual crack extension method.

We have analyzed similar crack geometries using our J calculation procedure and have done elastic-plastic analysis on two crack geometries: semi-circular and semi-elliptical surface cracks in a semi-infinite body. The analysis was performed for all the three FE meshes as before: a regular tetrahedral one from ABAQUS/Pre [14], an irregular one from Pro/MESH [15] and a brick mesh from ABAQUS/Pre [14]. Quarter-point elements were also used at the crack-tip [16] along with a finer mesh at the crack-tip. The Ramberg-Osgood deformation plasticity material model was

considered for the analysis using the in-built material model in ABAQUS/Standard [17]. The analysis was performed for $n = 10$ and $\alpha = 0.25$.

7.5.1 Semi-circular surface crack

A semi-circular surface crack has been considered, as shown in figure 7-14. The radius of the half cylinder which represents the infinite body is $10a$, where a is the crack depth. Hence we can be assured that there is a uniform stress field in the model except near the crack tip, and that the crack is unaffected by the boundaries. The model is loaded to a far-field relative displacement of Δ. One-fourth the specimen geometry is modeled, with $a/L = 1/20$. The irregular tetrahedral mesh from Pro/MESH and the brick mesh ABAQUS/Pre for the specimen geometry are shown in figure 7-10. Close-up views of displaced meshes of the the crack tip region are shown in figure 7-11. The model was loaded to a nominal strain $\epsilon = \Delta/L = (6 - 7) \times \epsilon_0$, so that we are near the fully plastic regime. A lower bound for the limit load can be computed as $P_{LB} = \sigma_0 \pi (100a^2 - a^2)$ from [29]. The variation of load P, normalized with P_{LB}, versus the nominal strain $\epsilon = \Delta/L$ is shown in figure 7-12. We can observe from figure 7-12 that we are well into the plastic regime. Figure 7-13 shows the variation of J at the symmetry plane (which is the $\phi = 90^o$ plane) with the normalized far-field displacement for all the FE meshes. The values of J are normalized using using $\sigma_0^2 a/E$. The plot on figure 7-13 has a parabolic variation at low nominal strains, corresponding to the dominance of the elastic J. Trantina, *et al.*, have reported values for only nominal strains up to $1.35\epsilon_0$. The results of the analyses for all three FE meshes at a nominal strain $\epsilon = 1.35\epsilon_0$, along with the values reported by Trantina, *et al.*, are shown in figure 7-14. The values of $J(\phi)$ are normalized with $J_{\phi=90^o}$. The 90^o plane corresponds to the symmetry plane, as shown in figure 7-14. The variation along the crack-front of $J(\phi)/J_{\phi=90^o}$, at different load levels, is shown in figure 7-15. Three load levels at nominal strains $\epsilon = 0.34\epsilon_0$, corresponding to an elastic state; $\epsilon = 1.20\epsilon_0$, representing yield and elastic-plastic behavior; and $\epsilon = 6.82\epsilon_0$, corresponding to a fully-plastic state, are considered. In the elastic region, J at the surface is 30 % greater than J at the center. This is in agreement with the results

reported by Trantina, *et al.* [32]. With increasing strain, J at the surface decreases (to about 90 % of the J at the center at $\epsilon = 1.20\epsilon_0$), and there is peak which develops at $\phi = 15 - 20^o$. This unique variation of J along the crack front is due to a combination of increased J due to plasticity and the loss of plane strain constraint at the free surface. Further discussion on the plane strain constraint can be found in [32]. In the fully-plastic case, J at the surface is smaller than J at the center by 25%.

7.5.2 Semi-elliptical surface crack

A semi-elliptical surface crack of aspect ratio $a/c = 0.7$ is considered next, as shown in figure 7-20. The radius of the half-cylinder which represents the infinite body is again $10a$, where a is the crack depth. The model is loaded to a far-field displacement of Δ, and one-fourth the specimen geometry is modeled, with $a/L = 1/20$. For the semi-elliptical surface crack, the irregular tetrahedral mesh from Pro/MESH and the brick mesh from ABAQUS/Pre are shown in figure 7-16. Figure 7-17 shows close-up views of the displaced meshes near the crack tip region. The model is again loaded to a nominal strain $\epsilon = \Delta/L = (6 - 7) \times \epsilon_0$. A lower bound for the limit load in this case can be computed as $P_{LB} = \sigma_0\pi(100a^2 - ac)$ from [29]. The variation of load P, normalized with P_{LB}, versus the nominal strain $\epsilon = \Delta/L$ is shown in figure 7-18. Figure 7-19 shows that variation of J at the symmetry plane (which is the 90^o plane) with the normalized far-field displacement for all the FE meshes. The values of J are normalized by $\sigma_0^2 a/E$. Again we observe the parabolic variation at low nominal strains from the plot on figure 7-19 due to the dominance of the elastic J. For $\epsilon/\epsilon_0 = 1.35$, figure 7-20 shows the variation along the crack-front of J, normalized with $J_{\phi=90^o}$ for all the three FE meshes, along with the values reported by Trantina, *et al.* [32]. The 90^o plane again corresponds to the symmetry plane, as shown in figure 7-20. The crack-front variation of J, normalized by J at the symmetry plane, is shown in figure 7-21 for different load levels. Three load levels at nominal strains $\epsilon = 0.34\epsilon_0$, $\epsilon = 1.20\epsilon_0$ and $\epsilon = 6.82\epsilon_0$ are again considered, as in the semi-circular case. From figure 7-21 we see J at the surface is 10 % smaller than J at the center at low nominal strains, and that there is a local minimum at around $15 - 20^o$. This is

again in agreement with the results reported by Trantina, *et al.* [32]. J at the surface decreases to about 30 % less than J at the center for $\epsilon = 1.20\epsilon_0$. The J-variation along the semi-elliptical crack-front, in the elastic-plastic regime has an increasing profile, unlike the corresponding elastic-plastic J-distribution for the semi-circular case. In the fully-plastic case (at $\epsilon = 6.82\epsilon_0$), J at the surface is smaller than the J at the center by 50 %, and again J increases monotonically as the crack-front is traversed from the surface to the center.

7.6 Semi-elliptical surface crack in a finite thickness plate

A semi-elliptical surface crack in a finite thickness plate is considered. Full three-dimensional elastic-plastic analysis of semi-elliptical surface cracks under tensile loading have been done by Wang [33]. Similar crack geometry has been considered here. The geometry of the plate with a part-through surface crack is shown in figure 7-22. A semi-elliptical crack with a maximum penetration a and a total surface length of $2c$ is in the middle of the plate. The plate has a thickness of t, total width $2b$ and total height $2h$. The dimensional ratios of the crack and plate are given by $a/c = 0.24$, $a/t = 0.6$, $b/t = 8$ and $h/t = 16$. These ratios are same as the crack geometry analyzed by Wang [33]. The model was loaded by a far-field uniform relative displacement Δ. One-fourth of the specimen geometry is modeled, and the brick, regular tetrahedral and irregular tetrahedral finite element meshes of the one-fourth model are shown in figure 7-23. The Poisson's ratio was set to 0.3, and the Ramberg-Osgood material model was used with $\alpha = 1$. Two general cases, high strain hardening ($n = 5$) and moderately low strain hardening ($n = 10$) were analyzed. The variation of far-field stress σ^∞ normalized by σ_0, versus far-field strain ϵ^∞ normalized by ϵ_0, for $n = 5$ and $n = 10$, are shown in figures 7-24 and 7-26, respectively. The far-field strain is given by $\epsilon^\infty = \Delta/2h$, and the far-field stress is given by $\sigma^\infty = P/bt$, where P is the total nodal reaction force acting on the half-specimen, applied at the plane enforcing

the far-field relative displacement Δ. Figure 7-25 shows the variation of J at the symmetry plane, normalized by $\sigma_0\epsilon_0 t$, versus normalized far-field stress, along with the results obtained by Wang [33], for $n = 5$. We can observe from figure 7-25 that the variation in J at the symmetry plane is less than 3% of the values reported by Wang [33]. The values of J at various load levels for high strain hardening exponent ($n = 10$) are shown in figure 7-27. Again we can see a close match with the values reported by Wang [33]. Comparisons of J values at different load levels for the two cases ($n = 5$ and $n = 10$) are shown in figure 7-28. At low stress levels, $\sigma^\infty/\sigma_0 \leq 0.5$, the curves for $n = 5$ and $n = 10$ are indistinguishable. The crack-tip fields are essentially in small-scale yielding. At intermediate stress levels, $0.5 \leq \sigma^\infty/\sigma_0 \leq 0.8$, the J values for a material with $n = 5$ is greater than that for a material with $n = 10$. At still higher levels, $\sigma^\infty/\sigma_0 \geq 0.9$, the normalized J values for a material with $n = 10$ increases faster than that for a material with $n = 5$. The cross-over occurs at a load level of $\sigma^\infty/\sigma_0 = 0.85$. These are also consistent with the observations reported by Wang [33]. The J-profile for a low stress level of $\sigma^\infty/\sigma_0 = 0.30$, normalized by J at the symmetry plane, is shown in figure 7-29 for $n = 10$. As stated before, at low load levels, the profile for $n = 5$ coincides with the one for $n = 10$. At this load-level, J at the free surface is 37% of the J at the symmetry plane. Figure 7-30 shows the J-profile for a high stress level of $\sigma^\infty/\sigma_0 = 0.975$, normalized by J at the symmetry plane, for $n = 5$ and $n = 10$. There is a slight variation in the J profiles for the two cases, but J at the free surface is essentially the same, about 20 % of the J at the symmetry plane. These profiles are also plotted along with the profiles obtained by Wang [33].

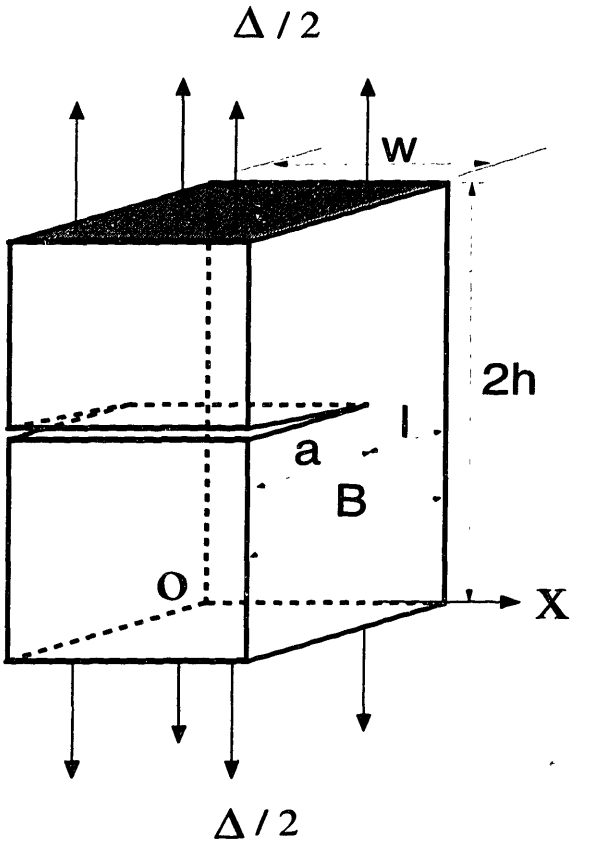

Figure 7-1: Model of the straight through-thickness crack in plane strain subjected to a uniform far-field relative displacement Δ. The dimensional ratios of the model are $(a/B) = 0.5$, $(h/B) = 3.0$ and $(a/w) = 0.5$

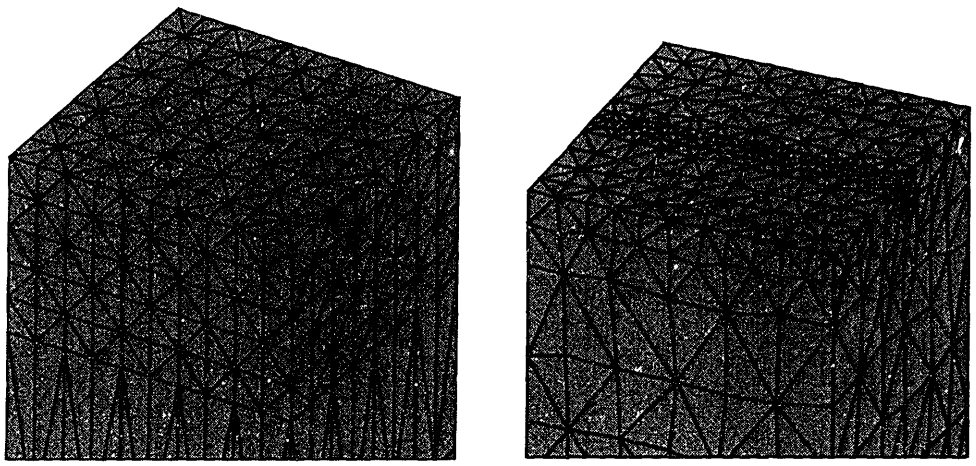

Figure 7-2: Crack plane view of the tetrahedral meshes for the straight through-thickness crack in plane strain. (a) Regular tetrahedral mesh from ABAQUS/Pre. (b) Irregular tetrahedral mesh from Pro/MESH.

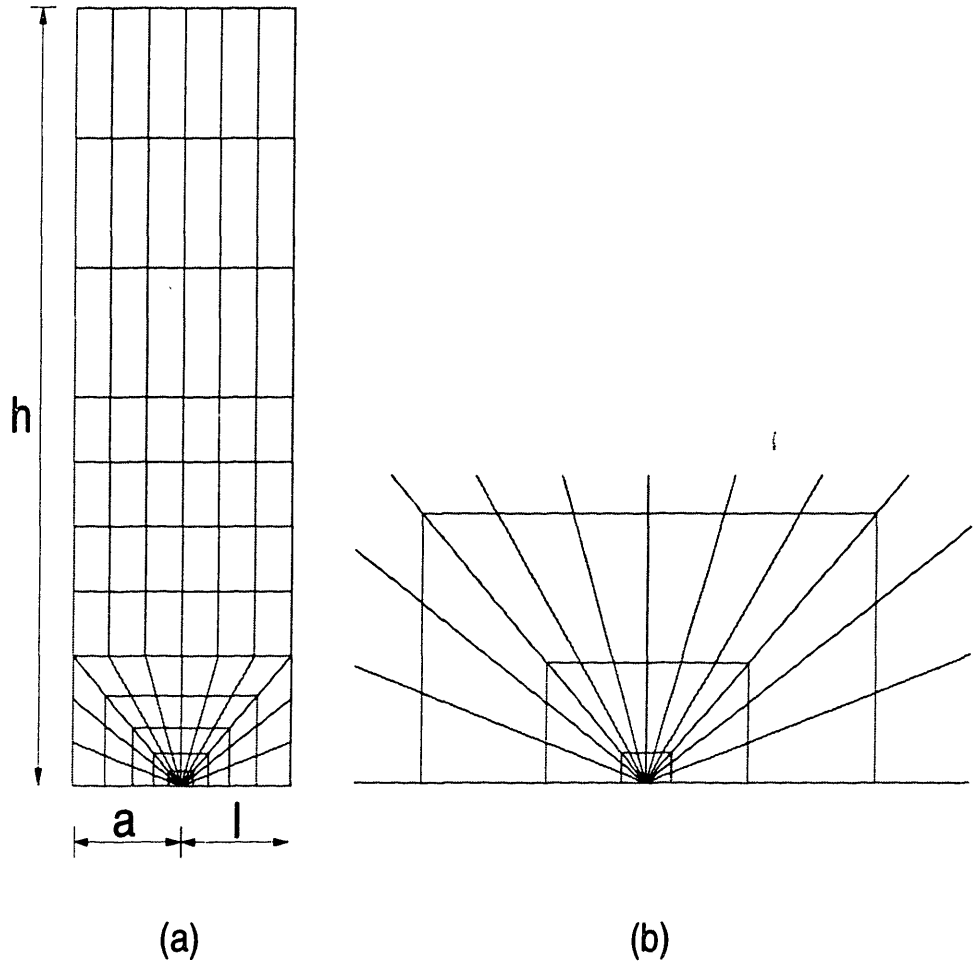

Figure 7-3: Finite element mesh for the 2-D analysis of the straight through-thickness crack in plane strain. (a) FE mesh of the entire model. (b) Detail of the crack-tip

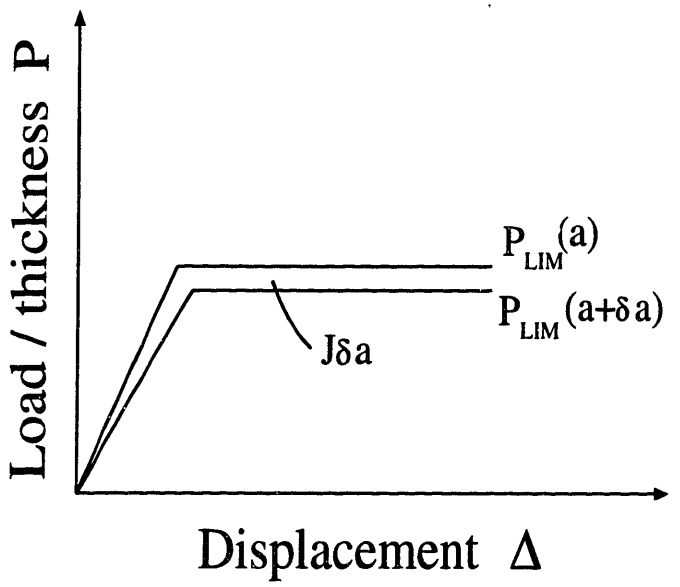

Figure 7-4: Schematic load versus displacement curve for two crack lengths, a and $(a + \delta a)$, for an elastic/perfectly-plastic material. The area under the curve is $J\delta a$. The limit load $P_{LIM}(a + \delta a) = P_{LIM}(a) + (\partial P_{LIM}/\partial a)\delta a$.

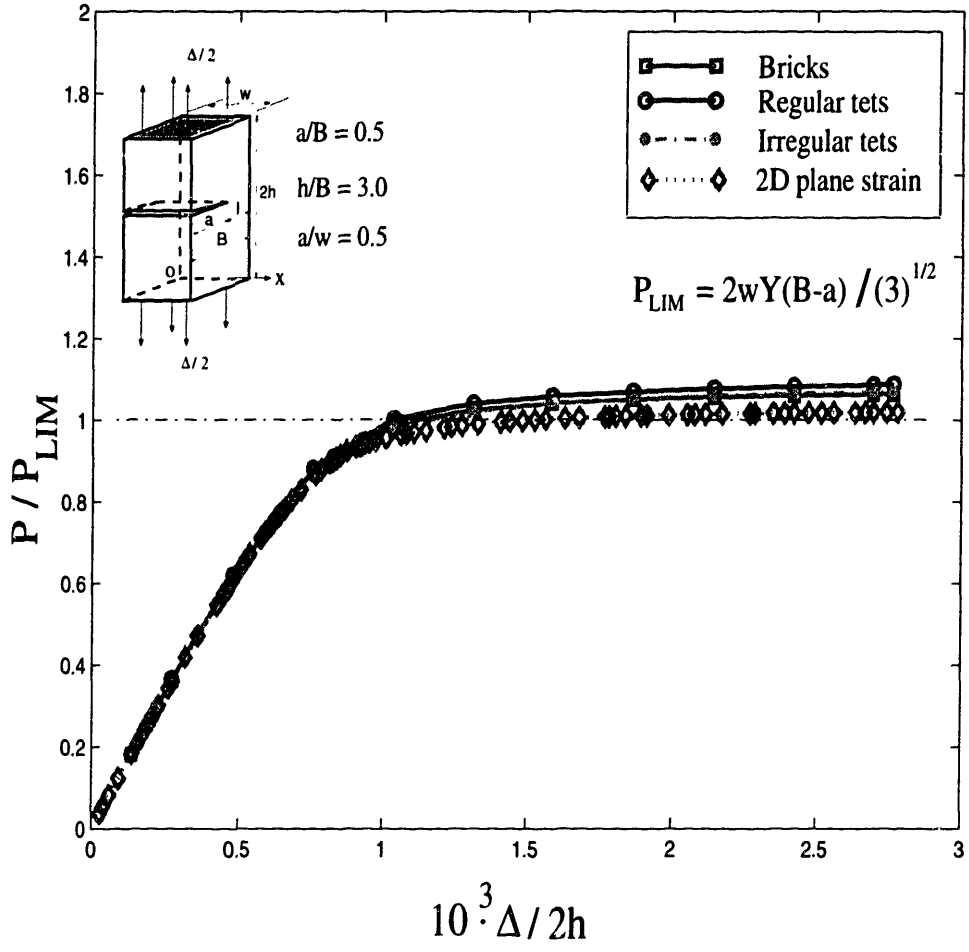

Figure 7-5: Variation of normalized load with normalized far-field displacement for the straight through-thickness crack in plane strain. Elastic/perfectly-plastic material model was used with $Y/E = 0.0011$.

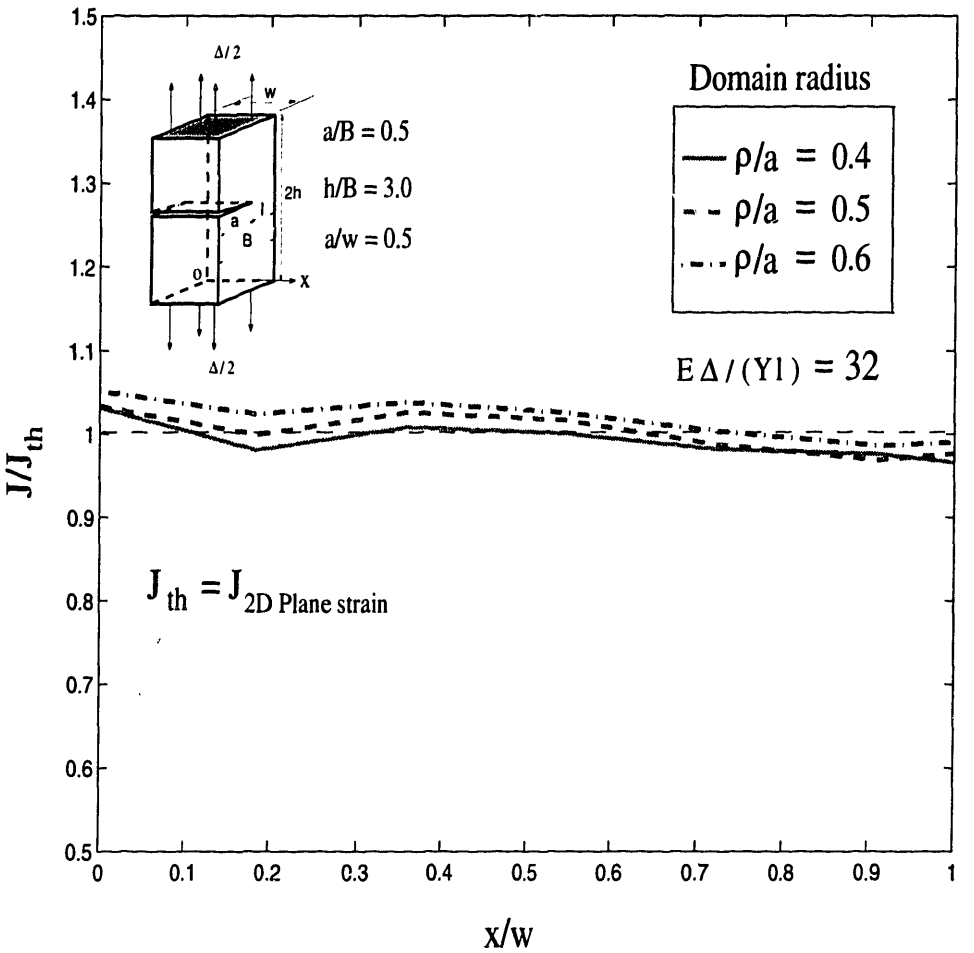

Figure 7-6: Normalized J profile along the crack-front for the straight through-thickness crack in plane strain. Elastic/perfectly-plastic material model was used with $Y/E = 0.0011$. The values of J are normalized using the J-value obtained from the 2-D plane strain solution for the load level $E\Delta/(Yl) = 32$. The values are shown for three domains of integration; $\rho/a = 0.4$, $\rho/a = 0.5$ and $\rho/a = 0.6$, for the irregular tetrahedral mesh.

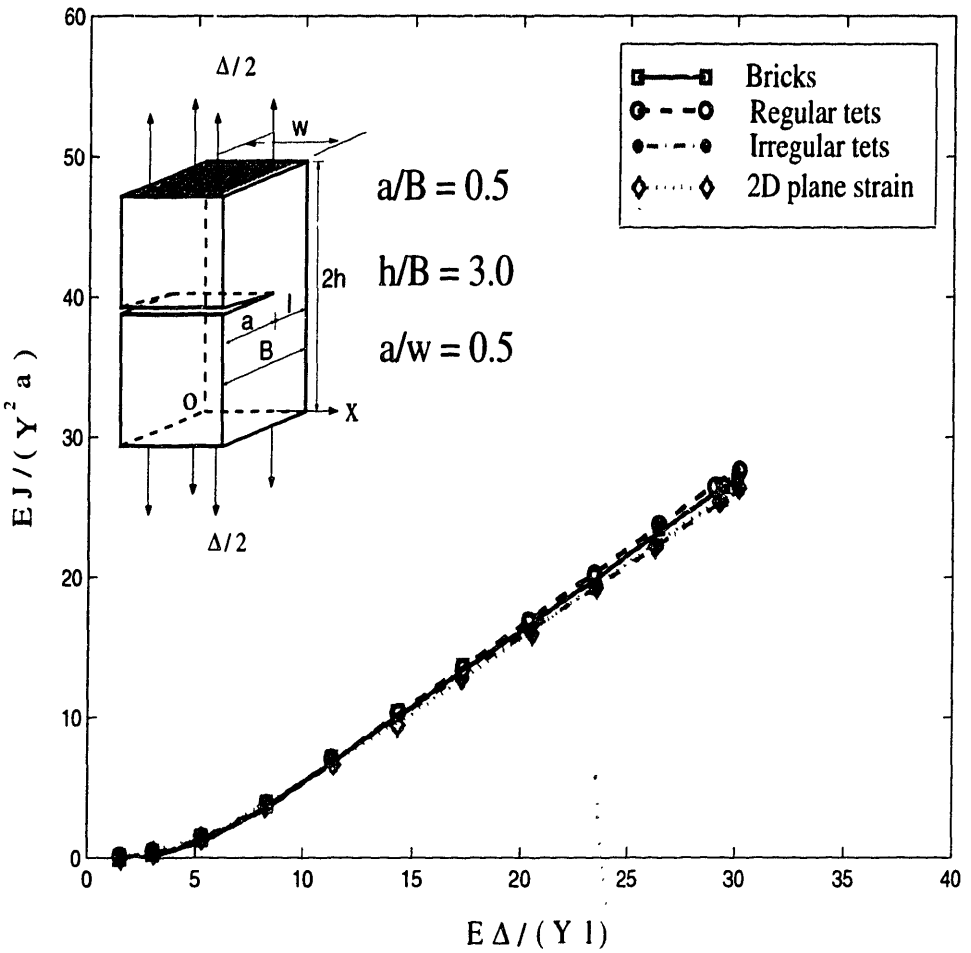

Figure 7-7: Variation of normalized J ($\bar{J}$ for the 3-D meshes) with normalized displacement for the FE meshes for the straight through-thickness crack in plane strain. Elastic/perfectly-plastic material model was used with $Y/E = 0.0011$.

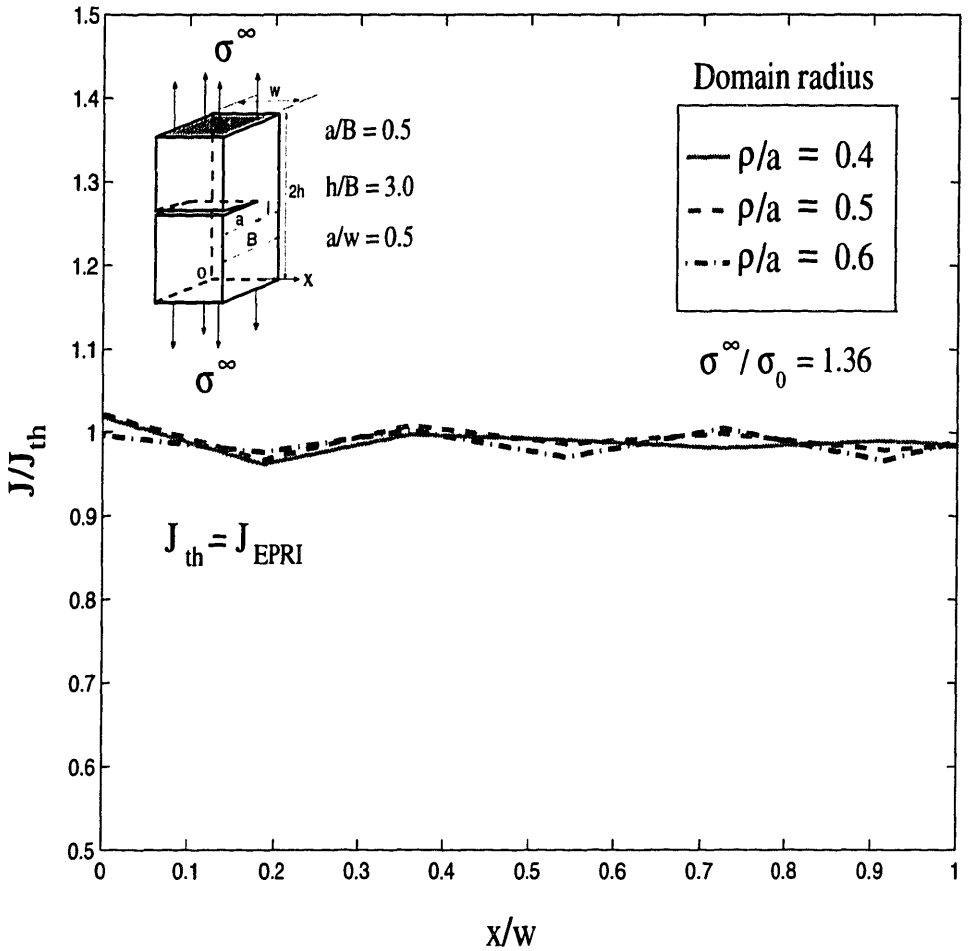

Figure 7-8: Normalized J profile along the crack-front for the straight through-thickness crack in plane strain. Ramberg-Osgood material model was used with $n = 5$ and $\alpha = 0.5$. The values of J are normalized using the J-value obtained from EPRI solution for the load level $\sigma^{\infty}/\sigma_0 = 1.36$. The values are shown for three domains of integration; $\rho/a = 0.4$, $\rho/a = 0.5$ and $\rho/a = 0.6$, for the irregular tetrahedral mesh.

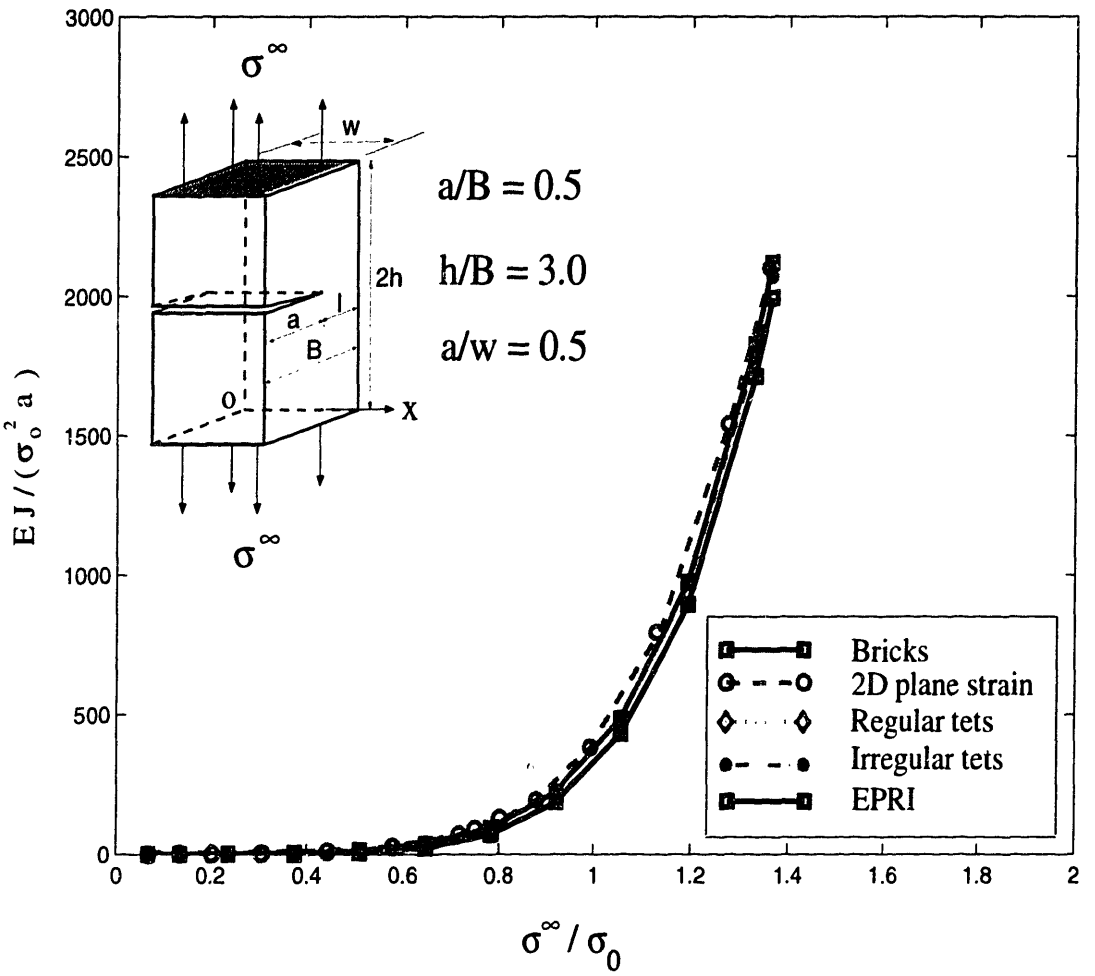

Figure 7-9: Variation of normalized J ($\bar{J}$ for the 3-D meshes) with normalized load level σ^{∞}/σ_0 from various the FE meshes for the straight through-thickness crack in plane strain. Ramberg-Osgood deformation plasticity is used with $n = 5$ and $\alpha = 0.5$.

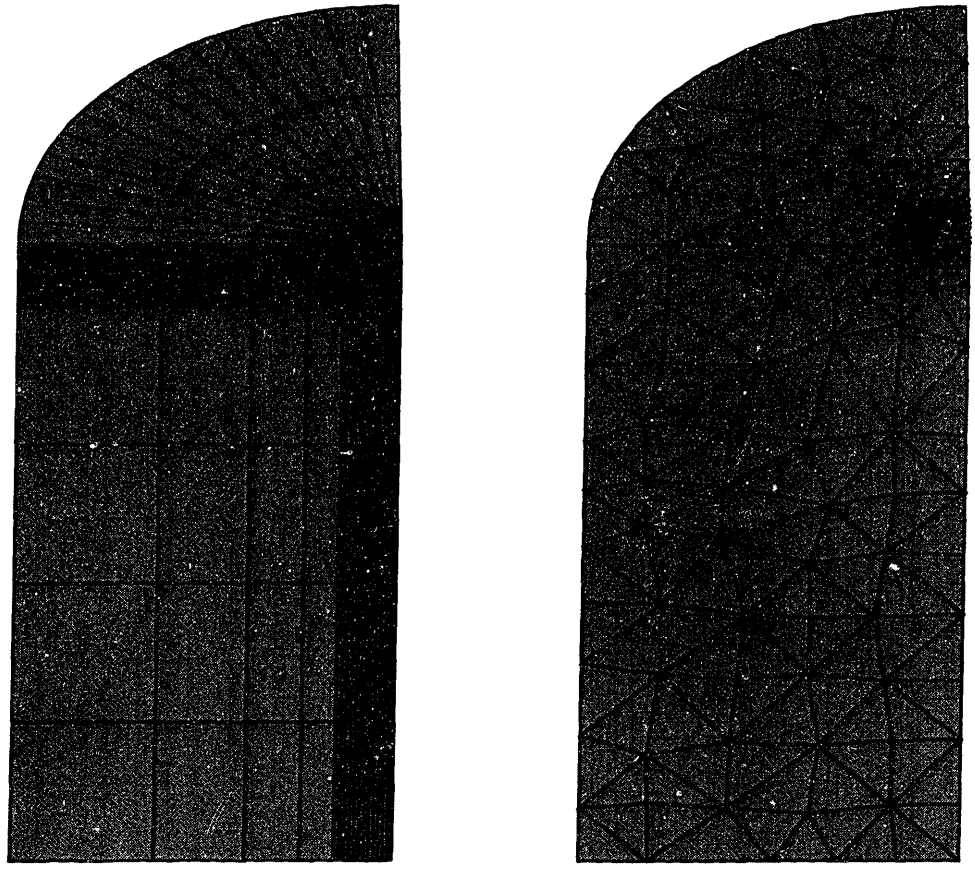

Figure 7-10: Finite element meshes for the semi-circular surface crack in a semi-infinite plate under tension. (a) Brick mesh from ABAQUS/Pre. (b) Irregular tetrahedral mesh from Pro/MESH.

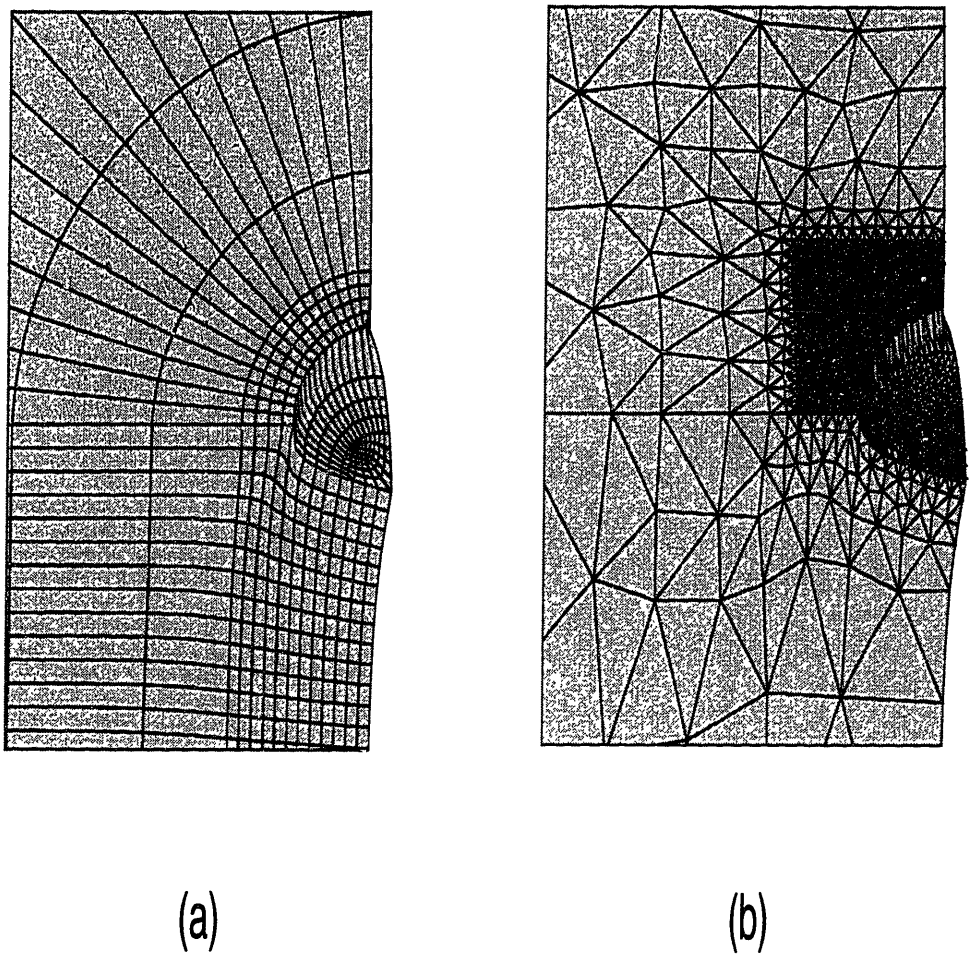

Figure 7-11: Close-up view near the crack-tip of the displaced meshes for the semi-circular surface crack . (a) Brick mesh from ABAQUS/Pre. (b) Irregular tetrahedral mesh from Pro/MESH.

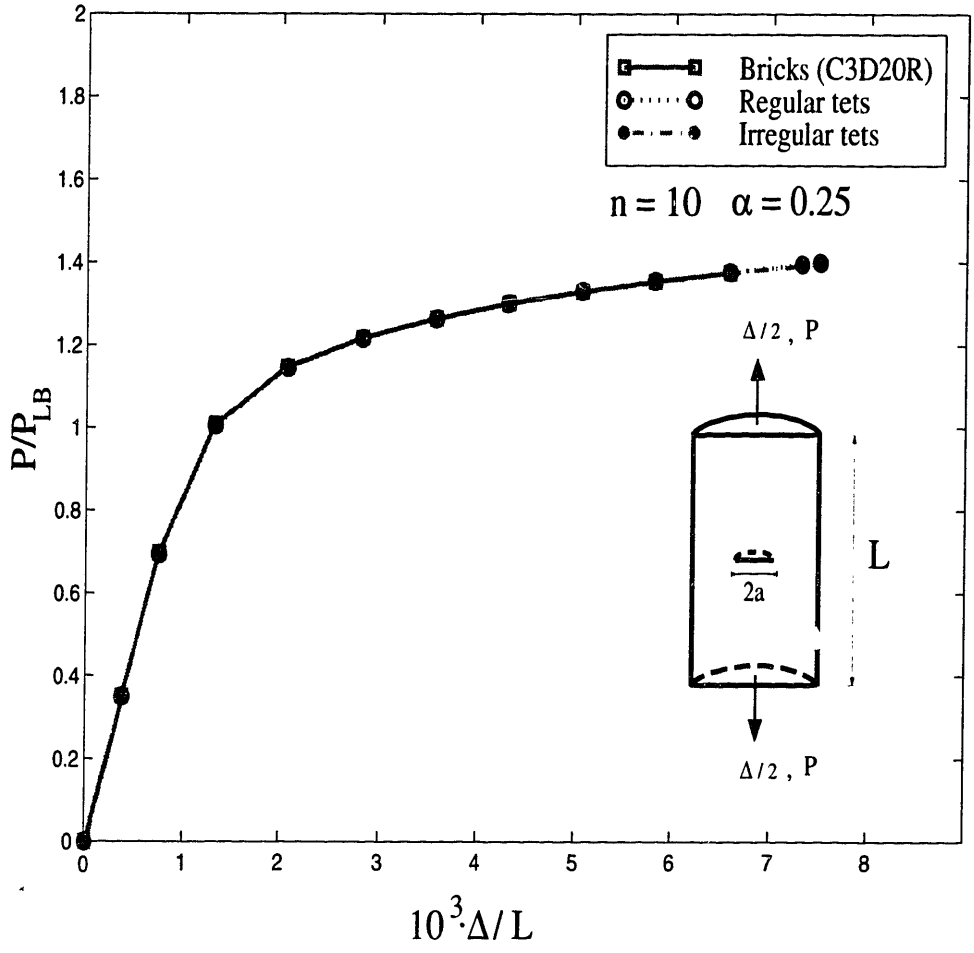

Figure 7-12: Variation of load P, normalized with $P_{LB} = \sigma_0 \pi(100a^2 - a^2)$, versus normalized far-field displacement $10^3 \cdot \Delta/L$ for the semi-circular surface crack in a semi-infinite plate. Ramberg-Osgood deformation plasticity is used with $n = 10$ and $\alpha = 0.25$.

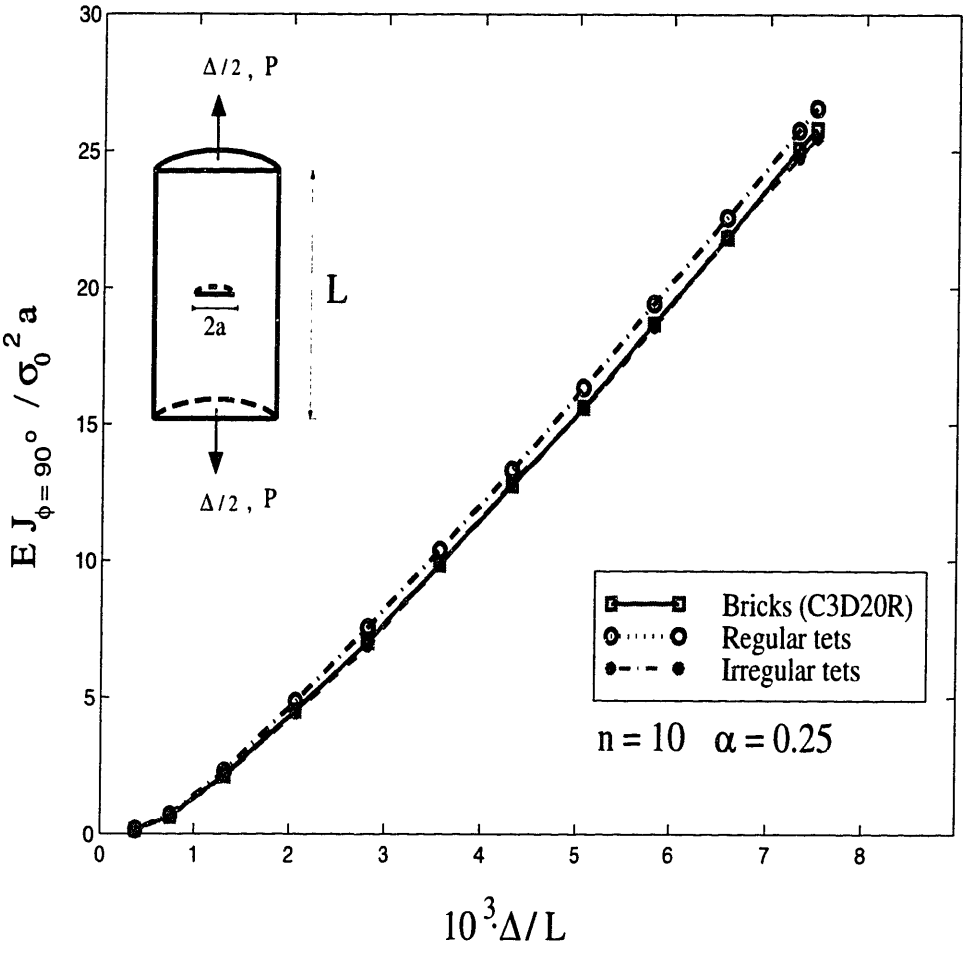

Figure 7-13: Variation of normalized J at the symmetry plane with normalized displacement for the semi-circular surface crack in a semi-infinite plate. Ramberg-Osgood deformation plasticity is used with $n = 10$ and $\alpha = 0.25$.

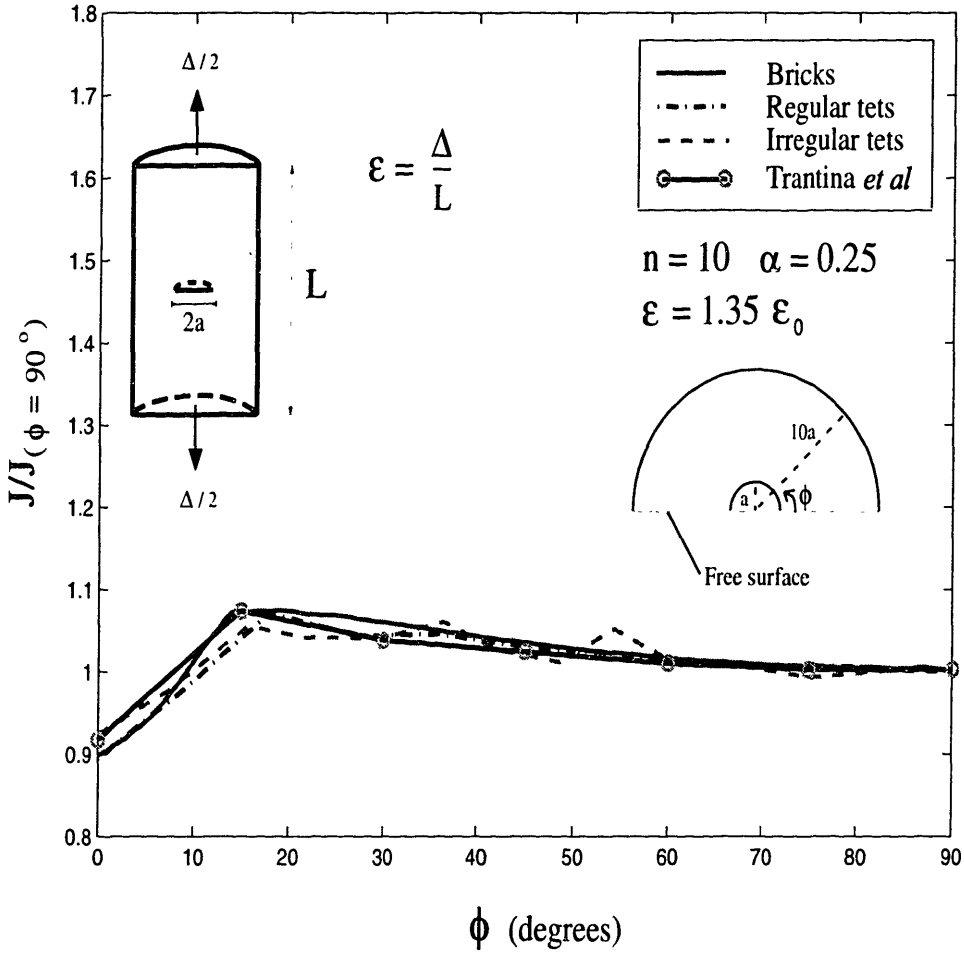

Figure 7-14: Variation of J normalized by J at the symmetry plane, along the crack front for the semi-circular surface crack in a semi-infinite body at a nominal strain ϵ = 1.35 ϵ_0. Nominal strain $\epsilon = \Delta/L$. Ramberg-Osgood deformation plasticity is used with $n = 10$ and $\alpha = 0.25$.

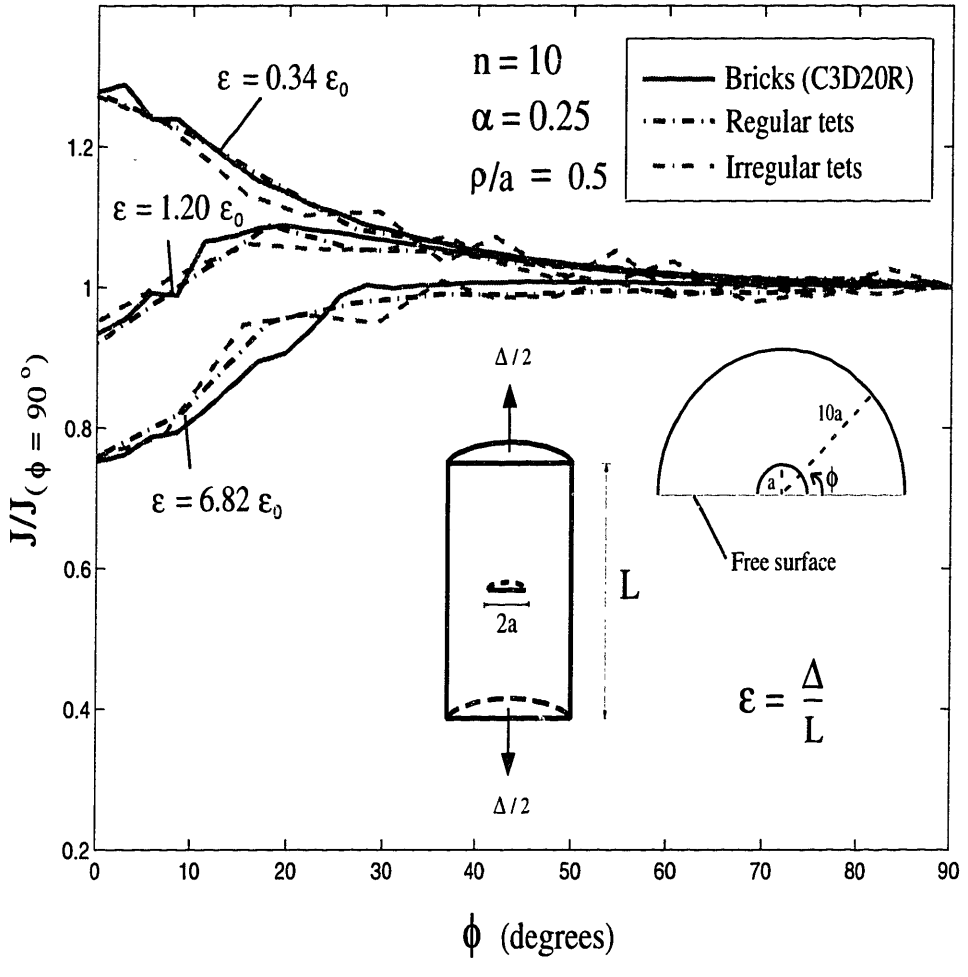

Figure 7-15: Variation of J normalized by J at the symmetry plane, along the crack front for the semi-circular surface crack in a semi-infinite body at different load levels. Nominal strain $\epsilon = \Delta/L$. Ramberg-Osgood deformation plasticity is used with $n = 10$ and $\alpha = 0.25$.

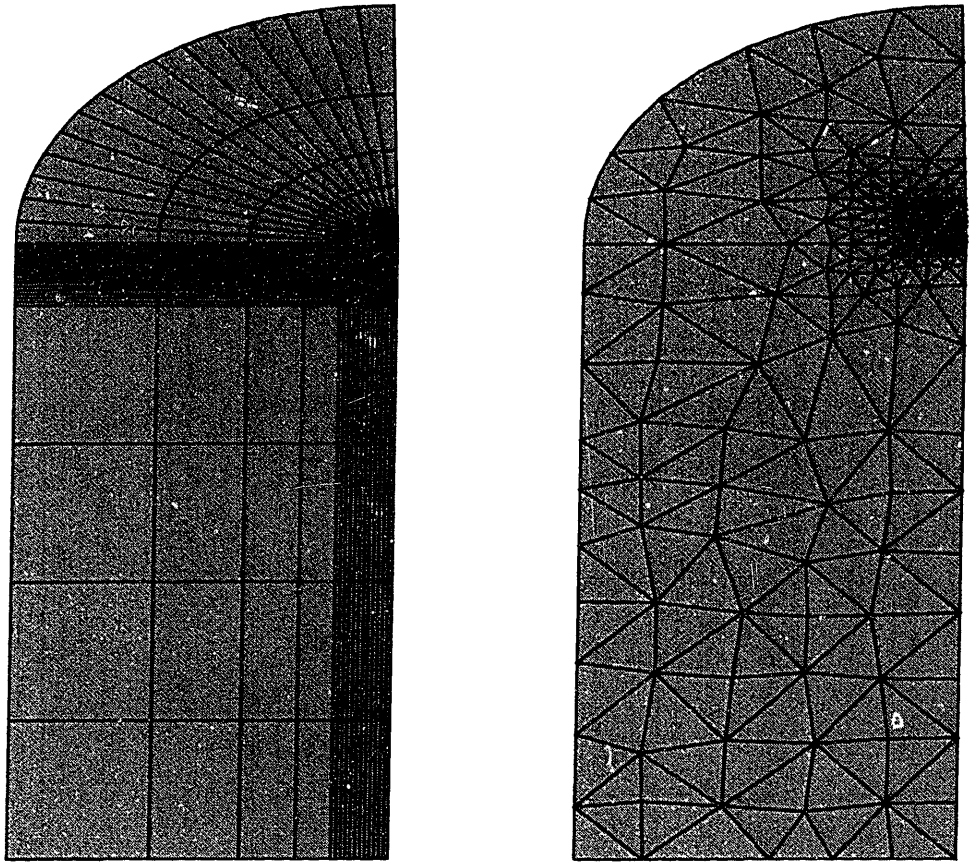

Figure 7-16: Finite element meshes for the semi-elliptical surface crack in a semi-infinite plate under tension. (a) Brick mesh from ABAQUS/Pre. (b) Irregular tetrahedral mesh from Pro/MESH.

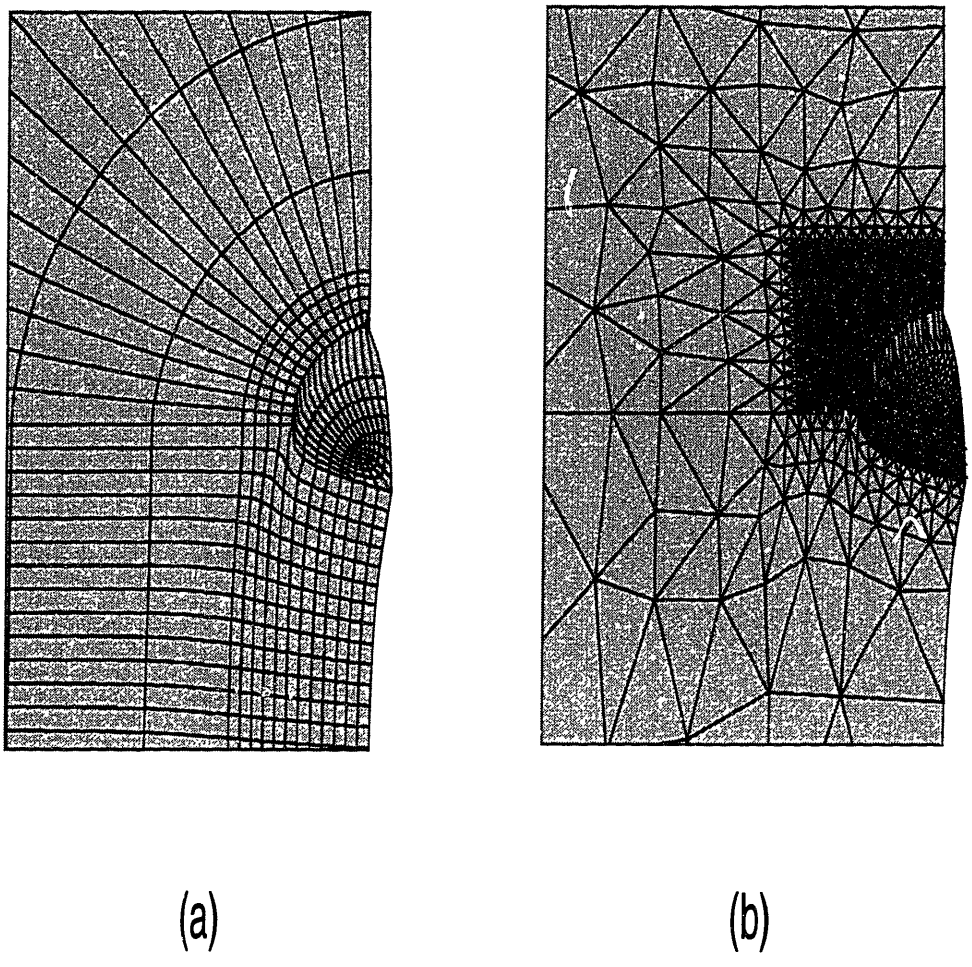

Figure 7-17: Close-up view near the crack-tip of the displaced meshes for the semi-elliptical surface crack. (a) Brick mesh from ABAQUS/Pre. (b) Irregular tetrahedral mesh from Pro/MESH.

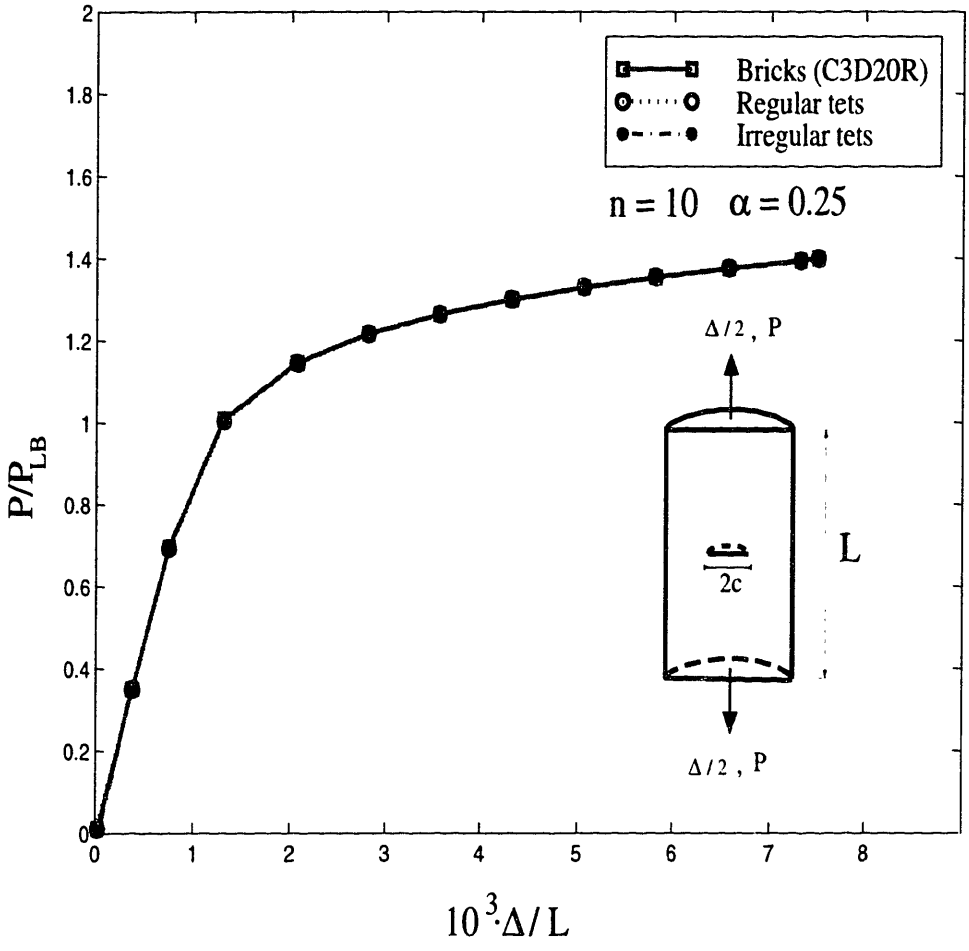

Figure 7-18: Variation of load P, normalized with $P_{LB} = \sigma_0 \pi(100a^2 - ac)$, versus normalized far-field displacement $10^3 \cdot \Delta/L$ for the semi-elliptical surface crack in a semi-infinite plate. Ramberg-Osgood deformation plasticity is used with $n = 10$ and $\alpha = 0.25$.

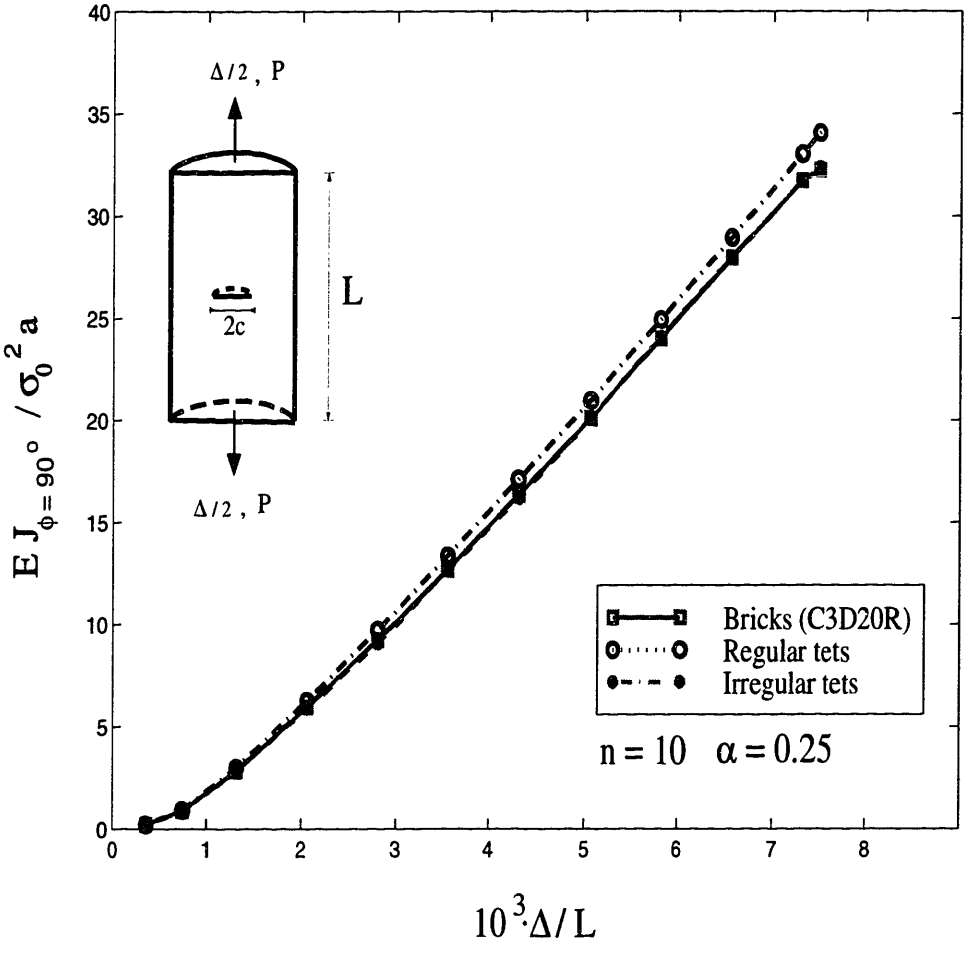

Figure 7-19: Variation of normalized J at the symmetry plane with normalized displacement for the semi-elliptical surface crack in a semi-infinite plate. Ramberg-Osgood deformation plasticity is used with $n = 10$ and $\alpha = 0.25$.

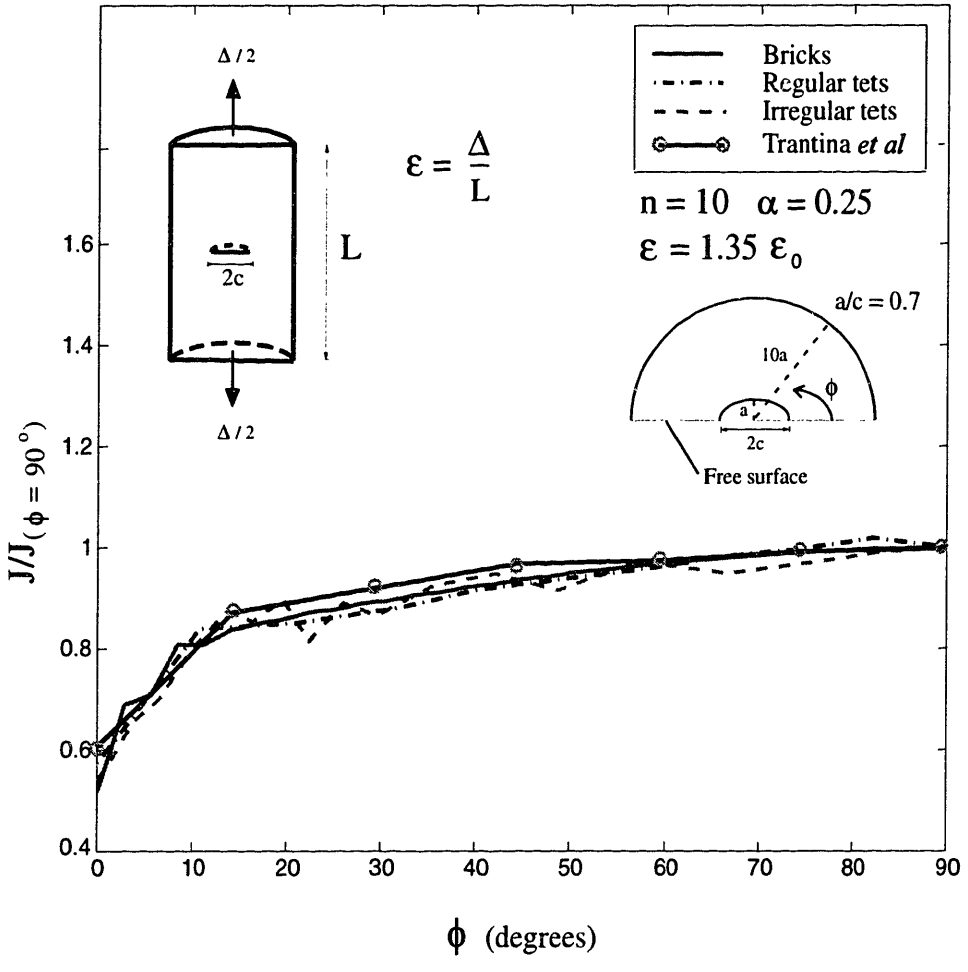

Figure 7-20: Variation of J, normalized by J at the symmetry plane, along the crack front for the semi-elliptical surface crack in a semi-infinite body at a nominal strain ϵ = 1.35 ϵ_0. Nominal strain $\epsilon = \Delta/L$. Ramberg-Osgood deformation plasticity is used with $n = 10$ and $\alpha = 0.25$.

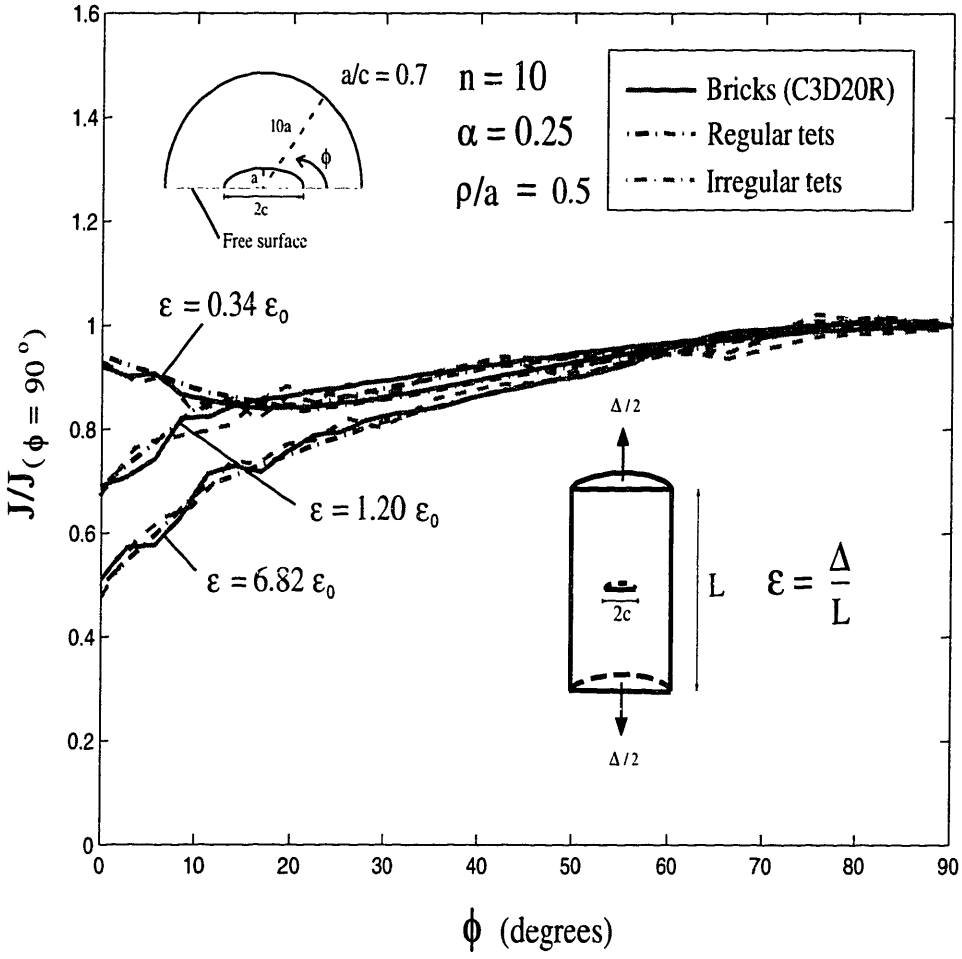

Figure 7-21: Variation of J, normalized by J at the symmetry plane, along the crack front for the semi-elliptical surface crack in a semi-infinite body at different load levels. Nominal strain $\epsilon = \Delta/L$. Ramberg-Osgood deformation plasticity is used with $n = 10$ and $\alpha = 0.25$.

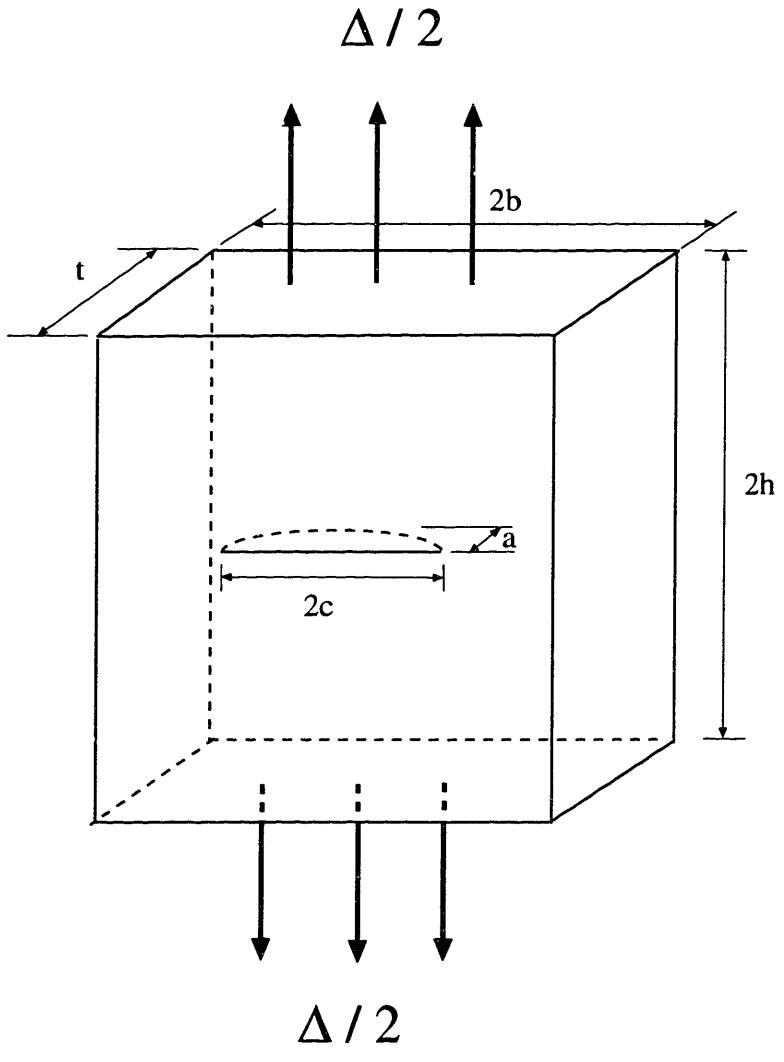

Figure 7-22: Model of the semi-elliptical surface crack in a finite thickness plate. The dimensional ratios are $a/c = 0.24$, $a/t = 0.60$, $b/t = 8$ and $h/t = 16$. The model is loaded by a uniform far-field relative displacement Δ.

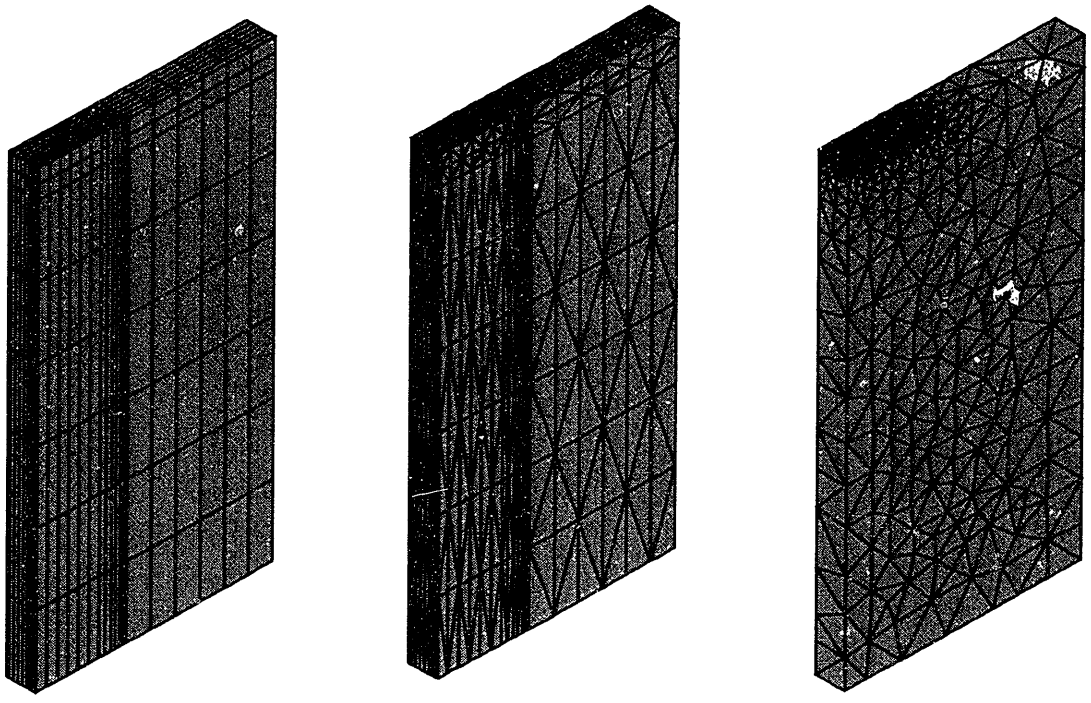

(a) (b) (c)

Figure 7-23: Finite element meshes for the semi-elliptical surface crack in a finite thickness plate. (a) Brick mesh generated using ABAQUS/Pre. (b) Regular tetrahedral mesh from ABAQUS/Pre. (c) Irregular tetrahedral mesh from Pro/MESH.

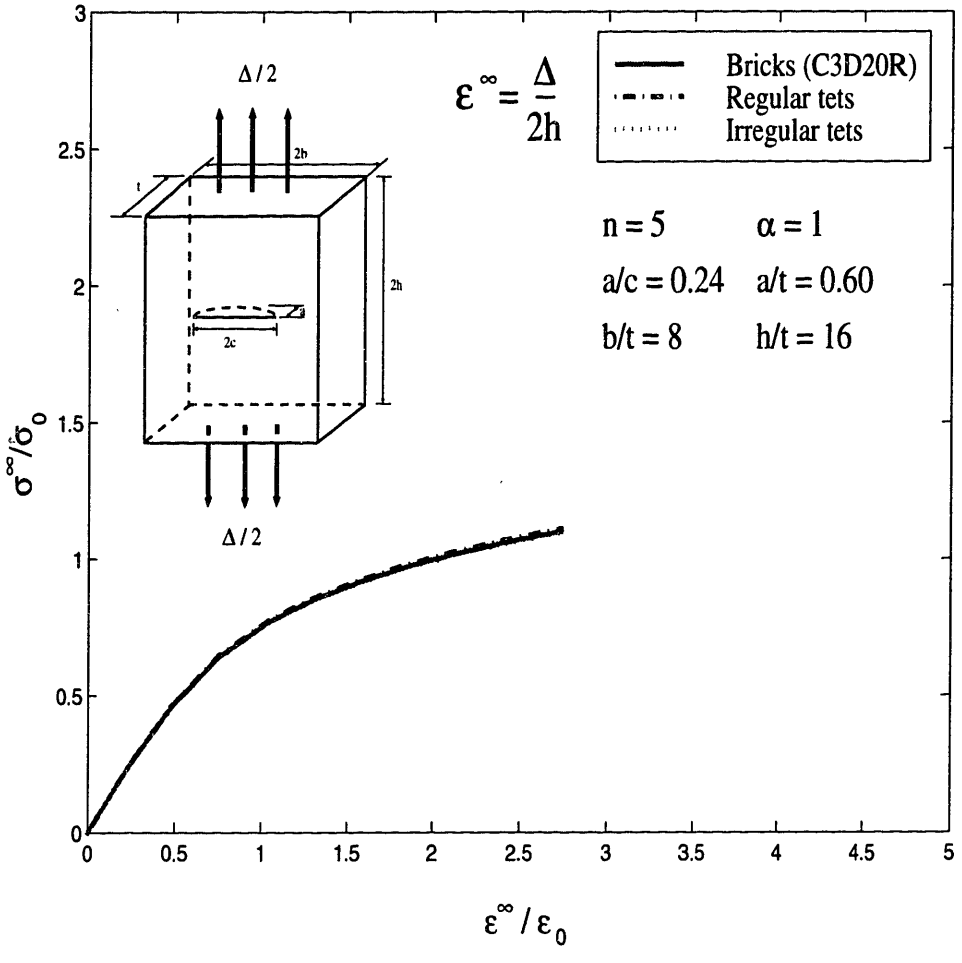

Figure 7-24: Variation of normalized far-field stress versus normalized far-field strain for the semi-elliptical surface crack in a finite thickness plate. Ramberg-Osgood material model is used with $n = 5$ and $\alpha = 1$. The far-field nominal strain $\epsilon^{\infty} = \Delta/2h$.

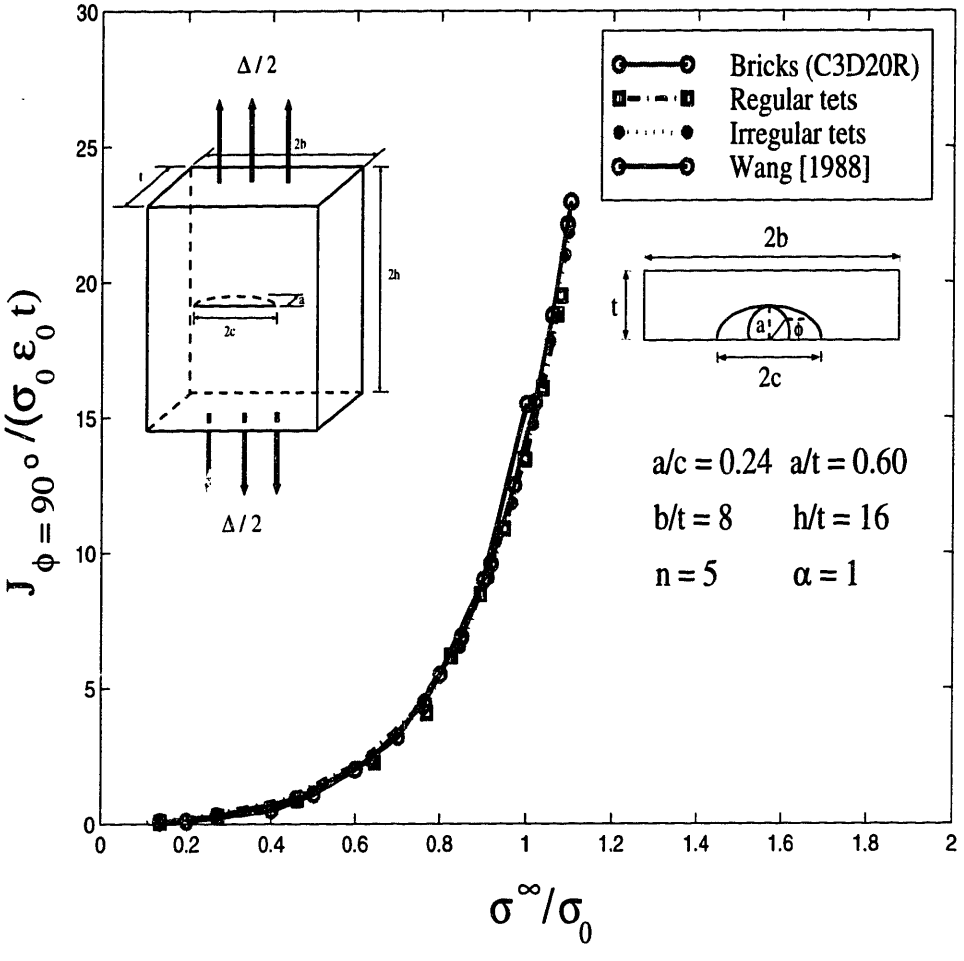

Figure 7-25: Variation of normalized J at the symmetry plane for the semi-elliptical surface crack in a finite thickness plate at different load levels. Ramberg-Osgood deformation plasticity is used with $n = 5$ and $\alpha = 1$.

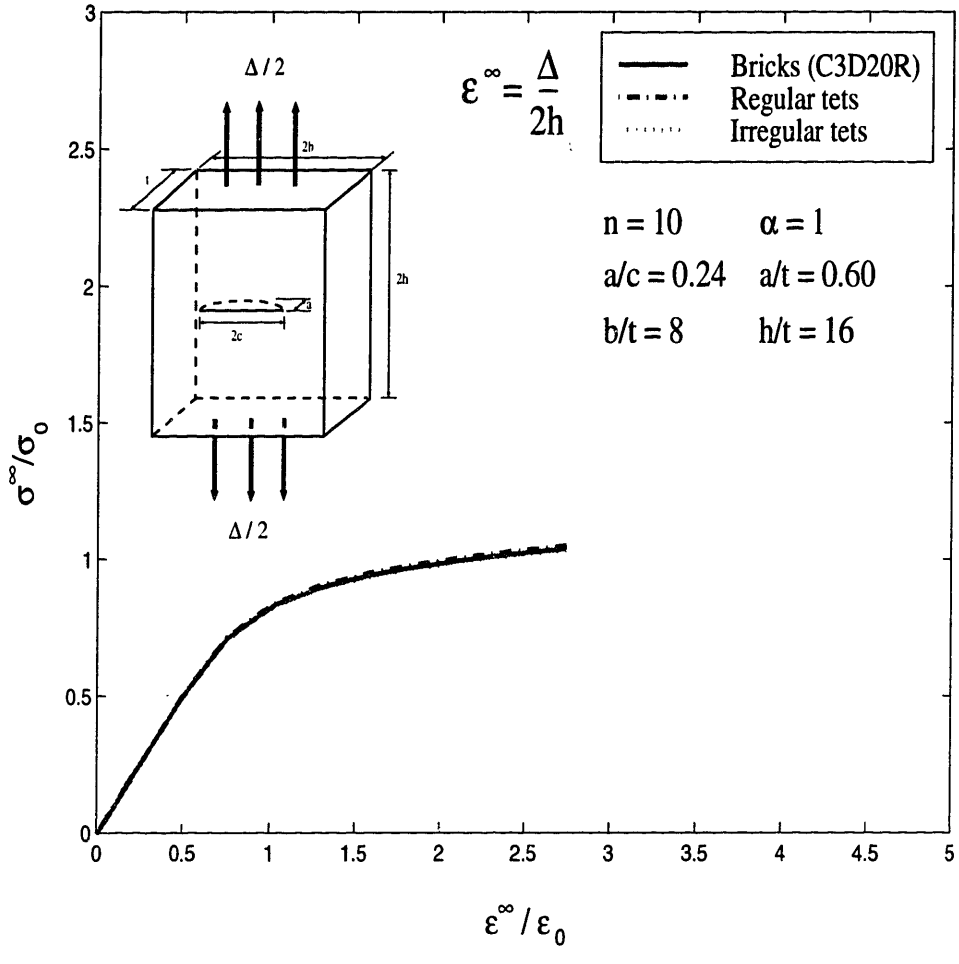

Figure 7-26: Variation of normalized far-field stress versus normalized far-field strain for the semi-elliptical surface crack in a finite thickness plate. Ramberg-Osgood material model is used with $n = 10$ and $\alpha = 1$. The far-field nominal strain $\epsilon^{\infty} = \Delta/2h$.

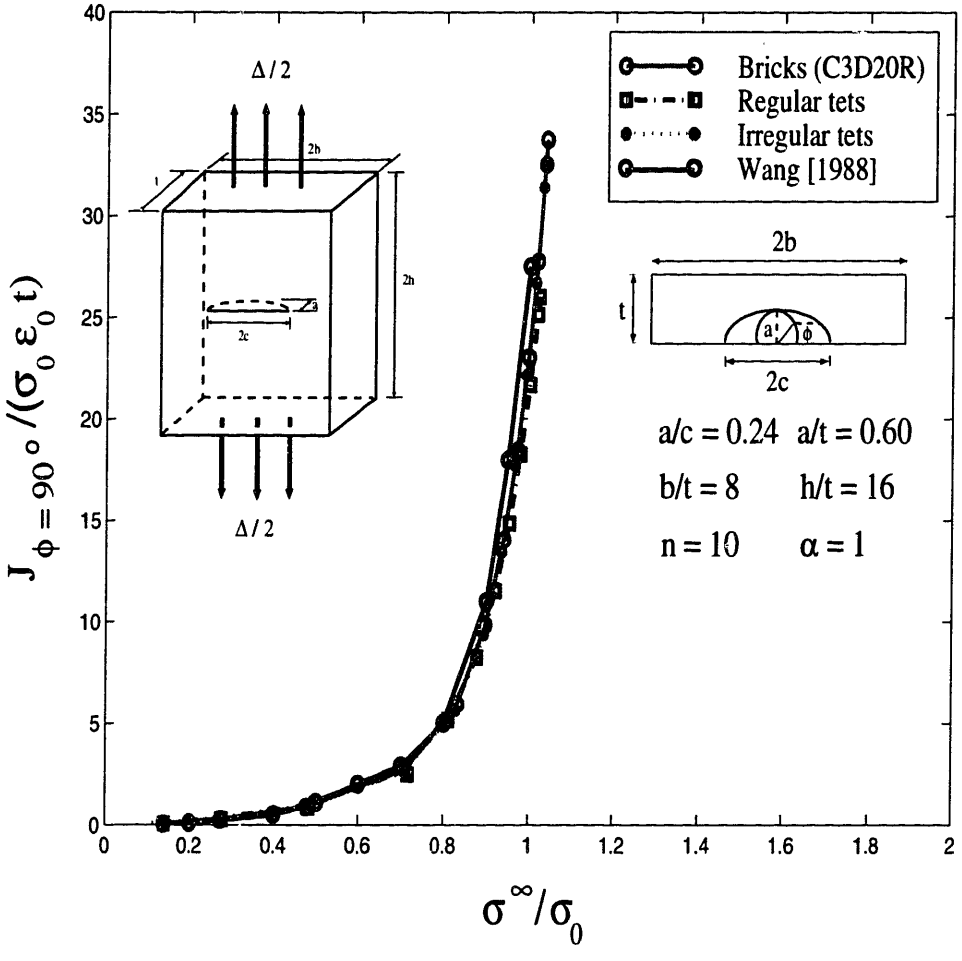

Figure 7-27: Variation of normalized J at the symmetry plane for the semi-elliptical surface crack in a finite thickness plate at different load levels. Ramberg-Osgood deformation plasticity is used with $n = 10$ and $\alpha = 1$.

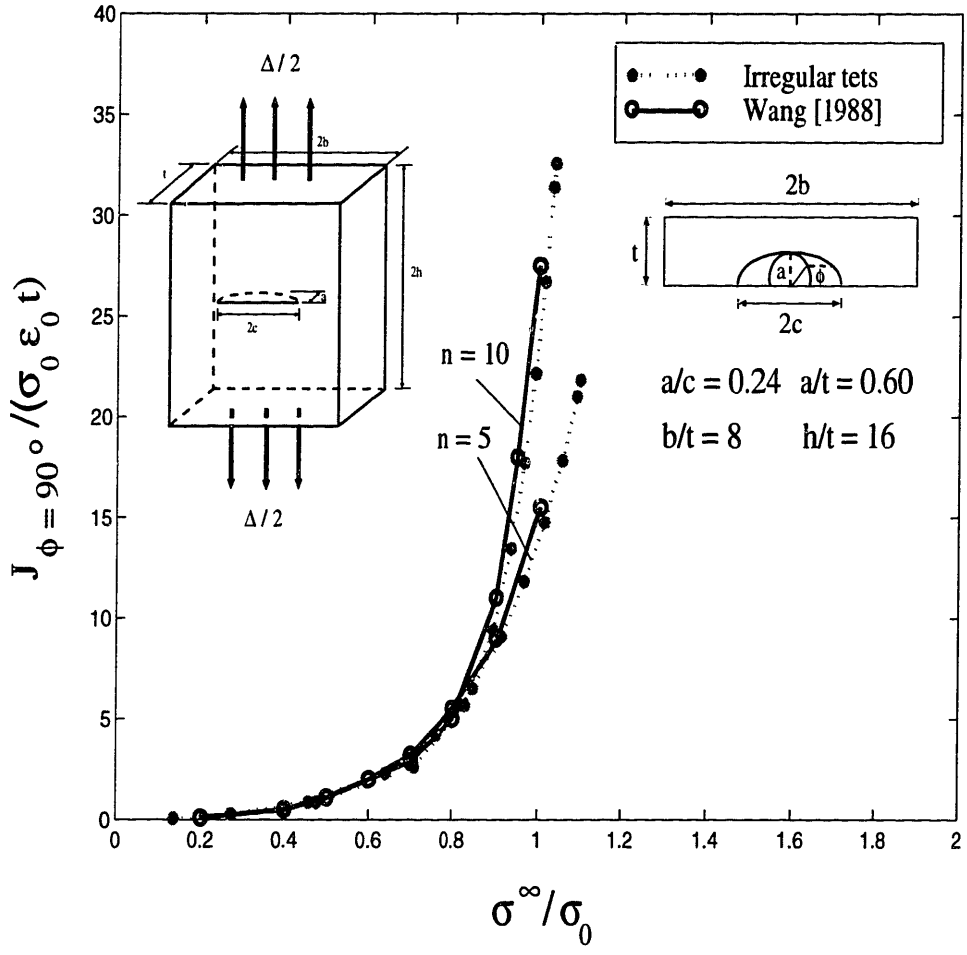

Figure 7-28: Comparison of normalized J at the symmetry plane at various load levels for hardening exponents $n = 5$ and $n = 10$. Ramberg-Osgood deformation plasticity is used with $\alpha = 1$.

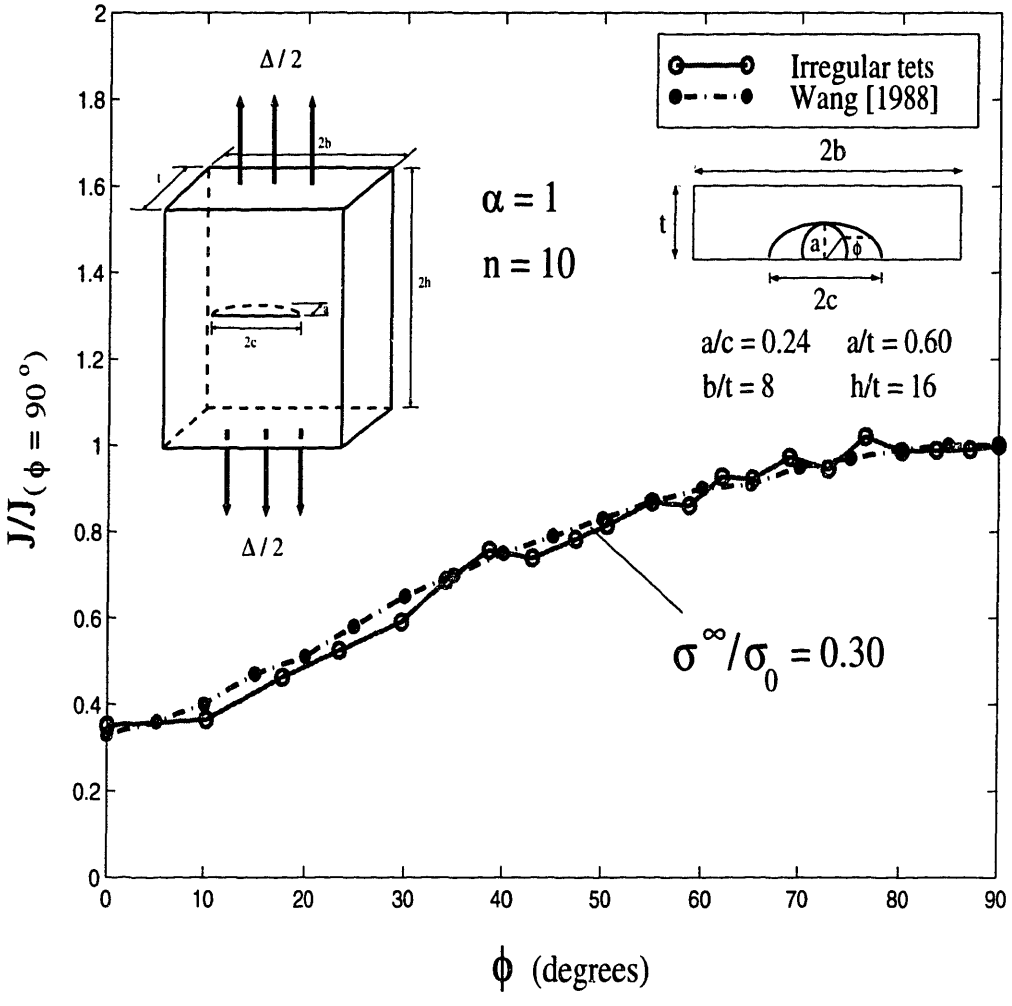

Figure 7-29: Variation of J, normalized by J at the symmetry plane, along the crack-front for the semi-elliptical surface crack in a finite thickness plate at load level σ^{∞}/σ_0 = 0.30. Ramberg-Osgood deformation plasticity is used with $n = 10$ and $\alpha = 1$.

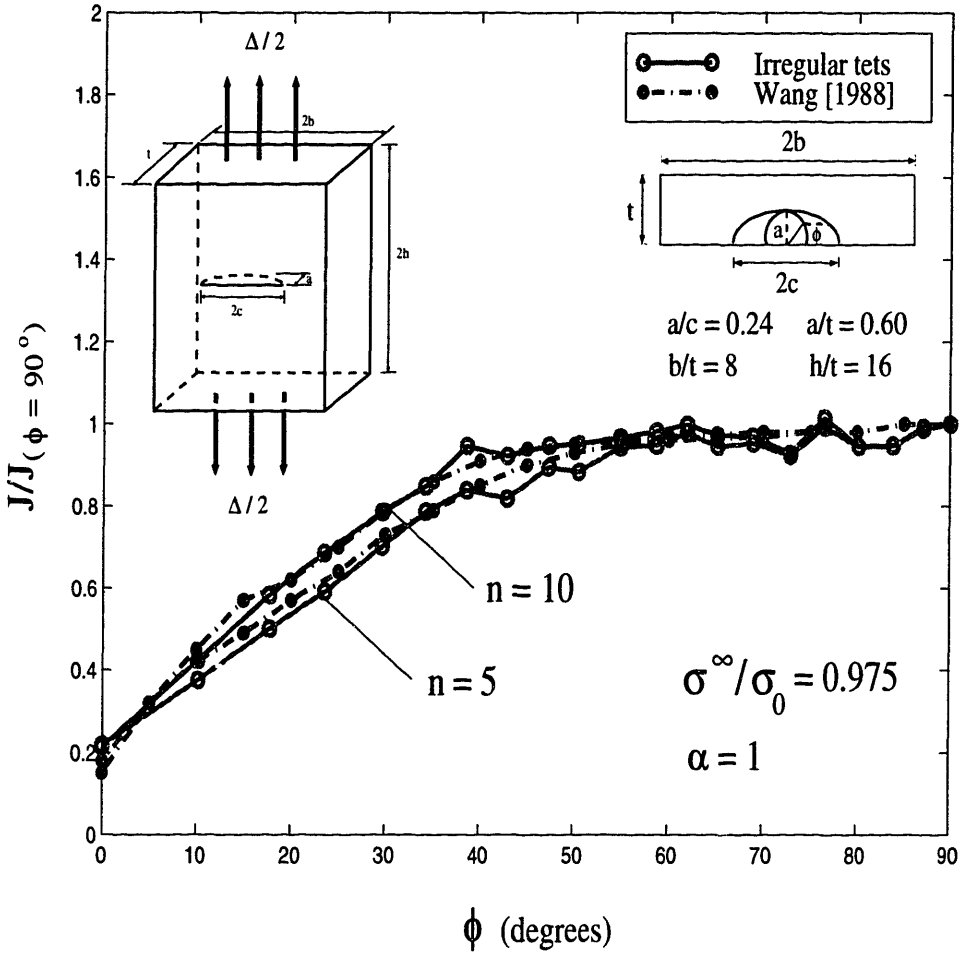

Figure 7-30: Variation of J normalized by J at the symmetry plane, along the crack-front for the semi-elliptical surface crack in a finite thickness plate at load level σ^{∞}/σ_0 = 0.975 for hardening exponents $n = 5$ and $n = 10$. Ramberg-Osgood deformation plasticity is used with $\alpha = 1$.

Chapter 8

Guidelines for obtaining accurate results

A parametric study on the accuracy achievable with the method proposed in chapter 4 was performed using the irregular tetrahedral meshes obtained from Pro/MESH [15]. Mesh convergence, and the effect of the size of the far-field element relative to the crack tip element were studied.

Based on the mesh-generating capabilities of Pro/MESH [15], we define two relevant parameters, P_1 and P_2, to study the above-mentioned factors. The parameter P_1 is defined as

$$P_1 = \frac{average\ element\ length\ along\ the\ crack-front}{relevant\ macroscopic\ crack\ dimension} ,$$

where the macroscopic crack dimension could be the dominant in-plane or out-of-plane crack dimension [1]. The parameter P_1 represents crack-front mesh refinement. We define a second parameter, P_2, as

$$P_2 = \frac{maximum\ length\ of\ a\ far-field\ element}{average\ element\ length\ along\ the\ crack-front} ,$$

where the length of a far-field element could be the "global maximum size" of the element as defined in Pro/MESH [15]. P_2 is an indication of the scale of typical far-field meshes, relative to the crack tip mesh, needed to obtain accurate results.

[1] For curved crack-fronts, the local radius of curvature must also be considered.

The parametric study was performed on the edge-crack in plane strain, with $(a/b) = 1/2$, subjected to uniform remote tension. The macroscopic crack dimension was chosen as the crack length, a. The elements along the crack-front were of uniform length. The parameter P_2 depends, implicitly, on the radius ρ, of the computational domain. This has not been addressed here, due to the limitations of the mesh generator chosen for the study. For advanced mesh generators having additional mesh gradation controls, the parameter P_2 can be readily redefined based on the maximum size in the domain radius. For all the cases, quarter-point crack-front elements were used, to obtain the square-root singularity as described earlier. We define $J_{var} = (J_{max} - J_{min})/J_{mean}$, where $J_{mean} = \int J dx/W$ is the average of the nodal J-values along the crack-front (see figure 5-2), with J_{max} and J_{min} being, respectively the maximum and minimum of these values.

Figure 8-1 gives the variation in J_{var} as a function of the parameters P_1 and P_2, for a domain size of $\rho/a = 0.7$. The variation in J_{mean} was observed to be within $1-2\%$ of J_{th} (see subsection 5.1.1) for all the cases. From figure 8-1, we note that to obtain results to an accuracy of $1-2\%$, the parameter P_2 has to be less than 4. The factor of 4 arises from the fact that the base for the perturbation field spans 4 crack-front elements [2]. The factor P_2 also directly correlates with the number of elements required in the model to obtain accurate results. This follows from the fact that P_2 relates the global mesh size to the mesh at the crack-front. Suppose a finer mesh is desired at the crack tip; then for accuracy in the calculated J-values, the factor P_2 has to be within the prescribed bounds (namely $P_2 \leq 4$ in this case), implying far-field mesh refinement as well. The results in figure 8-1 also give an idea of the effects of crack-front mesh refinement. For this specific problem, we found that, in order to obtain fairly accurate results, P_1 should not exceed a value of, approximately, 0.25.

The accuracy of the results increases with crack tip mesh refinement, as expected, indicating mesh convergence. For the edge-crack in plane strain, a study was also done on the accuracy of the computed J values obtainable without the use of quarter-

[2]The perturbation patterns, $\delta l^K(s) = f_s^K(s)$ need not be restricted to a piece-wise linear variation spanning four crack-front element-edges. See also chapter 9.

point crack-tip elements. It was observed that for $P_1 \leq 0.01$ and $P_2 \leq 4$, both $(|J_{mean} - J_{th}|)/J_{th} \leq 0.02$ and $J_{var} \leq 0.02$. In summary, although crack-front refinement and P_1 must be decided based on the desired accuracy and refinement of the results, the parameter P_2 is crucial for accuracy, and has to be within the prescribed bound.

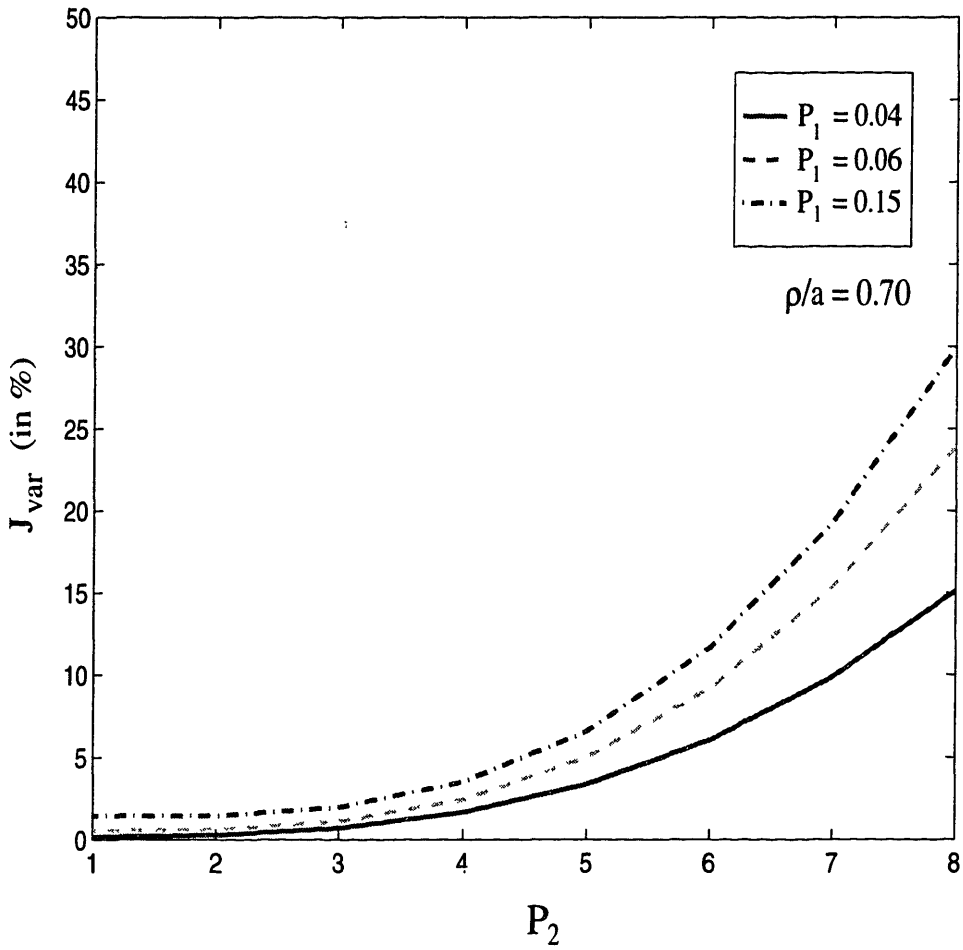

Figure 8-1: Sensitivity of the computed J-values, $J_{var} = (J_{max} - J_{min})/J_{mean}$. P_1 = (Average crack-front element-edge length) / (Crack length); P_2 = (Maximum far-field element length) / (Average crack-front element-edge length). Edge-crack in plane strain subjected to uniform remote tension.

Chapter 9

Conclusions and future work

9.1 Conclusions

With the development of CAD packages which can create complicated models and mesh them with tetrahedral elements with relative ease, there is a need for a general method to obtain crack-front singularity strengths from irregular tetrahedral element meshes so that the developments in the CAD systems can be directly extended to the whole class of fracture and fatigue crack propagation prediction problems. The practicality of the proposed method lies in its ability to obtain accurate results from rather irregular tetrahedral meshes readily obtained from commercially-available CAD packages possessing fairly good meshing capabilities.

A "straightforward" implementation failed to produce acceptably accurate results because of the large gradients within crack-front elements (both those having edge-coincidence with the crack front and those making only vertex contact) introduced by node-based interpolation of domain perturbations of highly localized support. This problem is offset by using perturbations of "extended support", numerical quadrature using analytically-calculated gradients of the perturbation vector field, and interpolation with the use of the nodal support at the boundaries of the model. The exponential radial variation also contributed to obtain a smooth perturbation field. On the meshes used, the method was shown to be accurate to $3-4\%$ of the theoretical predictions for a wide range of problems. Guidelines to obtain accurate results using

the method have been inferred from a parametric meshing study; they can be summarized by two useful parameters, P_1 and (more importantly) P_2, both of which must be suitably bounded, depending on the level of accuracy required. The correlation of the number of elements in the model required to obtain accurate results with P_1 and P_2 has been established, and the trade-off between accuracy and cost must be considered in selecting the values for these parameters.

9.2 Future work

9.2.1 Crack-front perturbations

A method of computing nodal J-values along the crack-front has been detailed in this thesis based on a four-element base piece-wise linear crack-front perturbation pattern that has been shown to work on a variety of crack geometries. The computation procedure has been developed for both elastic and elastic-plastic analysis. Various other related alternative schemes have been discussed in chapter 5, and their drawbacks have also been detailed. The piece-wise linear crack-front perturbation, though it has produced acceptable results for the cases studied, has an inherent discontinuity in the tangential derivative. The perturbation patterns need not be restricted to a piece-wise linear variation. An area of future research would be to develop more general perturbation patterns which would have continuous tangential gradients. Splines, for example, would be an ideal choice. But, implementation difficulties in using splines as perturbation patterns constitute impediments which have to be overcome, as the implementation of a spline-based perturbation pattern within a finite element scheme is not obvious. Another issue involves the accuracy on the proposed method, as discussed in chapter 8. A perturbation and domain integral evaluation scheme which produces good results from a mesh of a cracked structure which has far-field elements much larger than the crack-front elements (say a factor of 8-10) would be handy. This would be especially useful when fracture analysis (*i.e.* computation of J, K, etc.) has to be performed using a pre-existing mesh of a cracked structure obtained using

commercially-available CAD packages. This may again be related to the use of more "smooth" crack-front perturbation fields.

9.2.2 Two-parameter fracture mechanics

The correlation of macroscopic fracture behavior among various cracked configurations, such as initiation of crack growth and the onset of unstable crack propagation, is based on the "similarity" of crack-tip stress and deformation fields. Conventionally, these fields are represented by dominant singular fields whose magnitude is characterized by a single parameter such as K_I in linear elastic fracture mechanics (LEFM) or the J-integral in elastic-plastic fracture mechanics (EPFM). These representations are valid only as long as the singular fields dominate the crack-tip region and are the only dominant singularities. Larsson and Carlsson [34] showed from 2-D plane-strain elastic-plastic finite element analysis that the plastic-zone sizes of actual specimens were substantially different from the boundary layer solution at the same K_I. Hence to resolve the difference the modified boundary layer formulation (MBL) was applied using the second term in the Williams expansion (1.1) called the T-stress. Bilby, *et al.*, [35] showed that the two-parameter (K_I and T) approach characterizes the stress fields at a non-hardening blunted crack-tip better than K_I alone.

Fracture mechanics computation using tetrahedral elements can be extended by observing the ability of tetrahedral elements to accurately represent the crack tip stress and strain fields, with relevance to the two-parameter characterization of crack-tip fields. It has been shown that the elastic T-stress [36], especially negative T-stress, has a strong effect on the near-crack-tip fields. Wang [36] has performed an analysis of the effect of the T-stress on surface-cracked plates using brick elements. In order to perform such a two-parameter characterization study using tetrahedral elements, the stress fields, especially the crack-opening stress need to be accurately determined from the FE solution of the cracked model. To facilitate such an analysis, very fine meshes are needed at the crack-tip. To give an idea of the crack-tip mesh refinement, Wang [36] had used elements at the crack-tip which were 4 orders of magnitude smaller than the thickness of the plate, in his study of surface-cracked plates with a semi-elliptical

crack-front. Further he had also used sub-modeling and mapped a coarse mesh for the cracked plate to a fine mesh of a semi-elliptical region surrounding the crack-front.

Current commercially-available automatic mesh-generators are based on a fixed precision and and are suited to mesh geometries with meshes which vary to a maximum of 2 orders of magnitude. Detailed crack-front fracture mechanics computations usually involve crack-tip mesh refinements of up to 4 orders of magnitude. Also, in most fracture computations, we have a situation in which gradients of deformation or stress fields in one direction (*i.e.*, radial) dominates. In such cases, 3-D fracture studies performed using brick elements, have crack-tip elements with very high aspect ratios. Even though the tetrahedral elements are isotropic in nature, a crack-tip tetrahedral element having a high aspect ratio similar to the bricks, may be good enough. In any case, the effects of (geometrically) anisotropic tetrahedral crack-front elements have to be studied.

A scheme to build a mesh-generator suited for fracture computations is detailed below. The crux of the algorithm would be to mesh concentric tubular domains around a curve in space with tetrahedral elements. An ideal way to do this would be to mesh the surfaces of these domains first, and then build tetrahedra into the domain. To do this, one could start from the inner-most domain and progressively map the surface of the domain surrounding it, and then build tetrahedral elements for each of the domains. In summary, the key feature needed in a tetrahedral mesh generator to create fine crack-front meshes is to be able to map the surfaces of two adjacent concentric tubular domains, and mesh each of them with different element sizes. This way, we could progressively build a mesh with the required mesh-refinement at the crack-tip. While one could build such a mesh using brick elements, if the study has to conducted on a complex structure, then it maybe worthwhile (or needed in some cases) to mesh entire structure with tetrahedral elements.

9.2.3 Modeling crack-growth using tetrahedral elements

Ductile materials usually fail as the result of nucleation, growth and coalescence of microscopic voids that initiate at inclusions and second phase particles. Mathematical

models have been proposed for void growth and coalescence, and the most widely-referenced model is the Gurson model [37]. The Gurson model analyzes plastic flow in a porous medium by assuming that the material behaves as a continuum. One of the key parameters of the Gurson model is the void volume fraction. The Gurson model was modified by Tvergaard and Needleman [38], who replaced the void volume fraction by an effective void volume fraction. Ductile crack-growth has been modeled using 2-D FE analysis by Xia, *et al.* [39], using the void growth criteria through the Gurson model, in an elastic-plastic continuum model. The model uses a traction-displacement law on element faces spanning the separation plane, which is generally presumed to be known *a priori.* Crack-growth is modeled when the stress along element faces drop down to zero through the traction-displacement law. Three-dimensional crack-growth modeling using tetrahedral elements would be a very useful tool in modeling crack-growth. There exist limitations in modeling crack-growth through a traction-displacement law, as we have zero work-conjugate nodal forces for a 6-noded triangle subjected to constant stress. A modified tetrahedral element (C3D10M) has been developed by HKS, Inc. [40] to overcome this problem in large deformation and contact problems. Details of the modified tetrahedral element are not available at this time.

All of the above-mentioned issues, when incorporated into a robust computation scheme, would make fracture mechanics analysis using tetrahedral elements more accurate and convenient, when used in conjunction with CAD packages having superior tetrahedral meshing capabilities.

Appendix

Gradient of a node-based vector field

We define the vector quantity $\boldsymbol{f}$ in the element j by its nodal values at the K^{th} node, $\boldsymbol{F}^K$, and the bi-quadratic shape functions $\mathcal{N}^K(c_m)$ as

$$f_i(c_m) = \mathcal{N}^K(c_m) < F_i^K >_j, \tag{A.1}$$

where $< F_i^K >_j$ is the value of the i^{th} cartesian component of $\boldsymbol{F}$ at the K^{th} node in the element j, and c_m are the natural coordinates. We write the derivative of $\boldsymbol{f}$ as

$$\frac{\partial f_i(c_m)}{\partial c_m} = \frac{\partial \mathcal{N}^K(c_m)}{\partial c_m} < F_i^K >_j . \tag{A.2}$$

Also, we have

$$\frac{\partial f_i(c_m)}{\partial c_m} = \frac{\partial f_i}{\partial x_l}\frac{\partial x_l}{\partial c_m} = \frac{\partial f_i}{\partial x_l}\ \frac{\partial \mathcal{N}^K(c_m)}{\partial c_m} X_l^K, \tag{A.3}$$

where x_l are the global coordinates, and X_l^K are the nodal coordinates. We can write (A.3) in matrix notation for $f_{i,k}$ as

$$\begin{bmatrix} \frac{\partial \mathcal{N}^K}{\partial c_1}\cdot X_1^K & \frac{\partial \mathcal{N}^K}{\partial c_1}\cdot X_2^K & \frac{\partial \mathcal{N}^K}{\partial c_1}\cdot X_3^K \\ \frac{\partial \mathcal{N}^K}{\partial c_2}\cdot X_1^K & \frac{\partial \mathcal{N}^K}{\partial c_2}\cdot X_2^K & \frac{\partial \mathcal{N}^K}{\partial c_2}\cdot X_3^K \\ \frac{\partial \mathcal{N}^K}{\partial c_3}\cdot X_1^K & \frac{\partial \mathcal{N}^K}{\partial c_3}\cdot X_2^K & \frac{\partial \mathcal{N}^K}{\partial c_3}\cdot X_3^K \end{bmatrix} \begin{bmatrix} \frac{\partial f_i}{\partial x_1} \\ \frac{\partial f_i}{\partial x_2} \\ \frac{\partial f_i}{\partial x_3} \end{bmatrix} = \begin{bmatrix} \frac{\partial \mathcal{N}^K}{\partial c_1} \\ \frac{\partial \mathcal{N}^K}{\partial c_2} \\ \frac{\partial \mathcal{N}^K}{\partial c_3} \end{bmatrix} < F_i^K >_j$$

Inverting this system of equations, the derivatives $\partial f_i/\partial x_k$ within element j can be expressed as

$$f_{i,k} = C_k^K < F_i^K >_j . \tag{A.4}$$

Gradient of analytically-defined q*-functions*

Consider the point $P = \{s, r, \theta\}$ inside the domain Ω^K associated with the K-th perturbation pattern, as shown in figure 2-4. The position of P can be identified by the position of its projection, P^* on the crack front, and by the vector $\mathbf{r}$. We indicate

by $\boldsymbol{X}$ the position of P relative to a reference cartesian coordinate system. We can decompose the change in position $d\boldsymbol{X}$ into two components

$$d\mathbf{X} = (\mathbf{t} \cdot d\mathbf{X})\mathbf{t} + d\mathbf{r}, \tag{A.5}$$

so that the change in curvilinear coordinate s, associated with $d\boldsymbol{X}$ is

$$ds = (d\mathbf{X} \cdot \mathbf{t}). \tag{A.6}$$

Rearranging $(A.5)$, we can write

$$d\mathbf{r} = [I - (\mathbf{t} \otimes \mathbf{t})]d\mathbf{X}, \tag{A.7}$$

and we have

$$dr = \frac{\mathbf{r} \cdot d\mathbf{r}}{r} = \frac{\mathbf{r} \cdot [I - (\mathbf{t} \otimes \mathbf{t})]d\mathbf{X}}{r}. \tag{A.8}$$

Also, the change in the normal vector $\mathbf{n}$ at P^* can be expressed as

$$d\mathbf{n} = \frac{(ds)\mathbf{t}}{\rho_C} = \frac{(d\mathbf{X} \cdot \mathbf{t})\mathbf{t}}{\rho_C}, \tag{A.9}$$

where ρ_C is the local radius of curvature of the crack-front in the plane of the crack.

Now we have from (2.26) and (2.27)

$$\mathbf{q}^K(r,s) \;=\; f_s^K(s) \cdot f_r(r)\;\; \mathbf{n}(s). \tag{A.10}$$

Hence we can write

$$d\mathbf{q}^K \;=\; [f_s^K(\frac{\partial f_r}{\partial r})dr + f_r(\frac{\partial f_s^K}{\partial s})ds]\mathbf{n} + f_s^K \cdot f_r \;\; d\mathbf{n}. \tag{A.11}$$

Using $(A.6)$, $(A.8)$ and $(A.9)$, we can write $(A.11)$ as

$$d\mathbf{q}^K \;=\; [f_s^K(\frac{\partial f_r}{\partial r})\frac{\mathbf{r} \cdot [I - (\mathbf{t} \otimes \mathbf{t})]d\mathbf{X}}{r} + f_r(\frac{\partial f_s^K}{\partial s})(\mathbf{t} \cdot d\mathbf{X})]\mathbf{n} + f_s^K \cdot f_r \;\; \frac{(\mathbf{t} \cdot d\mathbf{X})\mathbf{t}}{\rho_C}. \tag{A.12}$$

Rearranging, we obtain

$$d\mathbf{q}^K = [f_s^K(\frac{\partial f_r}{\partial r})\mathbf{n}\otimes\frac{\mathbf{r}}{r} + f_r(\frac{\partial f_s^K}{\partial s})\mathbf{n}\otimes\mathbf{t} + \frac{f_s^K\cdot f_r}{\rho_C}\mathbf{t}\otimes\mathbf{t}]\cdot d\mathbf{X} = (\nabla\mathbf{q}^K)\cdot d\mathbf{X}. \quad (A.13)$$

Hence we obtain the gradient of $\mathbf{q}^K$ as

$$\nabla\mathbf{q}^K = f_s^K(\frac{\partial f_r}{\partial r})\mathbf{n}\otimes\frac{\mathbf{r}}{r} + f_r(\frac{\partial f_s^K}{\partial s})\mathbf{n}\otimes\mathbf{t} + \frac{f_s^K\cdot f_r}{\rho_C}\mathbf{t}\otimes\mathbf{t}. \quad (A.14)$$

Recalling section 6, to obtain accurate results we require the typical crack-front element length to be much less than the characteristic crack dimension. The term "ds" is of order element-length, while ρ_C is of the order of the macroscopic crack dimension; hence $\partial f_s^K/\partial s >> f_s^K/\rho_C$. Therefore, for evaluating (A.14), the third term has been neglected in our calculations.

Bibliography

[1] Field, D. A., The legacy of automatic mesh generation from solid modeling. *Computer Aided Geometric Design*, 1995, **12**, 651-673.

[2] Williams, M. L., On the stress distribution at the base of a stationary crack. *Journal of Applied Mechanics*, 1957, **24**, 109-114.

[3] Rooke, D. P and Cartwright, D. J, *Compendium of Stress Intensity Factors.* HMSO, London, 1976.

[4] Atluri, S. N., *Computational Methods in the Mechanics of Fracture.* North-Holland, 1973.

[5] Anderson, T. L., *Fracture Mechanics - Fundamentals and Applications.* CRC Press, Inc., 2000 Corporate Blvd., N.W., Boca Raton, Florida 33431, 1995.

[6] Červenka, J. and Saouma, V. E., Numerical evaluation of 3-D SIF for arbitrary finite element meshes. *International Journal of Fracture*, 1997, **57**, 541-563.

[7] Rice, J. R., A path independent integral and the approximate analysis of strain concentration by notches and cracks. *Journal of Applied Mechanics*, 1968, **35**, 379-386.

[8] Li, F. Z., Shih, C. F. and Needleman, A., A comparison of methods for calculating energy release rates. *Engineering Fracture Mechanics* , 1985, **21**, 405-421.

[9] Parks, D. M., A stiffness derivative finite element technique for determination of crack tip stress intensity factors. *International Journal of Fracture*, 1974, **10**, 487-502.

[10] Eshelby, J. D., Energy relations and the energy-momentum tensor in continuum mechanics, in *Inelastic Behavior of Solids*, (edited by Kanninen, M. F., Adler, W. F., Rosenfield, A. R. and Jaffee, R. I.), McGraw Hill, 1970, 77-115.

[11] Shih, C. F., Moran, B. and Nakamura, T., Energy release rate along a three-dimensional crack front in a thermally stressed body. *International Journal of Fracture*, 1986, **30**, 79-102.

[12] Budiansky, B. and Rice, J. R., Conservation laws and energy release rates. *Journal of Applied Mechanics*, 1973, **40**, 201-203.

[13] Hughes, T. J. R., *The Finite Element Method.* Prentice-Hall, 1987.

[14] ABAQUS/Pre, Release 5.7, Hibbitt, Karlsson & Sorensen, Inc., Pawtucket, RI 02860, 1998.

[15] Pro/MESH, Release 17.0, Parametric Technology Corporation, Waltham, MA 02154, 1998.

[16] Barsoum, R. S., On the use of isoparametric finite elements in linear elastic fracture mechanics. *International Journal for Numerical Methods in Engineering*, 1976, **10**, 25-37.

[17] ABAQUS/Standard, Release 5.7, Hibbitt, Karlsson & Sorensen, Inc., Pawtucket, RI 02860, 1998.

[18] ABAQUS Theory Manual. Hibbitt, Karlsson & Sorensen, Inc., Pawtucket, RI 02860, 1998.

[19] Tada, H., Paris, P. C. and Irwin, G. R., *The Stress Analysis of Cracks Handbook.* Paris Productions, 225 Woodbourne, St.Louis, MO, 1985.

[20] Raju, I.S. and Newman, J. C., Stress-intensity factors for a wide range of semi-elliptical surface cracks in finite-thickness plates. *Engineering Fracture Mechanics*, 1979, **11**, 817-829.

[21] Pickard, A. C., *The Application of 3-D FEM to Fracture Mechanics and Fatigue Life Prediction.* Engineering Materials Advisory Services Ltd., Warley, West Midlands, U.K., 1985.

[22] Nakamura, T. and Parks, D. M., Three-dimensional stress field near the crack front of a thin elastic plate. *Journal of Applied Mechanics*, 1988, **55**, 805-813.

[23] Hutchinson, J. W., Singular behavior at the end of a tensile crack tip in a hardening material. *Journal of the Mechanics and Physics of Solids*, 1968, **16**, 13-31.

[24] Rice, J. R. and Rosengren, G. F., Plane strain deformation near a crack tip in a power law hardening material. *Journal of the Mechanics and Physics of Solids*, 1968, **16**, 1-12.

[25] Lubliner, J., *Plasticity Theory.* Macmillan Publishing Company, New York, 1990.

[26] Budiansky, B., A reassessment of deformation theories of plasticity. *Journal of Applied Mechanics*, 1959, **81**, 259-264.

[27] Begley, J. A. and Landes, J. D., The J-Integral as a Fracture Criterion. *Fracture Toughness, Part II*, ASTM STP 514, 1972, 1-20.

[28] Kanninen, M. F. and Popelar, C. H., *Advanced Fracture Mechanics.* Oxford University Press, New York, 1985.

[29] McClintock, F. A. and Argon, A. S., *Mechanical Behavior of Materials.* Addison-Wesley Publishing Co., Reading, MA, 1966.

[30] Nagtegaal, J. C., Parks, D. M. and Rice, J. R., On numerically accurate finite element solutions in the fully plastic range. *Computer Methods in Applied Mechanics and Engineering*, 1974, **4**, 153-177.

[31] Kumar, V., German, M. D. and Shih, C. F., An engineering approach for elastic-plastic fracture analysis. EPRI Report NP-1931, Electric Power Research Institute, Palo Alto, CA, 1981.

[32] Trantina, G. G., deLorenzi, H. G. and Wilkening, W. W., Three-dimensional elastic-plastic finite element analysis of small surface cracks. *Engineering Fracture Mechanics*, 1983, **18**, 925-938.

[33] Wang, Y., Analysis of fracture initiation in surface-cracked plates. S. M. Thesis, M.I.T., 1988.

[34] Larsson, S. G. and Carlsson, A. J., Influence of non-singular stress terms and specimen geometry on small-scale yielding at crack tips in elastic-plastic material. *Journal of Mechanics and Physics of Solids*, 1973, **21**, 263-277.

[35] Bilby, B. A., Cardew, G. E., Goldthrope, M. R. and Howard, I. C., A finite element investigation of the effect of specimen geometry on the fields of stress and strain at the tips of stationary cracks. *Size Effects in Fracture*. Mechanical Engineering Publications Limited, London, United Kingdom, 1986, 37-46.

[36] Wang, Y., A two-parameter characterization of elastic-plastic crack-tip fields and applications to cleavage fracture. Ph. D. Thesis, M.I.T., 1991.

[37] Gurson, A. L., Continuum theory of ductile rupture by void nucleation and growth. *Journal of Engineering Materials and Technology*, 1977, **99**, 2-15.

[38] Tvergaard, V. and Needleman, A., Analysis of the cup-cone fracture in a round tensile bar. *Acta Metallurgica*, 1984, **32**, 157-169.

[39] Xia, L., Shih, C. F. and Hutchinson, J. W., A computational approach to ductile crack-growth under large-scale yielding conditions. *Journal of the Mechanics and Physics of Solids*, 1995, **43**, 389-413.

[40] ABAQUS/Standard, Release 5.8, Hibbitt, Karlsson & Sorensen, Inc., Pawtucket, RI 02860, 1999.

THESIS PROCESSING SLIP

FIXED FIELD: ill. _____ name _____

index _____ biblio _____

▶ COPIES: (Archives) Aero Dewey (Eng) Hum

Lindgren Music Rotch Science

TITLE VARIES: ▶☐ _____

NAME VARIES: ▶☐ _____

IMPRINT: (COPYRIGHT) _____

▶ COLLATION: 133 l

▶ ADD: DEGREE: _____ ▶ DEPT.: _____

SUPERVISORS: _____

NOTES:

cat'r: date:

page: 3140

▶ DEPT: M.E.

▶ YEAR: 1999 ▶ DEGREE: S.M.

▶ NAME: RAJARAM, Harish